Title

Rapid Wintertime Formation of Phenolic Secondary Organic Aerosol from Brown Carbon Photochemistry

Journal

Environmental Science &
Technology, 60(32)

ISSN

0013-936X

Authors

Heinlein, Laura MD
Kuhn, Jonas
Ijaz, Amna
et al.

Publication Date

2026-08-18

DOI

10.1021/acs.est.6c03997

Environmental Science & Technology

pubs.acs.org/est

Article

Rapid Wintertime Formation of Phenolic Secondary Organic Aerosol from Brown Carbon Photochemistry

Laura M. D. Heinlein,* Jonas Kuhn, Amna Ijaz, Brice Temime-Roussel, Karolina Cysneiros de Carvalho, Mallory Liebes, Fangzhou Guo, James H. Flynn, III, Kyle Moor, Brent Williams, Barbara D'Anna, Jochen Stutz, and Cort Anastasio*

Cite This: *Environ. Sci. Technol.* 2026, 60, 22748−22758

Read Online

ACCESS | Metrics & More | Article Recommendations | Supporting Information

ABSTRACT: Biomass burning (BB) is a major organic aerosol source during urban winter pollution events. BB particles are rich in brown carbon (BrC) and absorb light to produce photooxidants such as oxidizing triplet excited states of organic chromophores ($^3C^*$). In midlatitudes, semivolatile phenols (ArOH) from BB are oxidized to form phenolic secondary organic aerosol (SOA) under moderate temperatures and sunlight. Here, we explore whether phenolic SOA is also formed in a cold, relatively dark, high-latitude city during winter. We use measurements from the 2022 ALPACA field campaign in Fairbanks, Alaska, incorporated into the PACT-1D model with added emissions, partitioning, and chemistry for 34 semivolatile BB phenols. The model includes phenol oxidation in the gas phase and in two populations of particles—aqueous and organic. Despite short pollutant residence times within the polluted surface layer, simulated phenolic SOA formation is fast, generating up to 4.5 μg m^{-3}, with 99% produced by $^3C^*$ in organic particles. The modeled phenolic SOA explains up to 34% of measured daytime oxidized organic aerosol (OOA), indicating it is a significant portion of the poorly understood OOA in Fairbanks. Our results reveal that BrC photochemistry can be an important source of atmospheric oxidizing capacity even during high-latitude winters.

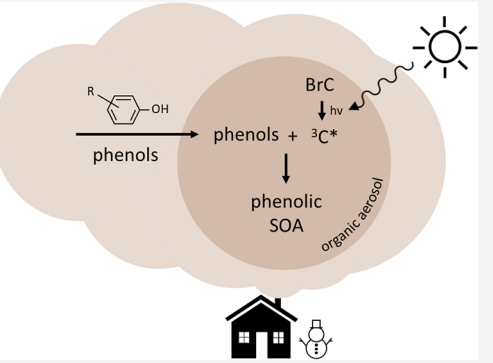

KEYWORDS: *Multiphase chemistry, winter pollution, atmospheric inversions, biomass burning, photooxidants, triplet excited states*

INTRODUCTION

Severe winter pollution events consistently make Fairbanks, Alaska one of the US cities with the worst 24-h $PM_{2.5}$ pollution.[1] In winter, multiday temperature inversions trap local emissions and drive high $PM_{2.5}$ concentrations in Fairbanks and other northern cities.[2,3] Although multiphase chemistry in high-latitude winter atmospheres is traditionally expected to be negligible,[4] reports from the Alaskan Layered Pollution and Chemical Analysis (ALPACA) field campaign in the winter of 2022 found this is not the case, at least for Fairbanks.[5,6] Secondary sulfate, nitrate, and hydroxymethanesulfonate (HMS) were found to be major components of Fairbanks' PM pollution,[5−10] revealing the important role of multiphase processes.

Biomass burning is widely considered to be a dominant primary PM source during Fairbanks winters.[11−14] Organic aerosol (OA) is the dominant component of winter PM, accounting for 66% of fine particle mass in 2022.[11,12] Biomass-burning organic aerosol (BBOA) is a major primary OA source, accounting for 30−80% of OA during ALPACA, depending on the measurement technique.[11−13] Oxidized organic aerosol (OOA) accounts for roughly half of OA across recent winters, yet its sources are poorly understood.[12] At lower latitudes, SOA is an important OOA component.[12,15] Phenols (ArOH), a class of SOA precursors abundantly emitted in woodsmoke, have cumulative gas and particle emissions equivalent to 38−57% of total particulate wood smoke emissions.[16−18] Phenols can be oxidized in the gas phase and in particles to form phenolic SOA[18−22] which has been identified in winter PM pollution at lower latitudes.[18,23]

In Fairbanks during winter, it is unclear whether significant SOA formation is possible. Traditional SOA formation mechanisms, such as gas-phase reactions of VOCs with $^{\bullet}OH$ or O_3, are slow due to low actinic fluxes and low gas-phase oxidant concentrations.[2] As an alternative, we hypothesize that brown carbon (BrC) photochemistry in particles forms significant phenolic SOA.[8,18,24,25] BB emissions make particles in Fairbanks rich in brown carbon (BrC), which absorbs longer wavelengths of light to form photooxidants such as oxidizing triplet excited states of brown carbon ($^3C^*$ or triplets), singlet

Received: March 17, 2026
Revised: July 17, 2026
Accepted: July 20, 2026
Published: July 31, 2026

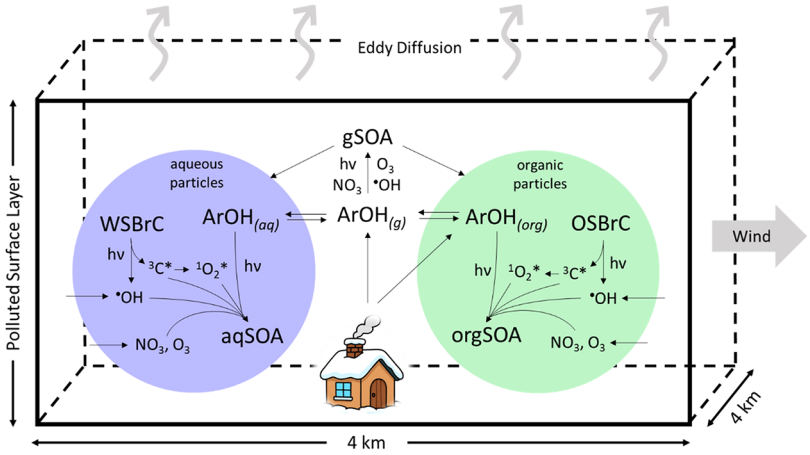

Figure 1. Conceptual model of the formation of phenolic (ArOH) secondary organic aerosol (SOA) in PACT-1D. ArOHs are assumed to come only from residential and commercial wood burning. Externally mixed aqueous and organic particles contain water-soluble BrC (WSBrC) and organic-soluble BrC (OSBrC), respectively, which absorb light to form $^3C^*$, $^1O_2^*$, and $^\bullet OH$. O_3, NO_3, and $^\bullet OH$ partition into particles from the gas phase. Phenols are oxidized to form SOA in the gas phase (gSOA), aqueous particles (aqSOA), and organic particles (orgSOA). The box represents homogeneous vertical layers over a 4 × 4 km area of Fairbanks simulated in PACT-1D. Air is lost horizontally due to wind and vertically due to mixing with clean background air.

molecular oxygen ($^1O_2^*$), and hydroxyl radical ($^\bullet OH$).[8,24,26−29] These oxidants can chemically react with ArOH to form phenolic SOA,[19,20,30−32] but are rarely included in SOA models.[18,25,33] Moreover, most studies neglect photooxidants from organic-soluble BrC (OSBrC), which during ALPACA absorbed three times more sunlight than water-soluble BrC (WSBrC)[34] and is likely an important photooxidant source.[35]

In this work, we explore whether phenolic SOA formation is significant during winter pollution events in Fairbanks. We simulate ArOH chemistry using the Platform for Atmospheric Chemistry and Transport in One Dimension (PACT-1D) optimized for Fairbanks' winter atmospheric dynamics.[9,36] We extend the multiphase kinetic mechanism in PACT-1D by adding BrC photooxidant production and phenolic SOA formation. This includes: (1) BrC photooxidant formation in aqueous and organic particles from water- and organic-soluble BrC, respectively; (2) emissions and gas-particle partitioning of 34 semivolatile phenols; and (3) gas- and particle-phase phenolic SOA formation during a 2022 winter pollution event in Fairbanks to quantitatively assess if phenolic SOA formation is possible.

METHODS

PACT-1D is a MATLAB-based, one-dimensional chemistry and transport model developed to interpret the near-surface distribution of atmospheric trace gases using explicit chemical kinetics.[37] The model was optimized to match the meteorology and multiphase chemistry during winter 2022 in Fairbanks, Alaska,[9,36,38] resulting in excellent agreement with measurements of SO_2,[36] ozone, nitrogen oxides, nitrous acid, formaldehyde, nitrate, and sulfate.[9,36] In this work, we expand upon PACT-1D by adding kinetic processes to simulate BrC photochemistry and multiphase phenolic SOA formation (Figure 1).

ALPACA PACT-1D

For ALPACA, PACT-1D models a 4 × 4 km area that covers both downtown Fairbanks and residential neighborhoods.[36,38] The model assumes horizontal homogeneity. Vertical mixing is described by eddy diffusion coefficients derived from measured boundary layer heights and horizontal transport is constrained by measured wind speeds. Emissions of gases and particles are modeled using the emissions inventory developed by the Environmental Protection Agency (EPA) and the Alaska Department of Environmental Conservation.[39] PACT-1D simulates gas-phase photochemistry with the RACM-2 chemical mechanism and actinic flux measurements,[8,9] and aqueous chemistry with Henry's Law partitioning and aqueous-phase reactions.[9] In this work, we added organic particles as sites for multiphase chemistry, as described below. The loss of gases and particles in PACT-1D is due to deposition and mixing with clean background air.[9]

Particle Composition. Winter PM in Fairbanks contains significant amounts of aerosol liquid water (ALW)[40] and high concentrations of organic matter, with an average ($\pm 1\sigma$) ALW concentration of 8.5($\pm$8.0) $\mu g\ m^{-3}$ and an average OA concentration of 6.8($\pm$8.1) $\mu g\ m^{-3}$ between 1/28/2022 and 2/11/2022 (Figure S2).[11,12] We simulate two externally mixed populations of 300 nm diameter particles—one aqueous and one organic—that each interact with the gas phase. During ALPACA, both inorganic species and organic aerosol uptake significant ALW,[41] and single particle measurements reveal multiphase processing on aqueous and biomass burning particles.[10] The ALW formation rate and OA emission rate are calculated by scaling the EPA methane emissions from wood burning so that modeled concentrations of ALW[40] and OA (from AMS)[11] mimic measurements from ALPACA (Figure S2). The total OA is then divided into water-soluble OA in aqueous particles and organic-soluble OA in organic particles based on the measured ratio of light absorption from water- and methanol-soluble BrC (Section S6).

Biomass-Burning Phenols. We created emissions profiles of 34 semivolatile ArOHs from wood smoke (Table S1 and Section S1).[17] We first generated a levoglucosan emissions profile by scaling the methane emissions from wood smoke so that modeled levoglucosan concentrations matched measurements (Figure S3a).[11] We then apportioned levoglucosan to hardwood and softwood (Figure S3b)[11] and used measured emissions ratios of phenols to levoglucosan (Table S2) to generate phenol emissions profiles.[17] As our base case, we assume all ArOHs are initially emitted in organic particles, from which they partition into the gas phase and aqueous particles. We assess this assumption with a sensitivity simulation with all phenols emitted as gases: as shown in Figure S9, this change makes aqueous and nontriplet reactions more significant but $^3C^*$-mediated reaction in organic particles still dominate during polluted periods when phenolic SOA is most significant. Our simulations only account for phenol emissions from biomass burning, which is likely the dominant source, but might neglect other sources such as vehicle exhaust and coal combustion.[42−44]

https://doi.org/10.1021/acs.est.6c03997
Environ. Sci. Technol. 2026, 60, 22748−22758

Gas-particle partitioning in PACT-1D[9,37,45] is determined using uptake and evaporation rates calculated with mass transfer continuum regime kinetics[46] and the Fuchs-Sutigin kinetic regime correction (Section S2).[47] Mass accommodation coefficients (Table S3) were temperature corrected (Section S3). Gas-aqueous partitioning is constrained by Henry's law (Table S4), adjusted to the ambient temperature and, for phenols, corrected for ionic strength (Section S4). Gas-particle partitioning in organic particles is governed by Pankow's adsorption model (i.e., C_i* partitioning, Table S4), adjusted to winter temperatures in Fairbanks (Section S5), and assumes activity coefficients of unity.

Photooxidant Production. Measurement-based kinetic models are the most robust tools for predicting ^{3}C*, $^1O_2$*, and $^\bullet$OH concentrations in particles.[24,48] We update the kinetic photooxidant scheme built with oxidant measurements in illuminated aqueous extracts of wintertime Fairbanks PM[8] and incorporate it into PACT-1D.

BrC Light Absorption. BrC photooxidant formation is simulated by calculating the rate constant for BrC sunlight absorption ($j_{BrC,abs}$, mol-photon mol-C^{1-} s^{-1}) between 310 and 550 nm with

$$j_{BrC,abs} = \sum_{310\ nm}^{550\ nm} (MAC_\lambda \times I'_{\lambda,AK} \times \Delta\lambda \times M_C \times (A + 1) \times 2.5) \quad (1)$$

where MAC_λ is the dissolved organic carbon (DOC)-normalized mass absorption cross section measured during ALPACA (cm^2 g-C^{-1}),[8] $I'_{\lambda,AK}$ is the measured actinic flux (mol-photon cm^{-2} nm^{-1} s^{-1}),[8] $\Delta\lambda$ is the wavelength interval (1 nm), M_C is the molecular weight of carbon (12.011 g mol^{-1}), A is the albedo (unitless), and 2.5 is a unitless factor to account for the optical confinement of sunlight inside particles.[49] Because we do not have MAC measurements of OSBrC, we assume they are equal to WSBrC MAC. Though this might be an underestimate of OSBrC MAC, the resulting ratio of $j_{BrC,abs}$ in both particle types is equal to the ratio of absorption of PM extracted into water and methanol.[50]

$^\bullet$OH and ^{3}C Production.* The first-order rate constants for $^\bullet$OH and ^{3}C* formation from brown carbon (j_{ox}, mol-ox mol-C^{1-} s^{-1}) are calculated with

$$j_{ox} = j_{BrC,abs} \times \Phi_{ox} \quad (2)$$

where Φ_{ox} is the $^\bullet$OH or ^{3}C* quantum yield measured in water extracts of ALPACA PM.[8] Φ_{3C*} represents the subset of ^{3}C* which are oxidizing, determined by their ability to react with syringol (with an oxidation potential of ∼1.17 V vs SHE).[8,26,51] Φ_{ox} were measured on composites of 2−13 daily filters and therefore have limited time resolution.[8] Because of a lack of data, we assume Φ_{ox} for OSBrC are equal to those measured in aqueous extracts.

Next, the $^\bullet$OH and ^{3}C* production rates in particles ($P_{ox,i}$, mol L^{-1} s^{-1}) are calculated using

$$P_{ox,i} = j_{ox}[DOC]_i \quad (3)$$

where $[DOC]_i$ is the concentration of dissolved organic carbon in particle-type i (i.e., either aqueous or organic particles; mol-C L^{-1}, derived in Section S6).

$^1O_2$ Production.* In PACT-1D, $^1O_2$* is produced from ^{3}C*. Φ_{1O2*} cannot be applied to (eqs 2 and 3) to calculate P_{1O2*} in particles[29] because P_{1O2*} is not proportional to DOC concentration.[24] P_{1O2*} is instead determined with

$$P_{^1O_2^*,i} = k_{3C*+O2}\left(\frac{1}{f_{ox-3C*}}\right)[^3C^*]_i[O_2]_i f_\Delta \quad (4)$$

Where k_{3C*+O2} is the second order rate constant for energy transfer of ^{3}C* and O_2 (2.8×10^{10} M^{-1} s^{-1}),[48] $f_{ox\text{-}3C*}$ is the fraction of ^{3}C* that are oxidizing (estimated as 0.35),[27] and f_Δ is the fraction of ^{3}C*-O_2 interactions that form $^1O_2$* (estimated as 0.43).[52]

Photooxidant Sinks. Table S6 includes the rate constants for the dominant photooxidant sinks.[8,24,27] We assume the rate constants are equivalent in aqueous and organic particles unless otherwise noted, because most kinetics are not known in organic particles. For $^\bullet$OH, sinks include reactions with DOC ($k_{DOC+\bullet OH}$ = 3.8(±1.9)×10^8 L mol-C^{1-} s^{-1}),[53] levoglucosan ($k_{lev+\bullet OH}$ = 2.4(±0.02)×10^9 M^{-1} s^{-1}),[54] and phenols (Table S8). ^{3}C* sinks include reactions with O_2, DOC ($k_{DOC+3C*}$ = 7.0 × 10^7 L mol-C^{1-} s^{-1}),[29] and phenols (Table S8). The major $^1O_2$* sinks are DOC ($k_{1O2*+DOC}$ = 1.6 × 10^6 L mol-C^{1-} s^{-1}, measured as described in Section S7), phenols (Table S8), and solvent deactivation. $k_{1O2*,H2O}$ is well-defined (2.76(±0.02) × 10^5 s^{-1})[55] but the equivalent value in organic particles is unknown so assumed equal to $k_{1O2*,H2O}$.

Phenolic SOA Formation. PACT-1D includes multiphase SOA formation in the gas phase, in aqueous particles, and in organic particles. Gas-phase ArOH reaction pathways are direct photodegradation (for phenolic carbonyls) and with $^\bullet$OH, O_3, and NO_3. Condensed-phase ArOH reaction pathways are direction photodegradation and with $^\bullet$OH, ^{3}C*, $^1O_2$*, O_3, and NO_3. The rate of phenolic SOA production ($P_{ox,ArOH\ SOA,p}$, molecules cm^3-air s^{-1} or mol L^{-1} s^{-1}) in phase p is

$$P_{ox,ArOHSOA,p} = k_{ox+ArOH}[ox]_p[ArOH]_p \times Y_{ox+ArOH} \quad (5)$$

where $k_{ox+ArOH}$ is the second-order rate constant of a given phenol and oxidant in the gas phase (cm^3-air molecule^{-1} s^{-1}, Table S7) or in particles (L mol^{-1} s^{-1}, Tables S8 and S9) and $Y_{ox+ArOH}$ is the SOA yield (Tables S10 and S11). Rate constants are temperature corrected (Section S9) with activation energies compiled in Tables S12 and S13. We assume equivalent rate constants in organic and aqueous particles due to a lack of measurements in organic media. For direct photodegradation reactions, $k_{ox+ArOH}[ox]_p$ is substituted with the direct photodegradation rate constant ($j_{ArOH,p}$, s^{-1}, Section S8). In aqueous particles, we account for ionic strength using Setchenow coefficients (Table S5)[56] to calculate phenol activities ($\{ArOH\}_{aq}$) and substitute them into eq 5 (Section S4). Oxidant activity coefficients in both particle types are assumed to be unity. Salts can also alter reaction kinetics,[57,58] though this is not accounted for in PACT-1D due to limited studies of this effect on reactions of ^{3}C* with phenols. We do not include a chemical sink for phenolic SOA because the polluted air-mass residence time is ∼hours,[9,36] shorter than aqueous phenolic SOA chemical lifetimes.[59] Section S10 outlines additional uncertainties.

RESULTS AND DISCUSSION

We simulate multiphase phenolic SOA formation in Fairbanks, Alaska during the ALPACA field campaign from January 28th to February 11th, 2022. This includes a 5-day pollution episode (1/29/22 to 2/3/22) during which $PM_{2.5}$ exceeded the EPA 24-h standard of 35 μg m^{-3}, followed by an extended clean period (2/4/22 to 2/11/22, Figure S4) with 10-times lower $PM_{2.5}$. Unless otherwise noted, numerical values quoted in the following text are 1:00 PM (solar noon) values averaged from 1/29/22 to 2/2/22.

Organic Aerosol

Strong surface-based inversions trap high concentrations of OA during polluted periods (Figure 2a). Field measurements show fast diurnal variability in the OA composition: OOA accounts for 17(±4)% of OA at 5:00 AM but increases to 40(±4)% at 1:00 PM during the pollution event (1/31 to 2/2, Figure S1).[11] The rapid changes in PM composition are partially explained by the short residence time of pollutants at the surface of 1−3 h.[9,36]

Sunlight Absorption by Brown Carbon

Fairbanks winter OA is rich in light-absorbing BrC, resulting in large sunlight absorption rates (Figure 2b) similar to rates in polluted urban winter sites at lower latitudes.[8,29] As reflected in measurements and implemented in PACT-1D, two-thirds of

https://doi.org/10.1021/acs.est.6c03997
Environ. Sci. Technol. 2026, 60, 22748−22758

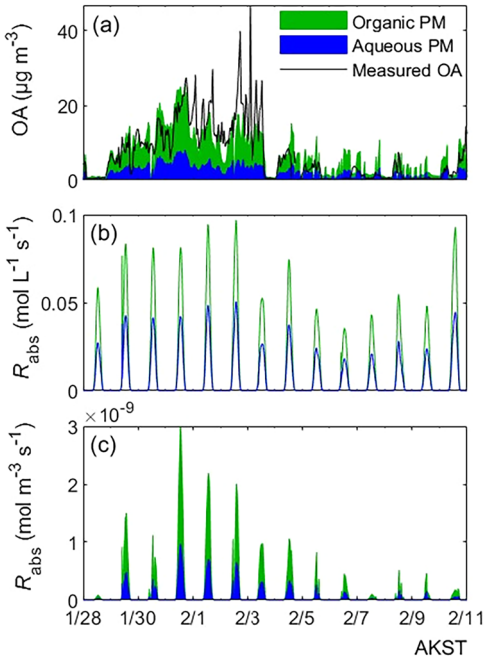

Figure 2. (a) Stacked plot of organic aerosol (OA) concentrations in aqueous (blue) and organic particles (green) overlaid with the measured hourly average OA concentration (black line).[11] (b) Line plot (i.e., not stacked) of rates of brown carbon (BrC) sunlight absorption per liter of particle volume. (c) Stacked plot of BrC sunlight absorption rates normalized to air volume.

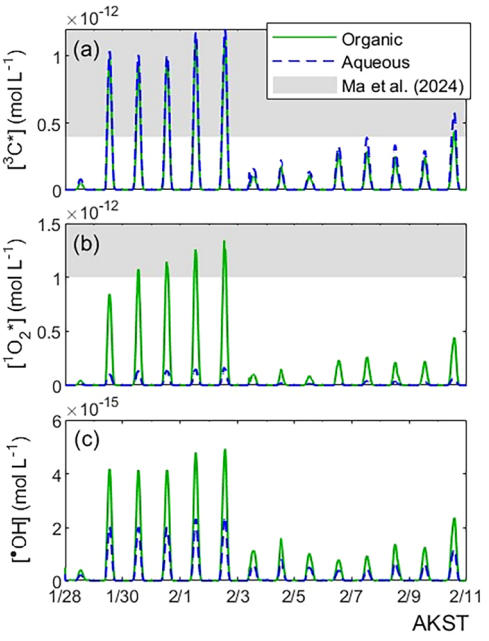

Figure 3. Steady-state concentrations of (a) ^{3}C*, (b) $^1O_2$*, and (c) •OH in aqueous (blue) and organic (green) particles. The gray-shaded regions are the ranges of oxidant concentration in particles from Davis, CA on the winter solstice, which are (0.4−13)×10^{-12} for ^{3}C*, (1−8)×10^{-12} M M for $^1O_2$*, and (8.8−13)×10^{-15} M for •OH.[29] For Panel (c), the Davis, CA values are larger than the *y*-axis range.[29]

the total BrC light absorption is by OSBrC.[50,60−63] We observe little variation in particle- volume-normalized rates of sunlight absorption by BrC across the campaign because the BrC character changes minimally between clean and polluted periods,[8] as seen in the small range of BrC MAC_{365} during ALPACA of 0.58−1.1 m^2 g-C^{1-}.[8] In contrast, the concentration of BrC-rich particles at the surface increases significantly during polluted periods. Because of this, on an air-volume-normalized basis, high OA concentrations drive an 8-factor increase in the rate of light absorption by BrC during the pollution episode (1/31) compared to the subsequent clean period (2/6 to 2/11, Figure 2c).

Particle Photooxidant Production

This work represents the first time that photooxidant production has been modeled from OSBrC. We find that oxidizing triplets are rapidly produced in both aqueous and organic particles, with highest rates during the polluted period when high BrC light absorption rates coincide with the peak ^{3}C* quantum yield (Figure S5).[8] Triplet concentrations are similar in aqueous and organic particles, with midday values of 1.1(±0.08) × 10^{-12} and 1.0(±0.08) × 10^{-12} M, respectively (Figure 3a). Though the ^{3}C* production rates in organic particles are twice as fast as in aqueous particles, the ^{3}C* lifetime in organic particles (~0.4 ns) is half the value in aqueous particles, leading to comparable concentrations in both particle types. Accounting for OSBrC doubles the total atmospheric ^{3}C* concentration and triples the total ^{3}C* production rate, demonstrating it is an important ^{3}C* source.

The dominant ^{3}C* sinks in organic particles during the pollution episode are organic carbon (67(±6)%), oxidation of phenols (32(±6)%), and energy transfer to O_2 (1(±0.2)%). Oxygen is a small triplet sink despite estimated dissolved oxygen concentrations in organic particles roughly 18 times higher than in water.[64] Phenols are treated as explicit ^{3}C* sinks distinct from DOC. While chemical reactions dominate the interaction of ^{3}C* with phenols,[18,20,25,30,65] it is unclear what fraction of triplet-DOC interactions result in chemical change of the organic molecule. Triplets can chemically react with several classes of organic compounds in addition to phenols, including anilines, alkenes, and organics with reduced sulfur atoms,[66] but some triplet-organic reactions (e.g., with dienes)[63] result in physical quenching that causes no chemical change in the organics.[66] Recent work by Hoffmann et al. assumed that triplets are only physically quenched by organic compounds,[33] but this ignores the oxidation of phenols and other organic molecules and so it underestimates the atmospheric significance of triplets.

In the aqueous particles, more than 99% of ^{3}C* are lost to organic carbon. Phenols, which again are treated as explicit ^{3}C* sinks distinct from DOC, are negligible triplet sinks in aqueous particles because high ammonium sulfate concentrations salt out ArOHs.[56] O_2 is a negligible ^{3}C* sink because O_2 concentrations in aqueous particles are much smaller than DOC concentrations. The stark difference in ^{3}C*-driven chemistry in aqueous and organic particles demonstrates that the significance of ^{3}C* chemistry depends on the availability of reactive triplet sinks such as phenols.

$^1O_2$* production is distinct in aqueous and organic particles. $^1O_2$* concentrations in organic particles are 1.1(±0.2) × 10^{-12} M, an order of magnitude higher than the 0.13(±0.02) × 10^{-12} M in aqueous particles, because of the higher O_2 concentration in organic particles. As a result, $^1O_2$* and ^{3}C* concentrations are similar in organic particles, whereas triplet concentrations in aqueous particles are 8-times larger than $^1O_2$*. In both particle types, we find significantly lower particle $^1O_2$* concentrations than past work[27,29] because our measured rate constant for $^1O_2$* interactions with organic carbon

https://doi.org/10.1021/acs.est.6c03997
Environ. Sci. Technol. 2026, 60, 22748−22758

($k_{1O2*+DOC}$ = 1.6(±0.1)×10^6 M^{-1} s^{-1}, Section S7) is 16-times higher than previous estimates.[24,27,29]

In PACT-1D, $^1O_2$* production in particles is determined using the reaction rate of ^{3}C* and O_2 (eq 4), because Φ_{1O2*} in particles differ from dilute solution.[8,24,27] Indeed, the effective $^1O_2$*quantum yields in ALW modeled here are 200 to 8000 times smaller than those measured in dilute extracts of Fairbanks PM (Figure S6). This agrees with previous kinetic modeling of $^1O_2$* in ALW: high concentrations of DOC suppress ^{3}C* concentrations, limiting $^1O_2$* production, and become an important $^1O_2$* sink.[24]

Quenching by organic carbon is the dominant $^1O_2$* sink in aqueous and organic particles, accounting for more than 98% of $^1O_2$* loss; it is unclear what fraction of these DOC−$^1O_2$* interactions are chemical reaction versus physical quenching. Chemical reactions with phenols are a negligible $^1O_2$* sink, resulting in insignificant ArOH oxidation by $^1O_2$*. Though not included here, other compound classes with larger $^1O_2$* chemical reaction rate constants, such as substituted furans,[32] may be more important $^1O_2$* sinks.

Both aqueous and organic particles produce significant daytime •OH. •OH production and loss rates are two times faster in organic particles than aqueous particles, leading to comparable steady-state •OH concentrations in both particle types (Figure 3). Based on measurements,[8] the dominant aqueous •OH sources in Fairbanks are reactions of HOOH with reduced iron and copper, with minor contributions from nitrate and nitrite photolysis. We capture these •OH sources in PACT-1D using measured •OH quantum yields.[8] Unspeciated DOC is the dominant •OH sink in particles, accounting for 90(±1)% and 89(±3)% of •OH loss in aqueous and organic particles, respectively. Chemical reactions with phenols are a negligible •OH sink in aqueous particles, but account for up to 11(±3)% of •OH loss in organic particles.

During clean periods, BrC photooxidant chemistry is slow for all three oxidants. Compared to the polluted period described above, photooxidant concentrations within particles are 4−8 times lower during clean periods due to smaller MAC_λ and lower Φ_{ox}. More importantly, low OA concentrations lead to small air-volume-normalized photooxidant concentrations during clean periods (Figure S7).

Biomass-Burning Phenols

The model includes 34 semivolatile phenols, with a total concentration up to 5 μg m^{-3} (Figure 4a); structures of each ArOH are listed in Table S1. Higher-volatility species such as phenol (C_6H_5OH) and cresols are the most abundant ArOHs in wood smoke (Table S2), making the gas phase the dominant ArOH reservoir. The average simulated nighttime gas-phase mass fraction of phenols is 63(±7)%, though at 1:00 PM this increases to 95(±2)%. Organic particles are the other important ArOH reservoir, containing 4−49% of the total phenol mass during the pollution event. In contrast, aqueous particles are a negligible phenol reservoir. Though K_H are roughly 150-times higher at −20 °C than at 25 °C, high ionic strengths in aqueous particles salt out ArOHs, effecting a 10−90 fold decrease in K_H.[56] We do not consider the poorly understood temperature dependence of Setschenow coefficients,[67−69] which should be characterized to assess aqueous particles as a phenol reservoir.

Gas-Particle Partitioning. Phenols have a wide range of volatilities, with simulated saturation concentrations (C_i*) ranging from 0.05 to 4 × 10^4 μg m^{-3} at 8:00 AM on 1/31/22,

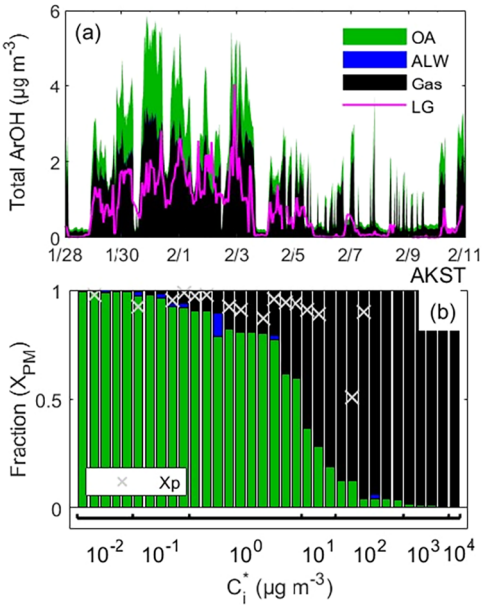

Figure 4. (a) Summed concentrations of all 34 modeled biomass-burning phenols (ArOH) in the polluted surface layer (1−3 m). Concentrations are shown as stacked values in the gas phase (black), aerosol liquid water (ALW, blue but not visible at this scale), and organic aerosol (OA, green); the magenta line is an overlay of measured levoglucosan (LG) concentrations.[11] (b) Modeled gas- and particle-phase fractions of all 34 phenols as a function of saturation concentration (C_i*). Bars are colored to show fractions in the gas phase (black), aqueous particles (blue), and organic particles (green) at 8:00 AM on 1/31/2022 (−34 °C). The gray 'x's denote the measured particle-phase fraction (X_{PM}) of 16 phenols for the same day and time.[70] Figure S8 depicts an analogous plot for 1:00 PM on 1/31/2022 (−30 °C). Phenol names organized by C_i* are in Table S14.

resulting in modeled particle-phase fractions (X_{PM}) from <0.3% to 99% (Figure 4b). At night, gas-particle partitioning in the model approaches equilibrium because ArOH chemical loss is slow. Two instruments were used to measure gas-particle partitioning of semivolatile compounds during ALPACA, with SV-TAG finding almost 100% of phenols in particles (Figure 4b)[70] and the CHARON-PTR reporting X_{PM} of semivolatile compounds (including phenols) between 50 and 80%.[71] Despite PACT-1D not accounting for nonideal behavior (i.e., viscosity),[72−74] simulated nighttime X_{PM} values generally fall within the wide measured range.

During daylight, rapid photochemical phenol loss in particles makes modeled X_{PM} values lower than nighttime values, which are near equilibrium (Figure S8b). This chemistry is driven by triplets which account for 98(±1%) of phenol loss. Rapid condensed-phase chemistry can be fast enough that it competes against mass transport from the gas phase, limiting particle ArOH concentrations and suppressing the steady-state X_{PM}.[75] Sensitivity tests reveal that the phase in which phenols are emitted impacts X_{PM} (Figures S9a−c). Under our base case, where we assume all phenols are emitted in organic particles, the average X_{PM} of particles in the polluted surface layer decreases on average (±1σ) by 8(±9)% between 8 AM and 1 PM (Figure S8) because of mass-transport limitations. In our limiting case where phenols are emitted into the gas phase—a scenario which is unrealistic but reveals this sensitivity in our simulation, the average X_{PM} in the polluted surface layer decreases by 37(±28)% from 8 AM to 1 PM,

https://doi.org/10.1021/acs.est.6c03997
Environ. Sci. Technol. 2026, 60, 22748−22758

because chemical loss of phenols in particles competes against uptake of phenols from the gas phase. In this extreme sensitivity test, lower particle phase phenol concentrations also lead to an average 33(±15)% decrease in the phenolic SOA concentration. The phase of phenol emissions does not significantly affect other model results, including nighttime X_{PM} values and photooxidant concentrations.

Atmospheric Lifetimes of Phenols. During the pollution event, rapid particle photochemistry leads to short midday phenol lifetimes. The median phenol lifetimes is 11 min when considering the total (gaseous and particulate) amount of a given phenol (Figure S10), which is significantly shorter than the airmass lifetime (1−3 h).[9] Nighttime chemical ArOH loss is negligible, with a median phenol lifetime of several days.

Lifetimes are only short in organic particles (Figures S11 and S12), revealing that photochemistry in organic particles drives the short ArOH atmospheric lifetimes. Organic particles dominate phenol loss because they are a significant phenol reservoir and have fast chemical loss. Aqueous particles are a minor phenol sink because they are a negligible phenol reservoir, a result of high ionic strengths. Though the gas phase is an important ArOH reservoir, chemical loss is slow, leading to long gas-phase phenol chemical lifetimes. In organic particles, all phenols undergo rapid oxidation (Figure S13a−c), but the least volatile species have the highest values of X_{PM} and therefore the shortest atmospheric lifetimes with respect to the total (i.e., gas and particle) amount of phenol (Figure S13d−f).

Multiphase Phenolic SOA Formation

Phenolic SOA is formed when a phenol is oxidized to low-volatility products, either by gas- or particle-phase reactions. For simplicity, here we consider all phenol oxidation reactions as a source of SOA even though oxidation of ArOH that predominantly exist inside particles (i.e., high X_{PM}) represents the chemical transformation of OA rather than the formation of new PM mass.

The mass concentration of phenolic SOA formed during daytime peaks during the pollution event at 4.5 μg m^{-3} and accounts for up to 34% of the measured oxidized organic aerosol (OOA, Figure 5a).[11] HMS and other organo-S(IV) adducts are also expected to be OOA, with up to 2.1 μg m^{-3} measured during the pollution event.[6] Accordingly, our simulations demonstrate that phenolic SOA is more significant than HMS as a source of secondary PM.[11] During the night, photochemistry ceases which leads to low simulated phenolic SOA concentrations of 0.07(±0.02) μg m^{-3} at midnight. When measured OOA is normalized by levoglucosan (LG) to remove variability in emissions and meteorology (Figure 5b), the data reveal a strong correlation between the measured OOA and modeled phenolic SOA during the pollution event. When the correlation is weak, we suspect that unknown sources dominate OOA formation.

The average daytime (9 AM to 5 PM) phenolic SOA formation rate during the pollution episode was 6(±2) μg m^{-3} hr^{-1}. In our model, 98(±1)% of phenolic SOA is formed in organic particles (Figure 5a), nearly all from ^{3}C* (Figure 5c). Aqueous particles are minor sources of phenolic SOA due to high ionic strengths limiting aqueous phenol concentrations. $^1O_2$* does not form significant phenolic SOA because of small reaction rate constants. This disagrees with recent work that suggested similar phenolic SOA formation from $^1O_2$* and ^{3}C* in ALW;[18] the authors used $^1O_2$* concentrations in ALW from

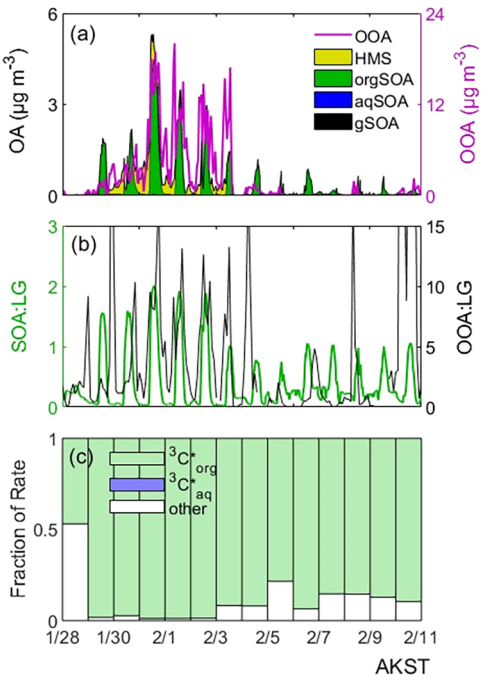

Figure 5. (a) Stacked plot of modeled phenolic secondary organic aerosol (SOA) concentrations in the polluted layer (1−3 m above ground level) formed in the gas phase (gSOA, black), aqueous particles (aqSOA, blue), and organic particles (orgSOA, green), as well as the simulated hydroxymethanesulfonate (HMS) reported by Kuhn et al.[9] (yellow) on the left *y*-axis. The magenta line is an overlay of the measured 1 h average concentration of oxidized organic aerosol (OOA, right *y*-axis).[11] Note the difference in the *y*-axis scales. (b) Timeseries of modeled phenolic SOA normalized by simulated levoglucosan (LG) (green, left axis) and 2-h average of OOA normalized to measured LG (black, right axis). (c) Bar chart depicting fraction of phenolic SOA formation rate from ^{3}C* in organic particles (green), ^{3}C* in aqueous particles (blue), and all other pathways (white). In panels (a) and (c), the blue and black contributions are too small to be seen.

Kaur et al.,[27] which we recently showed are 10 to 100 times too high.[24] Gas and particle •OH are negligible ArOH oxidants because •OH concentrations are too low to form significant phenolic SOA. Similarly, gas and particle reactions of ozone are slow because high NO concentrations titrate ozone to less than 1 ppb, as elucidated by measurements and by PACT-1D simulations.[9,39,76] These low ozone concentrations in turn restrict nitrate radical formation, explaining the negligible nighttime phenolic SOA from ozone and nitrate radical.

As shown in Figure 6, SOA formation is dominated by a small number of phenol species. During the day, five phenols—syringol, guaiacyl acetone, ethylsyringol, tyrosol, and homovanillic acid—account for 49% of the total phenolic SOA mass. The contribution of a given phenol to SOA formation is largely a function of two factors: the emissions rate (Figure 6a) and their saturation concentration (Figure 6b), which control phenol concentrations in organic particles (Figure S14). The relative importance of an individual BB phenol as a source of SOA is a product of the cold and OA-rich conditions of Fairbanks during winter. For example, under relatively clean conditions (OA = 5 μg m^{-3}) at 20 °C, 1.9% percent of syringol should be present in organic particles, but under polluted ALPACA conditions (25 μg m^{-3} OA and −30 °C), the value increases to 18%, accelerating SOA formation.

https://doi.org/10.1021/acs.est.6c03997
Environ. Sci. Technol. 2026, 60, 22748−22758

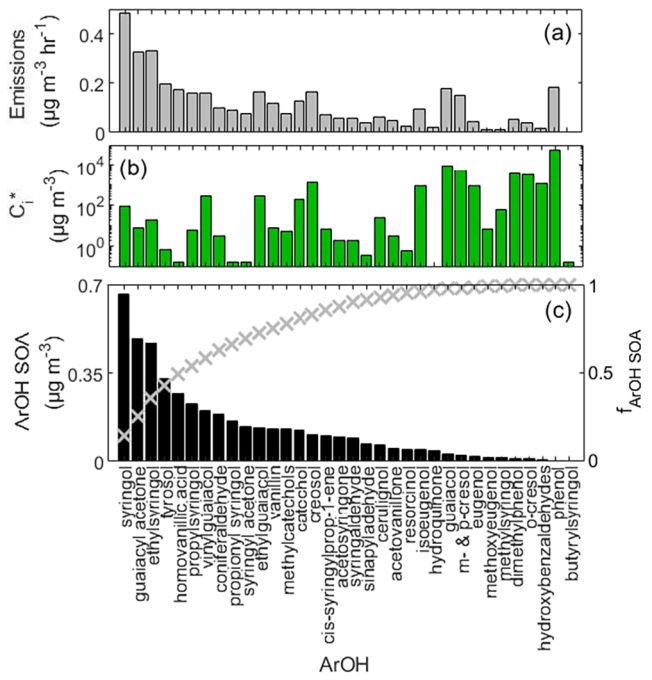

Figure 6. (a) Phenol emission rates, (b) phenol saturation concentrations at −30 °C (on a log scale), and (c) concentrations of secondary organic aerosol (ArOH SOA) formed from individual phenols, organized on the *x*-axis by SOA formation rate at 1:00 PM on 1/31/2022. In panel (c), the gray symbols (right *y*-axis) show the cumulative fraction of phenolic SOA formed by all phenols up to, and including, that species.

Thus, the relative and absolute importance of individual phenols as source of SOA will depend on location, season, and conditions (e.g., temperature, OA, and BrC).

IMPLICATIONS AND FUTURE DIRECTIONS

Our simulations of a winter pollution event in Fairbanks, Alaska demonstrate rapid daytime phenolic SOA formation, predominantly from BrC-derived triplet excited states in organic particles. In contrast to the traditional paradigm that SOA formation is mostly significant under conditions of high temperature and abundant sunlight, we find significant amounts of SOA formation in the winter in a location with very low temperatures and very little sunlight. This rapid SOA formation is possible because of high woodsmoke emissions, significant light absorption by brown carbon, and because surface-based inversions trap high concentrations of phenols and biomass burning particles, enhancing phenolic SOA formation rates. Moreover, accounting for OSBrC doubles the total atmospheric ^{3}C* concentration and triples the total ^{3}C* production rate, revealing the important role of OSBrC as a ^{3}C* source. The transport model further demonstrates that phenolic SOA formation outcompetes the short air-mass residence time in the polluted surface layer, which otherwise fundamentally limits secondary chemistry. The results highlight the unexpected ability of brown carbon photochemistry to transform the composition of organic aerosol in high-latitude cities which notoriously experience severe winter pollution events.

We expect the largest sources to be steady-state ^{3}C* concentrations and particle-phase phenol concentrations. PACT-1D incorporates state-of-the-art kinetic models to predict photooxidant concentrations,[8,24,27] but direct measurements of ^{3}C* in droplets are needed to validate these kinetic models. Similarly, while simulated phenol concentrations are validated by measurements (Figure S16),[70] improved high time resolution gas and particle measurements of the most important SOA precursors are needed to confirm simulated concentrations. A quantitative understanding of particle viscosity is essential for characterizing wintertime multiphase chemistry during, although viscosity was beyond our scope due to the abundant evidence of multiphase chemistry.[5−10] Furthermore, identifying ambient phenolic SOA requires a technique to distinguishing phenolic SOA from the ambient OA. Additional laboratory measurements are needed to understand winter phenolic SOA, including temperature-dependent kinetics and SOA yields from phenol oxidation, especially via oxidizing triplet excited states. Lastly, more studies regarding the (photo)chemistry of OSBrC are needed, with initial studies suggesting OSBrC has higher photooxidant quantum yields than WSBrC,[35] indicating that our simulations likely underestimate photooxidation production in OA.

ASSOCIATED CONTENT

Supporting Information

The Supporting Information is available free of charge at https://pubs.acs.org/doi/10.1021/acs.est.6c03997.

Additional descriptions of the PACT-1D model and its results, including simulated organic aerosol, aerosol liquid water, and dissolved organic carbon concentrations; ArOH emissions; gas-particle partitioning of ArOH; photooxidant production and the new $k_{1O2*+DOC}$ measurement; phenolic SOA formation kinetics and yields phenol lifetimes; and measured oxidized organic aerosol concentrations (PDF)

AUTHOR INFORMATION

Corresponding Authors

Laura M. D. Heinlein − *Department of Land, Air, and Water Resources, University of California, Davis, California 95616, United States;* orcid.org/0009-0005-6716-4661; Email: lmheinlein@ucdavis.edu

Cort Anastasio − *Department of Land, Air, and Water Resources, University of California, Davis, California 95616, United States;* orcid.org/0000-0002-5373-0459; Email: canastasio@ucdavis.edu

Authors

Jonas Kuhn − *Department of Atmospheric and Oceanic Sciences, University of California, Los Angeles, California 90095, United States;* orcid.org/0000-0002-6953-3281

Amna Ijaz − *Aix Marseille Univ, CNRS, LCE, 13331 Marseille, France;* Present Address: Atmospheric, Climate, & Earth Sciences Division, Pacific Northwest National Laboratory, Richland, Washington 99354, United States

Brice Temime-Roussel − *Aix Marseille Univ, CNRS, LCE, 13331 Marseille, France*

Karolina Cysneiros de Carvalho − *McKelvey School of Engineering & Applied Science, Washington University in St. Louis, St. Louis, Missouri 63130, United States;* Present Address: Environmental Sciences Department, University of California, Riverside, California 92521, United States

Mallory Liebes − *Utah Water Research Laboratory, Department of Civil and Environmental Engineering, Utah State University, Logan, Utah 84321, United States*

https://doi.org/10.1021/acs.est.6c03997
Environ. Sci. Technol. 2026, 60, 22748−22758

Fangzhou Guo − *Department of Earth & Atmospheric Sciences, University of Houston, Houston, Texas 77204, United States;* Present Address: Center for Atmospheric and Environmental Chemistry, Aerodyne Research Inc., Billerica, Massachusetts 01821, United States; orcid.org/0000-0003-3854-038X

James H. Flynn, III − *Department of Earth & Atmospheric Sciences, University of Houston, Houston, Texas 77204, United States*

Kyle Moor − *Utah Water Research Laboratory, Department of Civil and Environmental Engineering, Utah State University, Logan, Utah 84321, United States;* orcid.org/0000-0002-3152-0354

Brent Williams − *McKelvey School of Engineering & Applied Science, Washington University in St. Louis, St. Louis, Missouri 63130, United States;* Present Address: Department of Soil, Water, and Climate, University of Minnesota, Minneapolis, Minnesota 55455, United States

Barbara D'Anna − *Aix Marseille Univ, CNRS, LCE, 13331 Marseille, France*

Jochen Stutz − *Department of Atmospheric and Oceanic Sciences, University of California, Los Angeles, California 90095, United States*

Complete contact information is available at: https://pubs.acs.org/10.1021/acs.est.6c03997

Notes

The authors declare no competing financial interest.

■ ACKNOWLEDGMENTS

We gratefully acknowledge funding from the National Science Foundation (grant numbers AGS-2220307, AGS-2109011, and AGS-2109240). We thank the entire ALPACA team for data collection and collaboration, especially highlighting James H. Flynn III and Fangzhou Guo for their actinic flux and albedo measurements. We also thank Angelina Petersen, Surbhi Gupta, Tran Nguyen, and Bill Simpson for supplying Alaska birch wood and preparing the D_2O wood smoke extract used to measure $k_{^1O_2^*+DOC}$. We also gratefully acknowledge Mallory Liebes from the Water Research Laboratory for conducting singlet oxygen phosphorescence experiments to measure $k_{^1O_2^*+DOC}$.

■ REFERENCES

(1) American Lung Association. Most Polluted Cities 2026 https://www.lung.org/research/sota/key-findings/most-polluted-places. [Last accessed: January 14, 2026].

(2) Simpson, W.; Law, K.; Schmale, J.; Pratt, K.; Arnold, S.; Mao, J.; Alexander, B.; Anenberg, S.; Baklanov, A.; Bell, D.; Brown, S.; Creamean, J.; de Boer, G.; DeCarlo, P.; Descari, S.; Elleman, R.; Flynn, J.; Fochesatto, J.; Ganzenfeld, L.; Griffin, R.; Järvi, L.; Kaspari, S.; Konstantinov, P.; Murphy, J.; Petäjä, T.; Pye, H.; Jean-Christophe Raut, J.-C.; Roberts, T.; Shiraiwa, M.; Stutz, J.; Thomas, J.; Thornton, J.; Weber, R.; Webley, P.; Williams, B. Alaskan Layered Pollution And Chemical Analysis (ALPACA) White Paper. 2019.

(3) Simpson, W. R.; Mao, J.; Fochesatto, G. J.; Law, K. S.; DeCarlo, P. F.; Schmale, J.; Pratt, K. A.; Arnold, S. R.; Stutz, J.; Dibb, J. E.; Creamean, J. M.; Weber, R. J.; Williams, B. J.; Alexander, B.; Hu, L.; Yokelson, R. J.; Shiraiwa, M.; Decesari, S.; Anastasio, C.; D'Anna, B.; Gilliam, R. C.; Nenes, A.; St Clair, J. M.; Trost, B.; Flynn, J. H.; Savarino, J.; Conner, L. D.; Kettle, N.; Heeringa, K. M.; Albertin, S.; Baccarini, A.; Barret, B.; Battaglia, M. A.; Bekki, S.; Brado, T. J.; Brett, N.; Brus, D.; Campbell, J. R.; Cesler-Maloney, M.; Cooperdock, S.; Cysneiros de Carvalho, K.; Delbarre, H.; DeMott, P. J.; Dennehy, C. J. S.; Dieudonné, E.; Dingilian, K. K.; Donateo, A.; Doulgeris, K. M.; Edwards, K. C.; Fahey, K.; Fang, T.; Guo, F.; Heinlein, L. M. D.; Holen, A. L.; Huff, D.; Ijaz, A.; Johnson, S.; Kapur, S.; Ketcherside, D. T.; Levin, E.; Lill, E.; Moon, A. R.; Onishi, T.; Pappaccogli, G.; Perkins, R.; Pohorsky, R.; Raut, J.-C.; Ravetta, F.; Roberts, T.; Robinson, E. S.; Scoto, F.; Selimovic, V.; Sunday, M. O.; Temime-Roussel, B.; Tian, X.; Wu, J.; Yang, Y. Overview of the Alaskan Layered Pollution and Chemical Analysis (ALPACA) Field Experiment. *ACS ES&T Air* **2024**, *1* (3), 200−222.

(4) Haskins, J. D.; Lopez-Hilfiker, F. D.; Lee, B. H.; Shah, V.; Wolfe, G. M.; DiGangi, J.; Fibiger, D.; McDuffie, E. E.; Veres, P.; Schroder, J. C.; Campuzano-Jost, P.; Day, D. A.; Jimenez, J. L.; Weinheimer, A.; Sparks, T.; Cohen, R. C.; Campos, T.; Sullivan, A.; Guo, H.; Weber, R.; Dibb, J.; Green, J.; Fiddler, M.; Bililign, S.; Jaeglé, L.; Brown, S. S.; Thornton, J. A. Anthropogenic Control Over Wintertime Oxidation of Atmospheric Pollutants. *Geophys. Res. Lett.* **2019**, *46* (24), 14826−14835.

(5) Sunday, M. O.; Heinlein, L. M. D.; He, J.; Moon, A.; Kapur, S.; Fang, T.; Edwards, K. C.; Guo, F.; Dibb, J.; Flynn III, J. H.; Alexander, B.; Shiraiwa, M.; Anastasio, C. Hydrogen Peroxide Photoformation in Particulate Matter and Its Contribution to S(IV) Oxidation During Winter in Fairbanks, Alaska. *Atmos. Chem. Phys.* **2025**, *25* (10), 5087−5100.

(6) Moon, A.; Jongebloed, U.; Dingilian, K. K.; Schauer, A. J.; Chan, Y.-C.; Cesler-Maloney, M.; Simpson, W. R.; Weber, R. J.; Tsiang, L.; Yazbeck, F.; Zhai, S.; Wedum, A.; Turner, A. J.; Albertin, S.; Bekki, S.; Savarino, J.; Gribanov, K.; Pratt, K. A.; Costa, E. J.; Anastasio, C.; Sunday, M. O.; Heinlein, L. M. D.; Mao, J.; Alexander, B. Primary Sulfate Is the Dominant Source of Particulate Sulfate during Winter in Fairbanks, Alaska. *ES&T Air* **2024**, *1* (3), 139−149.

(7) Dingilian, K.; Hebert, E.; Battaglia, M.; Campbell, J. R.; Cesler-Maloney, M.; Simpson, W.; St Clair, J. M.; Dibb, J.; Temime-Roussel, B.; D'Anna, B.; Moon, A.; Alexander, B.; Yang, Y.; Nenes, A.; Mao, J.; Weber, R. J. Hydroxymethanesulfonate and Sulfur(IV) in Fairbanks Winter During the ALPACA Study. *ACS ES&T Air* **2024**, *1* (7), 646−659.

(8) Heinlein, L. M. D.; He, J.; Sunday, M. O.; Guo, F.; Campbell, J.; Moon, A.; Kapur, S.; Fang, T.; Edwards, K.; Cesler-Maloney, M.; Burns, A. J.; Dibb, J.; Simpson, W.; Shiraiwa, M.; Alexander, B.; Mao, J.; Flynn III, J. H.; Stutz, J.; Anastasio, C. Surprisingly Robust Photochemistry in Subarctic Particles During Winter: Evidence from Photooxidants. *Atmos. Chem. Phys.* **2025**, *25* (16), 9561−9581.

(9) Kuhn, J.; Heinlein, L. M. D.; Cesler-Maloney, M.; Sunday, M. O.; Guo, F.; Flynn, J. H.; Moon, A.; Alexander, B.; Simpson, W. R.; Anastasio, C.; Stutz, J. Atmospheric Mixing Controls Air Pollution Chemistry and Mitigation Efficacy in High-Latitude Cities. *Environ. Sci. Technol.* **2026**, *60*, 21104−21112.

(10) Holen, A. L.; Wu, J.; Forshee, L.; Dingilian, K. K.; Selimovic, V.; Battaglia, M. A.; Robinson, E. S.; Cysneiros de Carvalho, K.; Ketcherside, D. T.; Campbell, J. R.; Moon, A.; Alexander, B.; Simpson, W. R.; Mao, J.; Hu, L.; Williams, B. J.; DeCarlo, P. F.; Weber, R. J.; Pratt, K. A. Quantifying Contributions of Sulfate, Hydroxymethanesulfonate, and Additional S(IV) Compounds to Wintertime Aerosol Particles. *ACS ES&T Air* **2025**, *2* (11), 2588−2602.

(11) Ijaz, A.; Temime-Roussel, B.; Chazeau, B.; Albertin, S.; Arnold, S. R.; Barret, B.; Bekki, S.; Brett, N.; Cesler-Maloney, M.; Dieudonne, E.; Dingilian, K. K.; Fochesatto, J. G.; Mao, J.; Moon, A.; Savarino, J.; Simpson, W.; Weber, R. J.; Law, K. S.; D'Anna, B. Complementary Aerosol Mass Spectrometry Elucidates Sources of Wintertime Sub-Micron Particle Pollution in Fairbanks, Alaska, during ALPACA 2022. *Atmos. Chem. Phys.* **2025**, *25* (19), 11789−11811.

(12) Robinson, E. S.; Battaglia, M., Jr.; Campbell, J. R.; Cesler-Maloney, M.; Simpson, W.; Mao, J.; Weber, R. J.; DeCarlo, P. F. Multi-Year, High-Time Resolution Aerosol Chemical Composition and Mass Measurements from Fairbanks, Alaska. *Environ. Sci.: Atmos.* **2024**, *4* (6), 685−698.

(13) Ward, T.; Trost, B.; Conner, J.; Flanagan, J.; Jayanty, R. K. M. Source Apportionment of PM2.5 in a Subarctic Airshed - Fairbanks, Alaska. *Aerosol Air Qual. Res.* **2012**, *12* (4), 536−543.
(14) Robinson, E. S.; Cesler-Maloney, M.; Tan, X.; Mao, J.; Simpson, W.; DeCarlo, P. F. Wintertime Spatial Patterns of Particulate Matter in Fairbanks, AK during ALPACA 2022. *Environ. Sci.: Atmos.* **2023**, *3*, 568−580.
(15) Wang, Q.; Liu, T.; Xu, W.; Wang, J.; Ge, D.; Zhu, C.; Ren, C.; Wang, J.; Zha, Q.; Qi, X.; Nie, W.; Chi, X.; Lou, S.; Huang, X.; Ding, A. Characteristics and Processing of Aqueous Secondary Organic Aerosols during Autumn in Suburban Eastern China: Role of Aerosol Liquid Water, Aerosol Acidity, and Photochemistry. *Atmos. Chem. Phys.* **2026**, *26* (4), 3185−3194.
(16) Fine, P. M.; Cass, G. R.; Simoneit, B. R. T. Chemical Characterization of Fine Particle Emissions from the Fireplace Combustion of Woods Grown in the Southern United States. *Environ. Sci. Technol.* **2002**, *36* (7), 1442−1451.
(17) Schauer, J. J.; Kleeman, M. J.; Cass, G. R.; Simoneit, B. R. T. Measurement of Emissions from Air Pollution Sources. 3. C1-C29 Organic Compounds from Fireplace Combustion of Wood. *Environ. Sci. Technol.* **2001**, *35* (9), 1716−1728.
(18) Xiao, Y.; Hu, M.; Li, X.; Zong, T.; Xu, N.; Hu, S.; Zeng, L.; Chen, S.; Song, Y.; Guo, S.; Wu, Z. Aqueous Secondary Organic Aerosol Formation Attributed to Phenols from Biomass Burning. *Sci. Total Environ.* **2022**, *847*, No. 157582.
(19) Smith, J. D.; Kinney, H.; Anastasio, C. Aqueous Benzene-Diols React with an Organic Triplet Excited State and Hydroxyl Radical to Form Secondary Organic Aerosol. *Phys. Chem. Chem. Phys.* **2015**, *17* (15), 10227−10237.
(20) Ma, L.; Guzman, C.; Niedek, C.; Tran, T.; Zhang, Q.; Anastasio, C. Kinetics and Mass Yields of Aqueous Secondary Organic Aerosol from Highly Substituted Phenols Reacting with a Triplet Excited State. *Environ. Sci. Technol.* **2021**, *55* (9), 5772−5781.
(21) Arciva, S.; Niedek, C.; Mavis, C.; Yoon, M.; Sanchez, M. E.; Zhang, Q.; Anastasio, C. Aqueous ·OH Oxidation of Highly Substituted Phenols as a Source of Secondary Organic Aerosol. *Environ. Sci. Technol.* **2022**, *56* (14), 9959−9967.
(22) Li, F.; Zhou, S.; Du, L.; Zhao, J.; Hang, J.; Wang, X. Aqueous-Phase Chemistry of Atmospheric Phenolic Compounds: A Critical Review of Laboratory Studies. *Sci. Total Environ.* **2023**, *856*, No. 158895.
(23) Gilardoni, S.; Massoli, P.; Paglione, M.; Giulianelli, L.; Carbone, C.; Rinaldi, M.; Decesari, S.; Sandrini, S.; Costabile, F.; Gobbi, G. P.; Pietrogrande, M. C.; Visentin, M.; Scotto, F.; Fuzzi, S.; Facchini, M. C. Direct Observation of Aqueous Secondary Organic Aerosol from Biomass-Burning Emissions. *Proc. Natl. Acad. Sci. U.S.A.* **2016**, *113* (36), 10013−10018.
(24) Ma, L.; Worland, R.; Jiang, W.; Niedek, C.; Guzman, C.; Bein, K. J.; Zhang, Q.; Anastasio, C. Predicting Photooxidant Concentrations in Aerosol Liquid Water Based on Laboratory Extracts of Ambient Particles. *Atmos. Chem. Phys.* **2023**, *23* (15), 8805−8821.
(25) Zhang, J.; Shrivastava, M.; Ma, L.; Jiang, W.; Anastasio, C.; Zhang, Q.; Zelenyuk, A. Modeling Novel Aqueous Particle and Cloud Chemistry Processes of Biomass Burning Phenols and Their Potential to Form Secondary Organic Aerosols. *Environ. Sci. Technol.* **2024**, *58* (8), 3776−3786.
(26) Kaur, R.; Anastasio, C. First Measurements of Organic Triplet Excited States in Atmospheric Waters. *Environ. Sci. Technol.* **2018**, *52* (9), 5218−5226.
(27) Kaur, R.; Labins, J. R.; Helbock, S. S.; Jiang, W.; Bein, K. J.; Zhang, Q.; Anastasio, C. Photooxidants from Brown Carbon and Other Chromophores in Illuminated Particle Extracts. *Atmos. Chem. Phys.* **2019**, *19* (9), 6579−6594.
(28) Petersen-Sonn, E. A.; Brigante, M.; Deguillaume, L.; Jaffrezo, J. L.; George, C. Tropospheric Multiphase Chemistry: Excited Triplet States Compete with OH Radicals and Singlet Molecular Oxygen. *ACS Earth Space Chem.* **2025**, *9* (3), 533−544.
(29) Ma, L.; Worland, R.; Heinlein, L.; Guzman, C.; Jiang, W.; Niedek, C.; Bein, K. J.; Zhang, Q.; Anastasio, C. Seasonal Variations in Photooxidant Formation and Light Absorption in Aqueous Extracts of Ambient Particles. *Atmos. Chem. Phys.* **2024**, *24* (1), 1−21.
(30) Smith, J. D.; Sio, V.; Yu, L.; Zhang, Q.; Anastasio, C. Secondary Organic Aerosol Production from Aqueous Reactions of Atmospheric Phenols with an Organic Triplet Excited State. *Environ. Sci. Technol.* **2014**, *48* (2), 1049−1057.
(31) Chen, Y.; Li, N.; Li, X.; Tao, Y.; Luo, S.; Zhao, Z.; Ma, S.; Huang, H.; Chen, Y.; Ye, Z.; Ge, X. Secondary Organic Aerosol Formation from ^{3}C*-Initiated Oxidation of 4-Ethylguaiacol in Atmospheric Aqueous-Phase. *Sci. Total Environ.* **2020**, *723*, No. 137953.
(32) Arciva, S.; Zhou, Y.; Jiang, W.; Ross, A.; Zhang, Q.; Anastasio, C. Aqueous Oxidation of Biomass-Burning Furans by Singlet Molecular Oxygen ($^1O_2$*). *Environ. Sci. Technol.* **2025**, *59* (21), 10357−10367.
(33) Hoffmann, E. H.; Tilgner, A.; Felber, T.; Aiyuk, M. B. E.; Schaefer, T.; Herrmann, H. Modeling the Tropospheric Aqueous-Phase Chemistry of Photosensitizers under Wildfire-Plume and Urban Conditions with CAPRAM-PS1.0. *ACS Earth Space Chem.* **2025**, *9* (6), 1593−1606.
(34) Michael, S.; Laura, H.; Junwei, H.; Sukriti, K.et al. Photoformation of Hydrogen Peroxide by Water- and Organic-Soluble Chromophores in Ambient Particles *In preparation*.
(35) Sardena, C.; Gemmell, K. J.; Zhang, J.; Jiang, F.; Saathoff, H.; Bell, D. M.; Borduas-Dedekind, N. Singlet Oxygen and Triplet Excited State Organics Produced by Primary Biomass Burning Organic Aerosol from Wood, Dung, Straw, and Plastic Fuels: Role of Solvent-Dependent Photochemistry. *ACS ES&T Air.* **2026**, *3* (2), 611−626.
(36) Cesler-Maloney, M.; Simpson, W.; Kuhn, J.; Stutz, J.; Thomas, J.; Roberts, T.; Huff, D.; Cooperdock, S. Shallow Boundary Layer Heights Controlled by the Surface-Based Temperature Inversion Strength Are Responsible for Trapping Home Heating Emissions near the Ground Level in Fairbanks, Alaska. 2024 DOI: 10.5194/egusphere-2023-3082.
(37) Tuite, K.; Thomas, J. L.; Veres, P. R.; Roberts, J. M.; Stevens, P. S.; Griffith, S. M.; Dusanter, S.; Flynn, J. H.; Ahmed, S.; Emmons, L.; Kim, S. W.; Washenfelder, R.; Young, C.; Tsai, C.; Pikelnaya, O.; Stutz, J. Quantifying Nitrous Acid Formation Mechanisms Using Measured Vertical Profiles During the CalNex 2010 Campaign and 1D Column Modeling. *J. Geophys. Res.: Atmos.* **2021**, *126* (13), No. e2021JD034689, DOI: 10.1029/2021JD034689.
(38) Kuhn, J.; Stutz, J.; Bartels-Rausch, T.; Thomas, J. L.; Cesler-Maloney, M.; Simpson, W.; Dibb, J. E.; Heinlein, L. M. D.; Anastasio, C. The Interplay between Snow and Polluted Air Masses in Cold Urban Environments. *Faraday Discuss.* **2025**, *258*, 502−520.
(39) Cesler-Maloney, M.; Simpson, W. R.; Miles, T.; Mao, J.; Law, K. S.; Roberts, T. J. Differences in Ozone and Particulate Matter Between Ground Level and 20 m Aloft Are Frequent During Wintertime Surface-Based Temperature Inversions in Fairbanks, Alaska. *J. Geophys. Res.: Atmos.* **2022**, *127* (10), No. e2021JD036215, DOI: 10.1029/2021JD036215.
(40) Campbell, J. R.; Battaglia, M., Jr.; Dingilian, K. K.; Cesler-Maloney, M.; Simpson, W. R.; Robinson, E. S.; DeCarlo, P. F.; Temime-Roussel, B.; D'Anna, B.; Holen, A. L.; Wu, J.; Pratt, K. A.; Dibb, J. E.; Nenes, A.; Weber, R. J.; Mao, J. Enhanced Aqueous Formation and Neutralization of Fine Atmospheric Particles Driven by Extreme Cold. *Sci. Adv.* **2024**, *10* (36), No. eado4373.
(41) Campbell, J. R.; Battaglia, M., Jr.; Dingilian, K.; Cesler-Maloney, M.; Simpson, W.; Robinson, E.; DeCarlo, P.; Temime-Roussel, B.; D'Anna, B.; Holen, A.; Wu, J.; Pratt, K.; Dibb, J.; Nenes, A.; Weber, R.; Mao, J. Enhanced Aqueous Formation and Neutralization of Fine Atmospheric Particles Driven by Extreme Cold. *Sci. Adv.* **2024**, *10*, No. eado4373.
(42) Brett, N.; Arnold, S. R.; Law, K. S.; Raut, J.-C.; Onishi, T.; Barret, B.; Dieudonné, E.; Cesler-Maloney, M.; Simpson, W.; Bekki, S.; Savarino, J.; Albertin, S.; Gilliam, R.; Fahey, K.; Pouliot, G.; Huff, D.; D'Anna, B. Estimating Power Plant Contributions to Surface

Pollution in a Wintertime Arctic Environment. *ACS ES&T Air* **2025**, *2* (5), 943−956.
(43) Li, M.; Wang, X.; Lu, C.; Li, R.; Zhang, J.; Dong, S.; Yang, L.; Xue, L.; Chen, J.; Wang, W. Nitrated Phenols and the Phenolic Precursors in the Atmosphere in Urban Jinan, China. *Sci. Total Environ.* **2020**, *714*, No. 136760.
(44) Rubio, M. A.; Bustamante, P.; Vásquez, Y. Atmospheric Phenolic Derivatives as Tracers in an Urban Area. *J. Chil. Chem. Soc.* **2019**, *64* (2), 4407−4411.
(45) Ahmed, S.; Thomas, J. L.; Tuite, K.; Stutz, J.; Flocke, F.; Orlando, J. J.; Hornbrook, R. S.; Apel, E. C.; Emmons, L. K.; Helmig, D.; Boylan, P.; Huey, L. G.; Hall, S. R.; Ullmann, K.; Cantrell, C. A.; Fried, A. The Role of Snow in Controlling Halogen Chemistry and Boundary Layer Oxidation During Arctic Spring: A 1D Modeling Case Study. *J. Geophys. Res.: Atmos.* **2022**, *127* (5), No. e2021JD036140, DOI: 10.1029/2021JD036140.
(46) Seinfeld, J. H.; Pandis, S. N. *Atmospheric Chemistry and Physics: From Air Pollution to Climate Change*, 3rd ed.; Wiley, 2016.
(47) Fuchs, N. A.; Sutugin, A. G.High-Dispersed Aerosols. In *Topics in Current Aerosol Research*; Elsevier, 1971; p 1 .
(48) Kaur, R.; Hudson, B. M.; Draper, J.; Tantillo, D. J.; Anastasio, C. Aqueous Reactions of Organic Triplet Excited States with Atmospheric Alkenes. *Atmos. Chem. Phys.* **2019**, *19* (7), 5021−5032.
(49) Corral Arroyo, P.; David, G.; Alpert, P. A.; Parmentier, E. A.; Ammann, M.; Signorell, R. Amplification of Light within Aerosol Particles Accelerates In-Particle Photochemistry. *Science.* **2022**, *376* (6590), 293−296.
(50) Atwi, K.; Cheng, Z.; El Hajj, O.; Perrie, C.; Saleh, R. A Dominant Contribution to Light Absorption by Methanol-Insoluble Brown Carbon Produced in the Combustion of Biomass Fuels Typically Consumed in Wildland Fires in the United States. *Environ. Sci.: Atmos.* **2022**, *2* (2), 182−191.
(51) Ma, L.; Worland, R.; Tran, T.; Anastasio, C. Evaluation of Probes to Measure Oxidizing Organic Triplet Excited States in Aerosol Liquid Water. *Environ. Sci. Technol.* **2023**, *57* (15), 6052−6062.
(52) Ossola, R.; Jönsson, O. M.; Moor, K.; McNeill, K. Singlet Oxygen Quantum Yields in Environmental Waters. *Chem. Rev.* **2021**, *121* (7), 4100−4146.
(53) Arakaki, T.; Anastasio, C.; Kuroki, Y.; Nakajima, H.; Okada, K.; Kotani, Y.; Handa, D.; Azechi, S.; Kimura, T.; Tsuhako, A.; Miyagi, Y. A General Scavenging Rate Constant for Reaction of Hydroxyl Radical with Organic Carbon in Atmospheric Waters. *Environ. Sci. Technol.* **2013**, *47* (15), 8196−8203.
(54) Hoffmann, D.; Tilgner, A.; Iinuma, Y.; Herrmann, H. Atmospheric Stability of Levoglucosan: A Detailed Laboratory and Modeling Study. *Environ. Sci. Technol.* **2010**, *44* (2), 694−699.
(55) Appiani, E.; Ossola, R.; Latch, D. E.; Erickson, P. R.; McNeill, K. Aqueous Singlet Oxygen Reaction Kinetics of Furfuryl Alcohol: Effect of Temperature, PH, and Salt Content. *Environ. Sci. Process. Impacts* **2017**, *19* (4), 507−516.
(56) McFall, A. S.; Johnson, A. W.; Anastasio, C. Air-Water Partitioning of Biomass-Burning Phenols and the Effects of Temperature and Salinity. *Environ. Sci. Technol.* **2020**, *54* (7), 3823−3830.
(57) Liu, H.; Liu, T.; Yu, C.; Xie, Y.; Wang, Q.; Zha, Q.; Chi, X.; Song, W.; Wang, X.; Lou, S.; Huang, X.; Ding, A. Kinetics and Mechanisms of Reactive Uptake of Methylglyoxal on Deliquesced Ammonium Salts: Acid Catalysis and Sulfate Inhibition. *Environ. Sci. Technol.* **2026**, *60* (7), 5619−5627.
(58) Arciva, S.; Ma, L.; Mavis, C.; Guzman, C.; Anastasio, C. Formation and Loss of Light Absorbance by Phenolic Aqueous SOA by $^{\bullet}$OH and an Organic Triplet Excited State. *Atmos. Chem. Phys.* **2024**, *24* (7), 4473−4485.
(59) Jiang, W.; Niedek, C.; Anastasio, C.; Zhang, Q. Photoaging of Phenolic Secondary Organic Aerosol in the Aqueous Phase: Evolution of Chemical and Optical Properties and Effects of Oxidants. *Atmos. Chem. Phys.* **2023**, *23* (12), 7103−7120.
(60) Yan, F.; Kang, S.; Sillanpää, M.; Hu, Z.; Gao, S.; Chen, P.; Gautam, S.; Reinikainen, S. P.; Li, C. A New Method for Extraction of Methanol-Soluble Brown Carbon: Implications for Investigation of Its Light Absorption Ability. *Environ. Pollut.* **2020**, *262*, No. 114300.
(61) Cao, T.; Li, M.; Zou, C.; Fan, X.; Song, J.; Jia, W.; Yu, C.; Yu, Z.; Peng, P. Chemical Composition, Optical Properties, and Oxidative Potential of Water-and Methanol-Soluble Organic Compounds Emitted from the Combustion of Biomass Materials and Coal. *Atmos. Chem. Phys.* **2021**, *21* (17), 13187−13205.
(62) Paraskevopoulou, D.; Kaskaoutis, D. G.; Grivas, G.; Bikkina, S.; Tsagkaraki, M.; Vrettou, I. M.; Tavernaraki, K.; Papoutsidaki, K.; Stavroulas, I.; Liakakou, E.; Bougiatioti, A.; Oikonomou, K.; Gerasopoulos, E.; Mihalopoulos, N. Brown Carbon Absorption and Radiative Effects under Intense Residential Wood Burning Conditions in Southeastern Europe: New Insights into the Abundance and Absorptivity of Methanol-Soluble Organic Aerosols. *Sci. Total Environ.* **2023**, *860*, No. 160434.
(63) Xu, Z.; Feng, W.; Wang, Y.; Ye, H.; Wang, Y.; Liao, H.; Xie, M. Potential Underestimation of Ambient Brown Carbon Absorption Based on the Methanol Extraction Method and Its Impacts on Source Analysis. *Atmos. Chem. Phys.* **2022**, *22* (20), 13739−13752.
(64) Clever, H. L.; Battino, R.; Miyamoto, H.; Yampolski, Y.; Young, C. L. IUPAC-NIST Solubility Data Series. 103. Oxygen and Ozone in Water, Aqueous Solutions, and Organic Liquids (Supplement to Solubility Data Series Volume 7). *J. Phys. Chem. Ref. Data* **2014**, *43* (3), No. 033102.
(65) Yu, L.; Smith, J.; Laskin, A.; Anastasio, C.; Laskin, J.; Zhang, Q. Chemical Characterization of SOA Formed from Aqueous-Phase Reactions of Phenols with the Triplet Excited State of Carbonyl and Hydroxyl Radical. *Atmos. Chem. Phys.* **2014**, *14* (24), 13801−13816.
(66) McNeill, K.; Canonica, S. Triplet State Dissolved Organic Matter in Aquatic Photochemistry: Reaction Mechanisms, Substrate Scope, and Photophysical Properties. *Environ. Sci. Process. Impacts* **2016**, *18* (11), 1381−1399.
(67) Paul, M. A. The Solubilities of Naphthalene and Biphenyl in Aqueous Solutions of Electrolytes. *J. Am. Chem. Soc.* **1952**, *74* (21), 5274−5277.
(68) Wang, C.; Lei, Y. D.; Endo, S.; Wania, F. Measuring and Modeling the Salting-out Effect in Ammonium Sulfate Solutions. *Environ. Sci. Technol.* **2014**, *48* (22), 13238−13245.
(69) May, W. E.; Wasik, S. P.; Freeman, D. H. Determination of the Solubility Behavior of Some Polycyclic Aromatic Hydrocarbons in Water. *Anal. Chem.* **1978**, *50* (7), 997−1000.
(70) De Carvalho, K. C. Investigation of Volatility, Composition, and Gas-Particle Phase Investigation of Volatility, Composition, and Gas-Particle Phase Partitioning of Atmospheric Organic Compounds through Novel Partitioning of Atmospheric Organic Compounds through Novel Instrumentation and Techniques Instrumentation and Techniques, Dissertation or Thesis; Washington University in St. LouisMS, 2024, .https://openscholarship.wustl.edu/eng_etds/1057.
(71) Ijaz, A.; Temime-Roussel, B.; Kammer, J.; Mao, J.; Simpson, W.; Law, K. S.; D'Anna, B. In Situ Measurements of Gas-Particle Partitioning of Organic Compounds in Fairbanks. *Faraday Discuss.* **2025**, *258* (23), 23−39.
(72) Kiland, K. J.; Mahrt, F.; Peng, L.; Nikkho, S.; Zaks, J.; Crescenzo, G. V.; Bertram, A. K. Viscosity, Glass Formation, and Mixing Times within Secondary Organic Aerosol from Biomass Burning Phenolics. *ACS Earth Space Chem.* **2023**, *7* (7), 1388−1400.
(73) Reid, J. P.; Bertram, A. K.; Topping, D. O.; Laskin, A.; Martin, S. T.; Petters, M. D.; Pope, F. D.; Rovelli, G. The Viscosity of Atmospherically Relevant Organic Particles. *Nat. Commun.* **2018**, *9*, No. 956, DOI: 10.1038/s41467-018-03027-z.
(74) Shiraiwa, M.; Pöschl, U. Mass Accommodation and Gas-Particle Partitioning in Secondary Organic Aerosols: Dependence on Diffusivity, Volatility, Particle-Phase Reactions, and Penetration Depth. *Atmos. Chem. Phys.* **2021**, *21* (3), 1565−1580.
(75) Worsnop, D. R.; Morris, J. W.; Shi, Q.; Davidovits, P.; Kolb, C. E. A Chemical Kinetic Model for Reactive Transformations of Aerosol Particles. *Geophys. Res. Lett.* **2002**, *29* (20), 57-1−57-4, DOI: 10.1029/2002GL015542.

(76) Simpson, W.; Cesler-Maloney, M.; Hoskins-Chaddon, R.Gas and Meteorological Measurements at the CTC Site and Birch Hill in Fairbanks, Alaska, during the ALPACA-2022 Field Study. Arctic Data Center [data set], 2023 DOI: 10.18739/A27D2Q87W.

https://doi.org/10.1021/acs.est.6c03997
Environ. Sci. Technol. 2026, 60, 22748−22758

Supplement to Rapid Wintertime Formation of Phenolic Secondary Organic Aerosol from Brown Carbon Photochemistry

Laura M. D. Heinlein•, Jonas Kuhn[†], Amna Ijaz[#††], Brice Temime-Roussel[#], Karolina Cysneiros de Carvalho[‡§], Mallory Liebes[¶], Fangzhou Guo[§§‡‡], James H. Flynn III[§§], Kyle Moor[¶], Brent Williams[‡||], Barbara D'Anna[#], Jochen Stutz[†], Cort Anastasio•**

TABLE OF CONTENTS

Section S1. Predicting emissions of semi-volatile phenols

First, we calculated the emissions ratio of each phenol (ArOH) to levoglucosan. Schauer et al.[1] report phenol and levoglucosan emissions from hardwood and softwood in units of mg per kg wood burned. We calculate the emissions ratio (ER) for each phenol relative to levoglucosan with

$$\mathrm{ER} = \frac{e_{\mathrm{ArOH}}}{e_{\mathrm{LG}}} \quad \text{(S1)}$$

where ER is the emissions ratio either for hardwood or softwood specifically (mg-ArOH mg-levoglucosan^{-1}), e_{ArOH} is the emissions of a given phenol reported by Schauer (mg-ArOH kg-wood burned^{-1}) for that wood type, and e_{LG} is the emissions of levoglucosan for that wood type (mg-levoglucosan per kg^{-1}-wood burned).

Next, we next created an emission profile for levoglucosan by scaling emissions of methane from wood burning reported in the EPA's emission inventory so that the PACT-1D modeled levoglucosan concentrations matched the measured values. We designate a fraction of the levoglucosan as hardwood and softwood using data from Ijaz et al. (2025), who used positive matrix factorization of CHARON-PTR-ToF-MS data from ALPACA to identify a hardwood and softwood factor in organic aerosol (Figure S3).[2] We assume that the sum of the hardwood and softwood organic aerosol identified by positive matrix factorization is equal to the total biomass burning organic aerosol concentration, and therefore designate the fraction (F) of levoglucosan as originating from hardwood (HW) and softwood (SW) burning based on

$$\mathrm{F} = \frac{\mathrm{OA_{HW\ or\ SW}}}{\mathrm{OA_{HW}+OA_{SW}}} \quad \text{(S2)}$$

where $\mathrm{OA_{HW}}$ and $\mathrm{OA_{SW}}$ are the OA concentrations identified as originating from HW or SW determined by positive matrix factorization, as depicted in Figure S4. Next, we combine the emissions profiles of hardwood and softwood levoglucosan and the emissions ratios of phenols to calculate the emissions profile of 34 phenols from hardwood and softwood smoke with:

$$\mathrm{E_{ArOH,p}} = \mathrm{E_{LG}} \times \left(\mathrm{F_{HW}} \times \mathrm{ER_{HW}} \times \frac{\mathrm{MW_{ArOH}}}{\mathrm{MW_{LG}}} \times \mathrm{X_{p,HW}} + \mathrm{F_{SW}} \times \mathrm{ER_{SW}} \times \frac{\mathrm{MW_{ArOH}}}{\mathrm{MW_{LG}}} \times \mathrm{X_{p,SW}}\right) \quad \text{(S3)}$$

where: $E_{arOH,p}$ is the emissions profile of a given phenol (ArOH) in phase p (either gas phase or organic particle, mlc cm-air^{-3} s^{-1}); E_{LG} is the total emissions rate of levoglucosan (mlc cm-air^{-3} s^{-1}); $ER_{ArOH,HW}$ and $ER_{ArOH,SW}$ are the emissions ratios of each ArOH from HW and SW (mg-ArOH mg^{-1}-levoglucsoan), respectively;[1] MW_{ArOH} and MW_{LG} are the molecular weights of a phenol and levoglucosan, respectively; and $X_{p,SW}$ and $X_{p,HW}$ are the reported fraction of the phenol emitted in phase p (either gas phase or organic phase, Table S2). We assume the 34 phenols reported by Schuaer et al.[ref] and included here account for the majority of phenols relevant to phenolic SOA formation.

Section S2. Mass transfer: uptake and evaporation rates

The rate constant for uptake of a phenol into a particle is calculated using the mass transfer continuum regime framework:[3]

$$k_{\mathrm{C,in}} = 4\pi \mathrm{R_p} \mathrm{D_g} \mathrm{N_p} \quad \text{(S4)}$$

where $k_{\mathrm{C,in}}$ is the rate constant for uptake in the continuum regime (s^{-1}), R_p is the particle radius (m), D_g is the gas diffusion coefficient for each species ($m^2\ s^{-1}$), and N_p is the particle number (m^{-3}). The Fuchs-Sutugin approach[4] is used to correct for the transition regime with

$$k_{\mathrm{T,in}} = k_{\mathrm{C,in}} \frac{0.75\ \alpha\ (1+\mathrm{Kn})}{\mathrm{Kn}^2+\mathrm{Kn}+0.283\ \mathrm{Kn}\ \alpha+0.75\ \alpha} \quad \text{(S5)}$$

where $k_{\mathrm{T,in}}$ is the rate constant for uptake in the transition regime (s^{-1}), α is the mass accommodation coefficient (Section S3 and Table S3), and Kn is the Knudsen number (unitless).[4] Uptake rates are calculated with

$$R_{\mathrm{in}} = k_{\mathrm{T,in}}[i]_{\mathrm{g}} \quad \text{(S6)}$$

where R_{in} is the rate of uptake (mlc $cm^{-3}\ s^{-1}$) and $[i]_g$ is the gas-phase concentration of the species *i* (mlc cm^{-3}). Equations for D_g and Kn can be found in past PACT-1D publications.[5–8]

As described in past work,[5–8] we combine the uptake rate constant and the equilibrium constants from Henry's Law and Pankow's partitioning scheme to calculate the evaporation rate constant using

$$K_{\mathrm{eq}}^{\mathrm{cc}} \times \mathrm{V} = \frac{[i]_{\mathrm{p}}}{[i]_{\mathrm{g}}} = \frac{k_{\mathrm{T,in}}}{k_{\mathrm{out}}} \quad \text{(S7)}$$

where K_{eq}^{cc} is the equilibrium partitioning constant (m^3-particle m^{-3}-air, where cc denotes the equilibrium constant is in units of concentration per concentration: the units are equivalent to $\frac{mol/m^3-particle}{mol/m^3-air}$), V is the ALWC ($m^3$-aq m^{-3}-air) for aqueous particles and the volume of OA (m^3-OA m^{-3}-air) for organic particles, $[i]_p$ is the concentration of *i* in phase p (mlc cm^{-3}-air), $[i]_g$ is the concentration of *i* in the gas phase (mlc cm^{-3}-air), k_{in} is the rate constant for uptake (s^{-1}), and k_{out} is the evaporation rate constant (s^{-1}). Equation S7 can be rearranged to solve for k_{out} with

$$k_{\mathrm{out}} = \frac{k_{\mathrm{T,in}}}{K_{\mathrm{eq}}^{\mathrm{cc}} \times \mathrm{V}} \quad \text{(S8)}$$

For the aqueous phase, K_{eq}^{cc} is the Henry's Law constant corrected for temperature and ionic strength (Section S4) and transformed to its dimensionless form (Section S5).[9] For the organic phase, K_{eq}^{cc} is the K_{pi} partitioning constant converted to its dimensionless form (Section S5). The evaporation rate (R_{out}, mlc $cm^{-3}\ s^{-1}$) is then calculated with

$$R_{\mathrm{out}} = k_{\mathrm{out}}[i]_{\mathrm{p}} \quad \text{(S9)}$$

Section S3. Temperature correction to accommodation coefficients

Accommodation coefficients with respect to water have been reported for a small number of phenols and range between 3.7×10^{-5} and 0.022.[10,11] These values were derived from experiments performed with wetted flow tube reactors for phenol, 3-methylphenol, 2,5-dimethylphenol, and 2,6-dimethylphenol, which were then applied to all 34 phenols included in our simulations. PACT-1D calculates temperature-dependent accommodation coefficients with the equations listed in Table S3. For organic particles, measurements of accommodation coefficients of semi-volatile organic compounds are generally between 0.1 and 1.[12–14] However, we know of no measurements of accommodation coefficients of substituted phenols to organic particles. In PACT-1D, we assume these values are equivalent to those measured in water. Once corrected for the low temperatures in Fairbanks during ALPACA, the resultant accommodation coefficients are predominantly between 0.1 and 1, within the range of available measurements.[12–14] Because accommodation coefficients for organic particles in PACT-1D are calculated with respect to water, they are likely a lower bound, as the solvation barrier of phenols is likely lower for less-polar organic aerosol than it is for polar aqueous droplets.

Section S4. Gas-aqueous partitioning: temperature and ionic strength correction for Henry's Law

I. Temperature correction

Henry's Law constants are corrected for temperature using the Van't Hoff equation

$$K_{\mathrm{H,T_2}} = K_{\mathrm{H,T_1}} \exp\left(-\frac{\Delta H_{\mathrm{sol}}}{\mathrm{R}}\left(\frac{1}{\mathrm{T_2}} - \frac{1}{\mathrm{T_1}}\right)\right) \quad \text{(S10)}$$

where $K_{\mathrm{H,T2}}$ is the temperature-corrected Henry's Law constant (mol L^{-1} atm^{-1}), $K_{\mathrm{H,T1}}$ is the value at standard temperature (mol L^{-1} atm^{-1}), ΔH_{sol} is the enthalpy of dissolution (J mol^{-1}), R is the gas constant (8.314 J mol^{-1} K^{-1}), T_2 is the target temperature (K), and T_1 is the standard temperature (K). The Henry's law constants and $-\frac{\Delta H_{sol}}{R}$ values are listed in Table S4.

II. Ionic strength correction

The Henry's law constant is corrected for ionic strength using the Setschenow equation

$$-K_{\mathrm{s,salt}}[\mathrm{salt}] = \log(\gamma_{\mathrm{salt}}) = \log\left(\frac{K_{\mathrm{H,H2O}}}{K_{\mathrm{H,salt}}}\right) \quad \text{(S11)}$$

where $K_{\mathrm{s,salt}}$ is the Setschenow coefficient for a given compound and salt (L-aq mol^{-1}, Table S5), [salt] is the concentration of a salt (mol L^{-1}-aq), γ_{salt} is the activity coefficient of the phenol (dimensionless), $K_{\mathrm{H,H2O}}$ is the Henry's Law constant in pure water (mol L^{-1} atm^{-1}), and $K_{\mathrm{H,salt}}$ is the Henry's Law constant corrected for ionic strength (mol L^{-1} atm^{-1}). Equation S11 can be rearranged as

$$K_{\mathrm{H,salt}} = K_{\mathrm{H,H2O}} \times 10^{-K_{\mathrm{s,salt}}[\mathrm{salt}]} \quad \text{(S12)}$$

Sulfate is the dominant inorganic species during ALPACA. McFall et al. (2020) measured K_s values for eight semi-volatile phenols with five salts: ammonium sulfate, ammonium nitrate, potassium nitrate, sodium chloride, and ammonium chloride.[15] As sulfate is the dominant salt in winter Fairbanks particles, we only account for ammonium sulfate in our activity coefficient calculation. Ionic strength due to sulfate is calculated using measured sulfate concentrations and aerosol liquid water content.[16,17] There are two dominant sulfate sources in two distinct particle modes: primary sulfate forming small ~100 nm particles and secondary sulfate on larger 300-500 nm biomass-burning particles..[18,19] In our calculation of sulfate molarity, we only include the sulfate expected to be on the larger particles which are sites of secondary chemistry.[19] To do this, we apply the campaign average of 62% of sulfate originating from primary sources[16,20] only including the 38% considered secondary sulfate in our calculations of sulfate molarity on secondary particles.[17,21] Once K_H is corrected for temperature and ionic strength, it is converted to its dimensionless form ($K^{CC}_{\mathrm{H,T2,salt}}$, m^3-air m^{-3}-aq) with

$$K^{\mathrm{CC}}_{\mathrm{H,T2,salt}} = K_{\mathrm{H,T2,salt}} \times \mathrm{R} \times \mathrm{T} \quad \text{(S13)}$$

Section S5. Gas-organic partitioning: Pankow's adsorption calculation and temperature correction

Gas-organic partitioning is simulated with Pankow's Adsorption model, which calculates the saturation concentration (C_i*) of each species using its temperature-corrected saturation vapor pressure ($p_{sat,T2}$). $p_{sat,T2}$ is calculated with the Clausius-Claperyon equation

$$p_{sat,T_2} = p_{sat,T_1} \times \exp\left(-\frac{\Delta H_{vap}}{R}\left(\frac{1}{T_2} - \frac{1}{T_1}\right)\right) \quad \text{(S14)}$$

where $p_{sat,T1}$ is the saturation vapor pressure of species *i* at standard temperature (atm), ΔH_{vap} is the enthalpy of vaporization of species *i* (L atm^{-1} mol^{-1}). The gas-organic partitioning constant ($K_{p,i}$, m^3 μg^{-1}) is then calculated with

$$K_{p,i} = \frac{R \times T_2}{MW_{avg} \times p_{sat,T2} \times 10^6} \quad \text{(S15)}$$

where R is the gas constant (8.2057 × 10^{-5} m^3 atm mol^{-1} K^{-1}), MW_{avg} is the average molecular weight of species in OA (250 g mol^{-1})[22–24] and 10^6 is a unit conversion from g to μg. Finally, $K_{p,i}$ is converted to its dimensionless form. $K_{p,i}$ is defined as

$$K_{p,i} = \frac{C_i^{aer}}{C_i^{gas} C_{OA}} \quad \text{(S16)}$$

where C_i^{aer} is the saturation concentration of species *i* in the particle (μg-*i* m^{-3}-air), C_i^{gas} is the gas-phase saturation concentration of *i* (μg-*i* m^{-3}-air), and C_{OA} is the concentration of organic aerosol (μg-OA m^{-3}-air).[25,26] The dimensionless Pankow partitioning constant ($K_{p,i}^{cc}$, $\frac{\mu g - i - gas / m^3 - air}{\mu g - i - p / m^3 - OA}$) can be calculated with

$$K_{p,i}^{cc} = K_{p,i} \times 10^{12} \times \rho_{OA} \quad \text{(S17)}$$

where 10^{12} converts units from μg-OA to m^3-OA and ρ_{OA} is the density of OA (g cm^{-3}). The time-resolved OA density is calculated as described by Kuwata at al. (2012)[27] using the O:C and H:C measured by Ijaz et al. (2025)[21] with

$$\rho_{OA} = 1000 \frac{12 + 1(H{:}C) + 16(O{:}C)}{7.0 + 5(H{:}C) + 4.15(O{:}C)} \quad \text{(S18)}$$

Section S6. Predicting DOC concentrations

To estimate the total methanol-soluble organic carbon concentrations in Fairbanks particles, we use the total organic aerosol concentrations measured during ALPACA (Figure S1)[21] and assume that methanol extracts 90% of the total organic carbon mass, as reported by Atwi et al.[28] As an approximation, we assume that this reported 90% of methanol-extractable carbonaceous mass includes both the methanol-extractable and water-extractable fractions. The concentration of dissolved organic carbon in a given phase *i* (aqueous or organic), $[DOC]_i$ (mol-C L^{-1}), is then determined with

$$[DOC]_i = \frac{[OA]}{2 \times 10^9 \times V_p \times 12.011} \times 0.9 \times Z_i \quad \text{(S19)}$$

where [OA] is the total concentration of organic aerosol modeled by PACT-1D (μg m^{-3}), the factor of 2 converts OA mass to organic carbon mass assuming an OM/OC ratio of 2, 10^9 is the combined unit conversion from μg to g and from m^{-3} to L^{-1}, V_p is the volume of the phase of interest (either ALW or OA, m^3-phase m^{-3}-air), and 12.011 g mol^{-1} is the molecular weight of carbon. The 0.9 factor is the fraction of organic carbon that is soluble in methanol.[28] We adopt this number because we assume only water-extractable or methanol-extractable BrC can produce photooxidants. Finally, Z_i is the fraction of particulate organic carbon that is extracted into water (40%) or methanol (60%), which is also from Atwi et al. (2022).[28]

Section S7. Measurement of $k_{1O2*+DOC}$ in D_2O

Previous work has estimated the rate constant for interactions of $^1O_2$* with DOC using measurements in ambient aged woodsmoke extracts.[29–31] Here, we prepare fresh, lab-generated woodsmoke extracts and use them to measure $k_{1O2*+DOC}$.

To determine the rate constant of $^1O_2$* by dissolved organic carbon (DOC) in fresh woodsmoke, we measured the quenching of time-resolved $^1O_2$* phosphorescence signals as a function of woodsmoke extract addition. Woodsmoke extracts were prepared by burning birch firewood from Fairbanks, Alaska in a 40 L smoldering combustion chamber, collecting smoke on filters, and extracting them into D_2O by sonication for 2 h. The extracts were first vacuum filtered through a glass microfiber filter and then syringe filtered with a 0.45 um PVDF filter. In the stock woodsmoke extract, the DOC concentration was 1.58(±0.03) mol-C L^{-1} and the ratio of DOC to the measured absorbance at 365 nm was 14 mol-C L^{-1} cm^{-1}. DOC was measured with Shimadzu Total Organic Carbon Analyzer (TOC-V CSH) and the UV-Vis absorbance spectrum was measured in 1 cm quartz cuvettes (Starna Cells) with a Shimadzu UV-2501PC spectrophotometer.

Time-resolved $^1O_2$* phosphorescence measurements were collected using a spectrometer (LP-980, Edinburgh Instruments, UK) equipped with a near-infrared photomultiplier tube detector (H10330C-45-C2, Hamamatsu, Japan). $^1O_2$* phosphorescence was detected at 1275 nm with a 5 nm monochromator bandwidth. Excitation light at 530 nm was provided by a wavelength-tunable laser (Radiant QX8130, OPOTEK, U.S.A) that operated at a repetition rate of 10 Hz with 6 ns pulse widths. Rose Bengal (95%, Sigma Aldrich) and D_2O (99.9%, Sigma Aldrich) were used as purchased.

To measure the quenching of $^1O_2$* by DOC in the woodsmoke extract, $^1O_2$* signals were generated from 12.5 μM Rose Bengal solutions in D_2O containing different volumes of woodsmoke extract. The $^1O_2$* kinetic traces generated from these solutions were fit using a mono-exponential decay equation to yield $^1O_2$* decay rate constants (k'), which were used to calculate the quenching rate constant of $^1O_2$* with woodsmoke extract (k_q) using equation S19:[32]

$$k' = k_d + k_{1O2*+DOC}[\mathrm{DOC}] \quad \text{(S20)}$$

where k_d is the measured deactivation rate constant for $^1O_2$* in D_2O without any woodsmoke extract, $k_{1O2*+DOC}$ is the total (physical quenching and chemical reaction) rate constant for woodsmoke DOC with $^1O_2$*, and DOC is the concentration of woodsmoke DOC in the illuminated solution. $^1O_2$* kinetic traces are provided in Figure S15a.

Without any woodsmoke extract, we observed a $^1O_2$* lifetime of 68 μs, on the higher side of previously reported values of 44-70 μs for $^1O_2$* in D_2O.[33] With increasing concentrations of woodsmoke extract, k' increased (i.e., $^1O_2$* lifetimes decreased), indicating quenching/reaction of $^1O_2$* by woodsmoke extracts (Figure S15). Using this plot (Figure S15b) and equation S19, we calculate a quenching rate constant of 1.6(±0.1)×10^6 L mol-C^{-1} s^{-1}. This value is approximately 16 times higher than the upper bound estimated for summertime woodsmoke particles collected from Northern California, suggesting that $^1O_2$*-reactive organics in BBOA are lost during

atmospheric transport. However, the difference could also be due to differences in BBOA composition. For example, $^1O_2$* quenching rate constants for aquatic dissolved organic matter isolates[34] range from 1.5×10^5 L mol-C^{-1} s^{-1} for Suwannee River fulvic acid to 1.3×10^6 M-C^{-1} s^{-1} for Pony Lake fulvic acid.

Section S8. Calculating direct photodegradation rate constants for phenolic carbonyls

Ten of the phenols included in PACT-1D have a carbonyl group on the aromatic ring and thus undergo direct photodegradation. We calculated the time-dependent rate constant for this process for each of the ten phenols using in aqueous and organic particles with.

$$j_{\mathrm{ArOH,PM}} = \sum I'_{\lambda}\, \varepsilon_{\mathrm{ArOH},\lambda}\, \Phi_{\mathrm{ArOH,PM}}\, \frac{2.303 \times 10^{3}}{N_{\mathrm{A}}} \times 2.5 \qquad \text{(S21)}$$

where $j_{\mathrm{ArOH,PM}}$ is the rate constant for direct photodegradation of a given phenol in aqueous and organic particles (s^{-1}), I'_{λ} is the photon flux[35] at wavelength λ (photon cm^{-2} nm^{-1} s^{-1}), $\varepsilon_{\mathrm{ArOH},\lambda}$ is the base-10 molar absorption coefficient of a given ArOH at wavelength λ (M^{-1} cm^{-1}), $\Phi_{\mathrm{ArOH,PM}}$ is the quantum yield for direct photodegradation of a given phenol,[36] 2.303 is the log transformation, 10^3 is the unit conversion from L^{-1} to cm^{-3}, N_{A} is Avogadro's number, and 2.5 is a unitless factor which accounts for optical confinement inside particles.[37] Table S9 shows $j_{\mathrm{ArOH,PM}}$ values in the condensed phases, at solar noon on 1/30/22 in Fairbanks, Alaska. In the gas phase, we use a similar equation

$$j_{\mathrm{ArOH,gas}} = \sum I'_{\lambda}\, \varepsilon_{\mathrm{ArOH},\lambda}\, \Phi_{\mathrm{ArOH,gas}}\, \frac{2.303 \times 10^{3}}{N_{\mathrm{A}}} \qquad \text{(S22)}$$

where $\Phi_{\mathrm{ArOH,gas}}$ is the gas-phase photodegradation quantum yield calculated as described in Smith et al. (2016) by multiplying the measured particle-phase *j*-values by 7, based on the estimated ratio of $\Phi_{\mathrm{ArOH,gas}}$:$\Phi_{\mathrm{ArOH,aqueous}}$ for phenol photolysis.[36] Gas-phase photodegradation rate constants are in Table S7.

Section S9. Temperature correction of reaction rate constants

Temperature-corrected reaction rate constants (k_{T2}, cm^3-air mlc^{-1} s^{-1} or L mol^{-1} s^{-1}) are calculated with the Arrhenius equation

$$k_{T2} = k_{T1} \times \exp\left(-\frac{E_a}{R}\left(\frac{1}{T_2} - \frac{1}{T_1}\right)\right) \quad \text{(S23)}$$

where k_{T1} is the rate constant at temperature T_1 (cm^3-air mlc^{-1} s^{-1} or L mol^{-1} s^{-1}) and E_a is the activation energy (kJ mol^{-1}). E_a values are listed in Tables S12 and S13.

Section S10. Uncertainties in PACT-1D simulations relating to (a) photochemistry of organic-soluble brown carbon, (b) activity coefficients in aqueous and organic particles, and (c) viscosity.

(a) Photochemistry of organic-soluble brown carbon

Measurements of photooxidant production from organic-soluble BrC are scarce.[38,39] To our knowledge, this is the first kinetic model of photooxidant production which accounts for brown carbon chromophores that are not water soluble but are soluble in polar organic solvents (i.e. methanol).[35,38,39] We assume the photochemical properties of water-soluble BrC[29,35] apply to organic-soluble BrC, yet this likely results in a lower bound of $^3C^*$ reactivity.[39] Specifically, we suspect our modeling is a lower bound for photooxidant generation in organic particles because Sardena et al.[39] found brown carbon extracted into acetonitrile has up to 4-times higher $^3C^*$ concentrations and 5-times higher $^1O_2^*$ quantum yields than their aqueous counterparts.

Other components required in the kinetic model for photooxidant production and reactions in organic particles are also poorly understood. Mass absorption coefficients of organic-soluble chromophores are not known. The impact of the organic-rich solvation environment of organic aerosols on the light absorbing properties of brown carbon are unknown. Organic solvents can cause blueshifts in the molar absorption coefficients of individual chromophores, yet it is unclear if a hypsochromic or bathochromic shift happens for chromophores in organic aerosols.[39] Furthermore, we assume the properties of oxidizing $^3C^*$ – including oxidation potential and excited state energies – in aqueous and organic particles are the same, which allows us to assume $^3C^*$ have equivalent reactivity in both particle types.[40] For example, we assume the $^3C^*$ and $^1O_2^*$ rate constants for quenching by DOC – the dominant sink for both oxidants – are equivalent in both solvents, yet the values are not known in organic aerosols.[29] Lastly, without measurements of dissolved O_2 concentrations in organic aerosol, we assume it is equivalent to the O_2 solubility in methanol ($K_{H,methanol} = 2.41\times10^{-2}$ M atm^{-1}, calculated from O_2 solubility in methanol compared to water,[41] temperature corrected with aqueous ΔH_{sol}).

(b) Activity coefficients in aqueous and organic particles

Activity coefficients are poorly understood in ALW and OA. In both particle types, we assume photooxidant activity coefficients of unity, as values are poorly understood. In aqueous particles, we calculate the ionic strength from sulfate measurements assuming internally mixed particles, which likely overestimates the impact of ammonium sulfate on aqueous chemistry. This can be seen in single particle measurements during the ALPACA field campaign, which show that 42% of sulfate particles did not show evidence of secondary processing (i.e. did not contain hydroxymethanesulfonate),[19] indicating a large fraction of the primary sulfate particles were not involved in the multiphase chemistry targeted by this study. As the majority of sulfate was primary sulfate, this suggests our assumption of internal mixing overestimates the aqueous sulfate concentrations and overestimates the suppression of aqueous phenolic SOA formation by high ionic strength.

(c) Viscosity

At cold temperatures, particle viscosity has the capacity to slow gas-particle partitioning.[42–45] There is abundant evidence for multiphase chemistry during winter pollution events in Fairbanks, including the formation of secondary sulfate,[20] hydroxymethanesulfonate,[19,46,47] and oxidized organic aerosol/aged biomass burning particles,[19,21,48] all of which confirm that viscosity-driven uptake limitations do not prevent secondary multiphase chemistry. Nonetheless, an increase in the viscosity of particles is possible, which may have varied impacts on multiphase chemistry. For example, enhanced viscosity can slow gas-particle partitioning, generate concentration gradients of phenols within particles, and lead to heterogenous photooxidant generation (i.e. if the uptake of O_2 is viscosity-limited, this might suppress O_2 as a $^3C^*$ sink and concurrently suppress $^1O_2^*$ production), though the magnitude of these potential impacts is highly uncertain. The aim of this work is to explore the potential role of multiphase brown carbon photochemistry in urban winter pollution events, and therefore the intricate, varied, and uncertain impacts of particle viscosity of multiphase are beyond the scope of this work but should be explored in future work to understand its impact on multiphase chemistry in Fairbanks.

Table S1. Names, molecular weights, and structures of the 34 biomass-burning phenols included in our modeling.

Compound	Formula	Molecular Weight (g/mol)	Structure
Phenols			
phenol	C_6H_6O	94.11	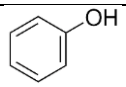
o-cresol	C_7H_8O	108.14	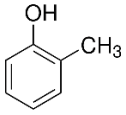
m- and p-cresol	C_7H_8O	108.14	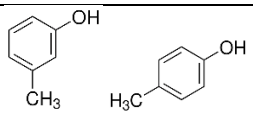
dimethylphenols [a]	$C_8H_{10}O$	122.16	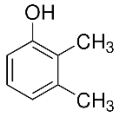
Diols			
catechol	$C_6H_6O_2$	110.11	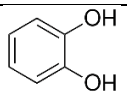
resorcinol	$C_6H_6O_2$	110.11	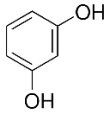
hydroquinone	$C_6H_6O_2$	110.11	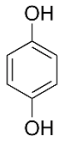
tyrosol	$C_8H_{10}O_2$	138.16	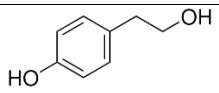
methylcatechols [b]	$C_7H_8O_2$	124.14	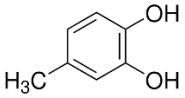
hydroxybenzaldehydes [c]	$C_7H_6O_2$	122.12	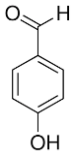
Guaiacols			
guaiacol	$C_7H_8O_2$	124.14	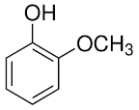

4-vinylguaicol	$C_9H_{10}O_2$	150.18	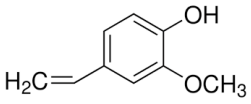
4-methylguaicol	$C_8H_{10}O_2$	138.16	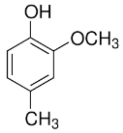
4-ethylguaicol	$C_9H_{12}O_2$	152.19	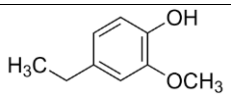
4-propylguaicol	$C_{10}H_{14}O_2$	166.22	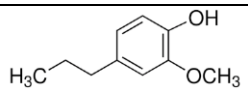
eugenol	$C_{10}H_{12}O_2$	164.2	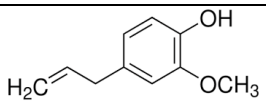
cis- & trans-isoeugenol	$C_{10}H_{12}O_2$	164.2	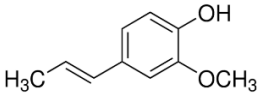
homovanillic acid	$C_9H_{10}O_4$	182.17	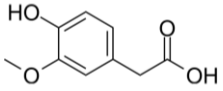
guaicyl acetone	$C_{10}H_{12}O_2$	180.2	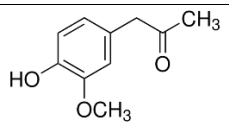
Syringols			
syringol	$C_8H_{10}O_3$	154.16	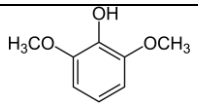
4-methylsyringol	$C_9H_{12}O_3$	168.19	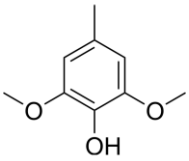
4-ethylsyringol	$C_{10}H_{14}O_3$	182.22	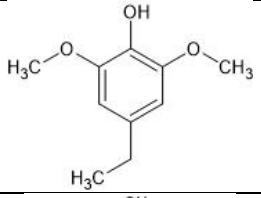
4-propylsyringol	$C_{11}H_{16}O_3$	196.25	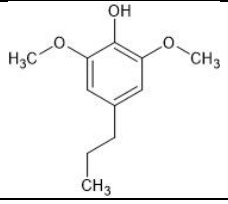

4-allylsyringol	$C_{11}H_{14}O_3$	194.23	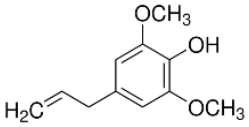
4-propenylsyringol	$C_{11}H_{14}O_3$	194.23	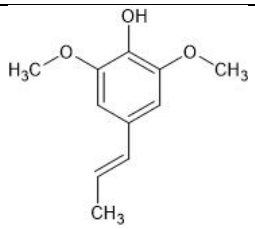
propionyl syringol	$C_{11}H_{14}O_4$	210.25	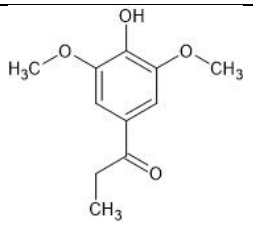
syringyl acetone	$C_{11}H_{14}O_4$	210.25	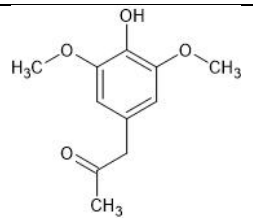
butyrylsyringol	$C_{12}H_{16}O_4$	224.26	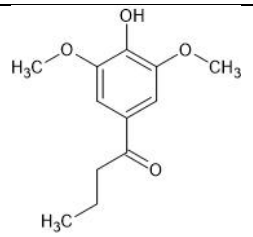
Carbonyls			
vanillin	$C_8H_8O_3$	152.15	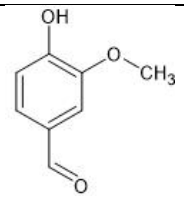
acetovanillone	$C_9H_{10}O_3$	166.17	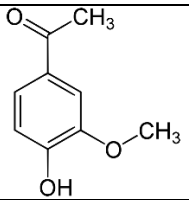
coniferylaldehyde	$C_{10}H_{10}O_3$	178.18	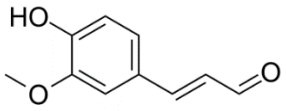

syringaldehyde	$C_9H_{12}O_4$	182.17	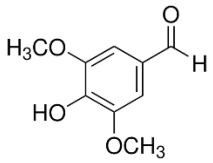
acetosyringone	$C_{10}H_{12}O_4$	196.19	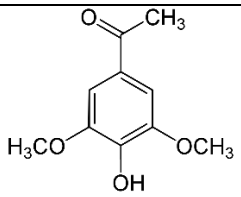
sinapylaldehyde	$C_{11}H_{12}O_4$	208.21	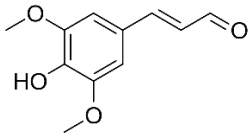

[a] Includes all structural isomers of dimethylphenols with the methyl groups in the 2, 3, and 4 positions.
[b] Includes 3- and 4-methylcatechol.
[c] Includes 2-, 3-, and 4-hydroxybenzaldehyde.

Table S2. Emissions ratios of phenols to Levoglucosan from softwood and hardwood[11]

Compound [e]	Emissions Ratios (ER) [a]		Phase-specific Fraction (X_p) [a]			
	Hardwood (HW)	Softwood (SW)	$X_{g,HW}$	$X_{org,HW}$	$X_{g,SW}$	$X_{org,SW}$
Phenols						
phenol	0.425	0.382	1.00	0	1.00	0
o-cresol	0.07	0.0652	1.00	0	1.00	0
m- and p-cresol	0.254	0.277	1.00	0	1.00	0
dimethylphenol	0.0718	0.0803	1.00	0	1.00	0
Diols						
catechol	0.201	0.227	1.00	0	1.00	0
resorcinol	0.0432	0.0362	0.06	0.94	0.15	0.85
hydroquinone	0.0385	0.0277	0.45	0.55	0.52	0.48
tyrosol	0.288	0	0	0	0.05	0.95
methylcatechols	0.120	0.0472	0.16	0.84	0.66	0.34
hydroxybenzaldehydes	0.0207	0.0146	0.60	0.40	0.96	0.04
Guaiacols						
guaicol	0.244	0.203	1.00	0	1.00	0
4-vinylguaicol [b]	0.142	0.148	1.00	0	1.00	0
4-methylguaicol	0.143	0.247	1.00	0	1.00	0
4-ethylguaicol	0.142	0.148	1.00	0	1.00	0
4-propylguaicol	0.0448	0.0510	0.99	0.01	1.00	0
eugenol	0.0293	0.0419	0.99	0.01	1.00	0
cis- & trans-isoeugenol [c]	0.0524	0.121	0.96	0.04	1.00	0
homovanillic acid [d]	0.0752	0.177	0.43	0.57	0.95	0.05
guaicyl acetone	0.222	0.150	0.43	0.57	0.78	0.22
Syringols						
syringol	0.565	0	0	0	1.00	0
4-methylsyringol	9.63×10^{-3}	2.19×10^{-4}	1.00	0	0.97	0.03
4-ethylsyringol	0.277	1.64×10^{-4}	1.00	0	0.94	0.06
4-propylsyringol	0.115	0	0	0	0.81	0.19
4-allylsyringol	8.88×10^{-3}	0	0	0	0.21	0.79
4-propenylsyringol	0.0531	0	0	0	0.03	0.97
propionyl syringol	0.0432	0.0362	0	0	0	1.00
syringyl acetone	0.0385	0.0277	1.00	0	0.03	0.97
butyrylsyringol	5.00×10^{-4}	0	0	0	0	1.00
Carbonyls						
vanillin	0.0752	0.177	0.43	0.57	0.95	0.05
acetovanillone	0.0344	0.0369	0.61	0.39	0.95	0.05
coniferylaldehyde	0.0214	0.167	0	1.00	0	1.00

syringaldehyde	0.0468	0	0.00	0	0.23	0.77
acetosyringone	0.0412	0	0.00	0.00	0.04	0.96
sinapylaldehyde	0.0261	0	0	0	0	1.00

[a] The Emissions Ratio (ER) is the ratio of ArOH emissions to levoglucosan emissions for a given phenol (equation S1), with emissions values from Schauer et al.[1] in units of mg per kg wood burned. We used pine as the surrogate for softwood and oak as the surrogate for hardwood.
[b] Assumed equal to 4-ethylguaiacol emissions ratios from hardwood and softwood.
[c] Emissions ratio is equal to the sum reported for cis- and trans-isoeugenol.
[d] Assumed equal to vanillic acid.
[e] All values are for the neutral form of the compound, unless otherwise noted.

Table S3. Mass accommodation coefficients at 298 K, associated temperature adjustments, and mass accommodation coefficients calculated at 248 K.

Compound [f]	α (298 K)	T Adjustment	α (248 K)
Phenols			
phenol [10]	0.0022	$\alpha_T = \frac{1}{e^{\left(\left(-\frac{7440}{T}\right)+30.1\right)}+1}$ (S24)	0.48
o-cresol [a]	0.0018	$\alpha_T = \frac{1}{e^{\left(\left(-\frac{2830}{T}\right)+14.8\right)}+1}$ (S25)	0.033
m- and p-cresol [b,10]			
dimethylphenol [c,11]	3.7×10^{-5}	$\alpha_T = 7.000 \times 10^{16} \times e^{-0.1643\,T}$ (S26)	0.14
Diols			
catechol [d]	3.7×10^{-5}	$\alpha_T = 7.000 \times 10^{16} \times e^{-0.1643\,T}$ (S26)	0.14
resorcinol [d]			
hydroquinone [d]			
tyrosol [d]			
methylcatechols [d]			
hydroxybenzaldehydes [d]			
Guaicols			
guaicol [d]	3.7×10^{-5}	$\alpha_T = 7.000 \times 10^{16} \times e^{-0.1643\,T}$ (S26)	0.14
4-vinylguaicol [d]			
4-methylguaicol [d]			
4-ethylguaicol [d]			
4-propylguaicol [d]			
eugenol [d]			
cis- & trans-isoeugenol [d]			
homovanillic acid [d]			
guaicyl acetone [d]			
Syringols			
syringol [d]	3.7×10^{-5}	$\alpha_T = 7.000 \times 10^{16} \times e^{-0.1643\,T}$ (S26)	0.14
4-methylsyringol [d]			
4-ethylsyringol [d]			
4-propylsyringol [d]			
4-allylsyringol [d]			
cis-syringyprop-1-ene [d]			
propionyl syringol [d]			
syringyl acetone [d]			
butyrylsyringol [d]			
Carbonyls			
vanillin [d]	3.7×10^{-5}	$\alpha_T = 7.000 \times 10^{16} \times e^{-0.1643\,T}$ (S26)	0.14
acetovanillone [d]			

coniferylaldehyde [d]			
syringaldehyde [d]			
acetosyringone [d]			
sinapylaldehyde [d]			
Inorganic Species			
O_2 [e]	0.01	None	0.14
O_3 [e]	0.002		
$^{\bullet}OH$ [e]	0.01		
NO_3 [e]	0.04		

[a] Assumed equal to m- and p-cresol.
[b] Muller & Heal (2002) reported a value for m-cresol.[10]
[c] Dievart et al. (2006) report values for 2,5-dimethylphenol and 2,6-dimethylphenol from 279-293 K.[11] We calculate an average of both values, fit an exponential function to the averaged data, and use this to predict the accommodation coefficient at low temperature. The equation is reported in the right column.
[d] Assumed equal to dimethylphenol.
[e] Citations listed in past PACT-1D publications.[5–8]
[f] All values are for the neutral form of the compound, unless otherwise noted.

Table S4. Gas-particle partitioning of phenols: Henry's Law constants, enthalpies of dissolution, saturation vapor pressures, and enthalpies of vaporization at (a) standard temperature (298 K) and (b) typical Fairbanks temperature during ALPACA (248 K).

(a) Quantities at 298 K

Compound [δ]	Henry's Law		Pankow (C_i*) Partitioning	
	K_H (M atm^{-1}) at 298 K	$\frac{-\Delta H_{sol}}{R}$ (K)	P_{sat} (atm) at 298 K	ΔH_{vap} (L atm mol^{-1})
Phenols				
phenol	6.19×10^{2} [a,49]	6400 [k,9]	3.89×10^{-4} [50]	465 [51]
o-cresol	4.30×10^{2} [b,49]	6550 [k,9]	2.75×10^{-4} [50]	739 [x,52]
m- and p-cresol	8.86×10^{2} [c,49]	7275 [k,l,9]	2.03×10^{-4} [r,50]	642 [y,52]
dimethylphenol	4.1×10^{2} [d,9]	6800 [m,9]	1.38×10^{-4} [s]	642 [z]
Diols				
catechol	4.6×10^{3} [53]	8300 [9]	5.04×10^{-5} [50]	855 [54]
resorcinol	1.0×10^{4} [53]	6300 [9]	1.63×10^{-7} [s]	855 [α]
hydroquinone	2.2×10^{7} [53]	8300 [9]	2.45×10^{-8} [s]	855 [α]
tyrosol	3.5×10^{7} [δ,15]	7633 [n]	1.80×10^{-7} [s]	855 [α]
methylcatechols	3.5×10^{7} [e]	7633 [n]	1.46×10^{-6} [t]	855 [α]
hydroxybenzaldehydes	7.7×10^{5} [f,9]	7400 [o,9]	2.92×10^{-4} [s]	855 [α]
Guaiacols				
guaicol	8.7×10^{2} [15]	7900 [9]	3.82×10^{-4} [50]	640 [55]
4-vinylguaicol	5.6×10^{2} [g]	7900 [p]	1.01×10^{-5} [s]	640 [β]
4-methylguaicol	1.1×10^{3} [56]	7900 [p]	7.82×10^{-5} [s]	700 [57]
4-ethylguaicol	5.6×10^{2} [δ,15]	7900 [p]	1.01×10^{-5} [u]	640 [β]
4-propylguaicol	4.4×10^{2} [15]	7900 [p]	2.80×10^{-6} [s]	770 [55]

eugenol	9.3×10^{2} [15]	9700 [58]	3.88×10^{-5} [50]	654 [59]
cis- & trans-isoeugenol	1.7×10^{3} δ,[15]	9700 [q]	5.01×10^{-5} [s]	682 [55]
homovanillic acid	1.2×10^{6} [h]	9700 [q]	5.66×10^{-9} [s]	640 [β]
guaicyl acetone	1.2×10^{6} [15]	9700 [q]	2.99×10^{-7} [s]	640 [β]
Syringols				
syringol	5.0×10^{3} [15]	7900 [p]	4.04×10^{-6} [s]	660 [γ]
4-methylsyringol	3.9×10^{3} δ,[15]	7900 [p]	2.63×10^{-6} [s]	660 [γ]
4-ethylsyringol	3.0×10^{3} δ,[15]	7900 [p]	8.39×10^{-7} [s]	660 [γ]
4-propylsyringol	2.2×10^{3} δ,[15]	7900 [p]	2.80×10^{-7} [s]	660 [γ]
4-allylsyringol	6.4×10^{3} δ,[15]	7900 [p]	3.07×10^{-7} [s]	660 [γ]
4-propenylsyringol	6.4×10^{3} [i]	7900 [p]	3.07×10^{-7} [v]	660 [γ]
propionyl syringol	3.8×10^{7} δ,[15]	7900 [p]	7.46×10^{-9} [w]	660 [γ]
syringyl acetone	1.2×10^{7} [15]	7900 [p]	7.46×10^{-9} [w]	660 [γ]
butyrylsyringol	3.8×10^{7} [j]	7900 [p]	7.46×10^{-9} [w]	660 [γ]
Carbonyls				
vanillin	1.72×10^{5} [9]	7900 [p]	3.31×10^{-7} [50]	660 [55]
acetovanillone	6.4×10^{5} δ,[15]	7900 [p]	1.32×10^{-7} [s]	660 [γ]
coniferylaldehyde	4.5×10^{6} δ,[15]	7900 [p]	1.37×10^{-7} [s]	660 [γ]
syringaldehyde	3.7×10^{7} δ,[15]	7900 [p]	8.54×10^{-8} [s]	660 [γ]
acetosyringone	5.1×10^{7} δ,[15]	7900 [p]	8.76×10^{-8} [s]	660 [γ]
sinapylaldehyde	3.1×10^{8} δ,[15]	7900 [p]	1.61×10^{-8} [s]	660 [γ]

[a] Average Henry's Law values reported for phenol by Feigenbrugel et al. (2004).[49]
[b] Average Henry's Law values reported for m- and p-cresol by Feigenbrugel et al. (2004).[49]
[c] Average of m- and p-cresol reported by Feigenbrugel et al. (2004).[49]
[d] Average of Henry's Law values reported for six dimethylphenols by Sander (2023).[9]
[e] Assumed equal to Henry's Law constant for tyrosol reported by McFall et al. (2020).[15]
[f] Average of 2-, 3-, and 4- hydroxybenzaldehyde reported by Sander (2023).[9] Note that the Henry's law values for these three isomers

span three order of magnitude.
[g] Assumed equal to Henry's Law constant of 4-ethylguaiacol.
[h] Assumed equal to the Henry's Law constant for guaiacyl acetone reported by McFall et al. (2020).[15]
[i] Assumed equal to Henry's Law constant of allylsyringol reported by McFall et al. (2020).[15]
[j] Assumed equal to Henry's Law constant of propionyl syringol reported by McFall et al. (2020).[15]
[k] Midpoint of highest and lowest values reported by Sander (2023).[9]
[l] Average of the highest and lowest values reported for m- and p- cresol by Sander (2023).[9]
[m] Assumed equal to 2,3-dimethylphenol reported by Sander (2023).[9]
[n] Average of o-, m-, and p-benzenediol used here, all of which are reported by Sander (2023).[9]
[o] Average of 2- and 4-hydroxybenzaldehyde reported by Sander (2023).[9]
[p] Assumed equal to guaiacol reported by Saunder (2023).[9]
[q] Assumed equal to eugenol reported by Sander (2015).[58]
[r] p-cresol vapor pressure reported by Yaw (2015) chose to represent both.
[s] Determined using EPI Suite MPBPVP Method, the Environmental Protection Agency's peer-reviewed tool for estimating vapor pressure (EPA, 2007).[60]
[t] Assumed equal to vapor pressure of catechol reported by Yaw (2015).[50]
[u] Assumed equal to vapor pressure ot 4-vinylguaiacol determined with EPI Suite MPBPVP method.
[v] Assumed equal to 4-allylsyringol as determined with EPI Suite MPBPVP method.
[w] Assumed equal to syringic acid as determined with EPI Suite MPBPVP method.
[x] Average of all values for o-cresol reported by Richard et al. (2007).[52]
[y] Average of all values reported for m- and p-cresol reported by Richard et al. (2007).[52]
[z] Assumed equal to m- and p-cresol used here.
[α] Assumed equal to value reported for catechol by Verevkin & Schick (2000).[54]
[β] Assumed equal to value for guaiacol reported by Stephensen & Malanowski (1987).[55]
[γ] Assumed equal to value for vanillin reported by Stephensen & Malanowski (1987).[55]
[δ] These values were reported by McFall et al. (2020) and were determined using EPI Suite HENRYWIN Method, the Environmental Protection Agency's peer reviewed tool for estimating Henry’s Law constants based on quantitative structure activity relationships (EPA, 2007).[60]

(b) at 248 K

Compound	K_H (M atm^{-1}) at 248 K	P_{sat} (atm) at 248 K
Phenols		
phenol	4.70×10^{4}	8.41×10^{-6}
o-cresol	3.61×10^{4}	6.21×10^{-7}
m- and p-cresol	1.22×10^{5}	1.02×10^{-6}
dimethylphenol	4.08×10^{4}	6.94×10^{-7}
Diols		
catechol	1.26×10^{6}	4.37×10^{-8}
resorcinol	7.10×10^{5}	1.41×10^{-10}
hydroquinone	6.04×10^{9}	2.13×10^{-11}
tyrosol	6.12×10^{9}	1.56×10^{-10}
methylcatechols	6.12×10^{9}	1.27×10^{-9}
hydroxybenzaldehydes	1.15×10^{8}	2.53×10^{-7}
Guaicols		
guaicol	1.82×10^{5}	1.95×10^{-6}
4-vinylguaicol	1.17×10^{5}	5.16×10^{-8}
4-methylguaicol	2.30×10^{5}	2.44×10^{-7}
4-ethylguaicol	1.17×10^{5}	5.16×10^{-8}
4-propylguaicol	9.22×10^{4}	4.90×10^{-9}

eugenol	6.59×10^{5}	1.77×10^{-7}
cis- & trans-isoeugenol	1.20×10^{6}	1.81×10^{-7}
homovanillic acid	8.50×10^{8}	2.89×10^{-11}
guaicyl acetone	8.50×10^{8}	1.53×10^{-9}
Syringols		
syringol	1.05×10^{6}	1.75×10^{-8}
4-methylsyringol	8.17×10^{5}	1.14×10^{-8}
4-ethylsyringol	6.29×10^{5}	3.63×10^{-9}
4-propylsyringol	4.61×10^{5}	1.21×10^{-9}
4-allylsyringol	1.34×10^{6}	1.33×10^{-9}
4-propenylsyringol	1.34×10^{6}	1.33×10^{-9}
propionyl syringol	7.96×10^{9}	3.23×10^{-11}
syringyl acetone	2.51×10^{9}	3.23×10^{-11}
butyrylsyringol	7.96×10^{9}	3.23×10^{-11}
Carbonyls		
vanillin	3.60×10^{7}	1.43×10^{-9}
acetovanillone	1.34×10^{8}	5.72×10^{-10}
coniferylaldehyde	9.43×10^{8}	5.94×10^{-10}
syringaldehyde	7.75×10^{9}	3.70×10^{-10}
acetosyringone	1.07×10^{10}	3.80×10^{-10}
sinapylaldehyde	6.49×10^{10}	6.98×10^{-11}

Table S5. Setschenow coefficients for ammonium sulfate

Compound	K_s (M^{-1})
Phenols [a]	
phenol	0.36 [b]
o-cresol	0.36 [b]
m- and p-cresol	0.36 [b]
dimethylphenol	0.36 [b]
Diols [a]	
catechol	0.36 [b]
resorcinol	0.36 [b]
hydroquinone	0.36 [b]
tyrosol	0.36 [b]
methylcatechols	0.36 [b]
hydroxybenzaldehydes	0.36 [b]
Guaiacols [a]	
guaicol	0.36 [15]
4-vinylguaicol	0.46 [c]
4-methylguaicol	0.46 [c]
4-ethylguaicol	0.46 [c]
4-propylguaicol	0.46 [15]
eugenol	0.40 [15]
cis- & trans-isoeugenol	0.40 [d]
homovanillic acid	0.40 [d]
guaicyl acetone	0.51 [15]
Syringols [a]	
syringol	0.51 [e]
4-methylsyringol	0.51 [e]
4-ethylsyringol	0.51 [e]
4-propylsyringol	0.51 [e]
4-allylsyringol	0.51 [e]
4-propenylsyringol	0.51 [e]
propionyl syringol	0.51 [e]
syringyl acetone	0.51 [e]
butyrylsyringol	0.51 [e]
Carbonyls [a]	
vanillin	0.65 [15]
acetovanillone	0.65 [f]
coniferylaldehyde	0.65 [f]

syringaldehyde	0.65 [f]
acetosyringone	0.65 [f]
sinapylaldehyde	0.65 [f]
Inorganic Species	
O_2	0 [g]
O_3	0.184 [h]
$^{\cdot}OH$	0 [i]
NO_3	0 [i]

[a] In PACT-1D, we use the K_s for phenols with ammonium sulfate as a proxy for the K_s for the entire system because ammonium sulfate is the dominant salt (see section S4). Here, we show the K_s values for phenols with ammonium sulfate.
[b] Assumed equal to guaiacol due to ammonium sulfate.
[c] Assumed equal to 4-propylguaiacol due to ammonium sulfate
[d] Assumed equal to eugenol due to ammonium sulfate|
[e] Assumed equal to guaiacyl acetone due to ammonium sulfate
[f] Assumed equal to vanillin due to ammonium sulfate.
[g] Battino et al. (1983) report a K_s for O_2 in ammonium sulfate of 0.212, which we have not included in our model.[61]
[h] Miyamoto et al. (2014) report the K_s for O_3 in sodium sulfate at 278.15 K.[41]
[i] No data available. The value is assumed to be 0.
[j] All values are for the neutral form of the compound, unless otherwise noted.

Table S6. Reaction rate constants of particle oxidants with some of their major sinks. Rate constants for triplet excited states with phenols are in Table S8.

Oxidant	Rate Constant (units)	Value	Source
$^{\cdot}OH$	$k_{\cdot OH+DOC}$ (L mol^{-1}-C s^{-1})	3.8(±1.9)×10^{8}	62
$^{1}O_2$*	$k'_{1O2*+H2O}$ (s^{-1})	2.8(±0.02)×10^{5}	63
	$k_{1O2*+DOC}$ (L mol^{-1}-C s^{-1})	1.6(±0.1)×10^{6}	This work (Section S7)
^{3}C*	$k_{3C*+DOC,SYR}$ (L mol^{-1}-C s^{-1}) [a]	7.0×10^{7}	30
	k_{3C*+O2} (M^{-1} s^{-1})	2.8×10^{9}	31

Table S7. Gas-phase rate constants

Compound [α]	Rate Constants [a]			
	$k_{\cdot OH+ArOH}$ (cm^3 mlc^{-1} s^{-1})	$k_{O3+ArOH}$ (cm^3 mlc^{-1} s^{-1})	$k_{NO3+ArOH}$ (cm^3 mlc^{-1} s^{-1})	j_{ArOH} (s^{-1}) [z]
Phenols				
phenol	7.95×10^{-12} [64]	3.3×10^{-19} [l]	5.89×10^{-12} [65]	0
o-cresol	4.30×10^{-11} [66]	3×10^{-19} [67]	1.56×10^{-11} [65]	0
m- and p-cresol	5.45×10^{-11} [66]	3.5×10^{-19} [m]	1.625×10^{-11} [s]	0
dimethylphenol	4.88×10^{-11} [b]	3.3×10^{-19} [l]	1.60×10^{-11} [t]	0
Diols				
catechol	7.73×10^{-13} [64]	13.5×10^{-18} [e,68]	1.60×10^{-11} [t]	0
resorcinol	2.62×10^{-11} [64]	13.5×10^{-18} [e,n]	1.60×10^{-11} [t]	0
hydroquinone	4.40×10^{-12} [64]	13.5×10^{-18} [e,n]	1.60×10^{-11} [t]	0
tyrosol	4.40×10^{-12} [c]	13.5×10^{-18} [e,n]	1.60×10^{-11} [t]	0
methylcatechols	4.40×10^{-12} [c]	13.5×10^{-18} [e,n]	1.60×10^{-11} [t]	0
hydroxybenzaldehydes	4.40×10^{-12} [c]	13.5×10^{-18} [e,n]	1.60×10^{-11} [t]	0
Guaiacols				
guaicol	7.53×10^{-11} [66]	0.4×10^{-18} [e,68]	2.69×10^{-11} [e,69]	0
4-vinylguaicol	5.44×10^{-11} [d]	2.1×10^{-17} [d]	2.69×10^{-11} [e,u]	0
4-methylguaicol	9.45×10^{-11} [e,66]	2.1×10^{-17} [o]	2.4×10^{-13} [70]	0
4-ethylguaicol	9.45×10^{-11} [e,f]	2.1×10^{-17} [o]	2.92×10^{-12} [71]	0
4-propylguaicol	9.45×10^{-11} [e,f]	2.1×10^{-17} [o]	2.92×10^{-12} [v]	0
eugenol	5.91×10^{-11} [72]	5.48×10^{-16} [72]	2.92×10^{-12} [v]	0
cis- & trans-isoeugenol	5.91×10^{-11} [g]	5.48×10^{-16} [p]	2.92×10^{-12} [v]	0
homovanillic acid	5.4×10^{-12} [h]	5.48×10^{-16} [p]	6.38×10^{-12} [w]	0
guaicyl acetone	5.4×10^{-12} [h]	5.48×10^{-16} [p]	6.38×10^{-12} [w]	4.61×10^{-7}
Syringols				

syringol	5.4×10^{-12} [69]	7.84×10^{-19} [73]	1.58×10^{-10} [69] [e]	0
4-methylsyringol	5.4×10^{-12} [i]	7.84×10^{-19} [q]	1.58×10^{-10} [e,x]	0
4-ethylsyringol	5.4×10^{-12} [i]	7.84×10^{-19} [q]	1.58×10^{-10} [e,x]	0
4-propylsyringol	5.4×10^{-12} [i]	7.84×10^{-19} [q]	1.58×10^{-10} [e,x]	0
4-allylsyringol	5.4×10^{-12} [i]	7.84×10^{-19} [q]	1.58×10^{-10} [e,x]	0
4-propenylsyringol	5.4×10^{-12} [i]	7.84×10^{-19} [q]	1.58×10^{-10} [e,x]	0
propionyl syringol	5.4×10^{-12} [i]	7.84×10^{-19} [q]	1.58×10^{-10} [e.x]	1.76×10^{-4}
syringyl acetone	5.4×10^{-12} [i]	7.84×10^{-19} [q]	1.58×10^{-10} [e,x]	1.76×10^{-4}
butyrylsyringol	5.4×10^{-12} [i]	7.84×10^{-19} [q]	1.58×10^{-10} [e,x]	1.76×10^{-4}
Carbonyls				
vanillin	5.72×10^{-12} [74]	2.52×10^{-18} [r]	6.38×10^{-12} [74]	4.70×10^{-5}
acetovanillone	5.72×10^{-12} [j]	2.52×10^{-18} [r]	6.38×10^{-12} [y]	3.45×10^{-5}
coniferylaldehyde	10.59×10^{-12} [75]	2.52×10^{-18} [r]	6.38×10^{-12} [y]	3.11×10^{-4}
syringaldehyde	12.25×10^{-12} [75]	2.52×10^{-18} [r]	6.38×10^{-12} [y]	1.76×10^{-4}
acetosyringone	12.25×10^{-12} [k]	2.52×10^{-18} [r]	6.38×10^{-12} [y]	1.93×10^{-4}
sinapylaldehyde	1.93×10^{-10} [d]	2.52×10^{-18} [r]	6.38×10^{-12} [y]	3.11×10^{-4}

[a] All values reported here were measured at 298 K unless otherwise noted.
[b] Calculated as the average of o-, m-, and p- cresol with ·OH.
[c] Assumed equal to hydroquinone with ·OH reported by Kilic et al. (2007).[64]
[d] Calculated from EPI Suite, as described by McFall et al. (2020).[15]
[e] Rate constant reported at 294 K.
[f] Assumed equal to 4-methylguaicol (creosol) with ·OH.
[g] Assumed equal to eugenol and ·OH determined by Sun et al. (2021).[72]
[h] Assumed equal to vanillic acid and ·OH reported by Sun et al (2022).[74]
[i] Assumed equal to syringol and ·OH.
[j] Assumed equal to vanillin and ·OH reported by Sun et al. (2022).[74]
[k] Assumed equal to syringaldehyde and ·OH reported by Liu et al. (2018).[75]
[l] Average of o-, m-, and p-cresol reported by Tomas et al. (2003).[67]
[m] Average of m-, and p-cresol reported by Tomas et al. (2003).[67]

[n] Assumed equal to catechol and O_3 reported by El Zein et al. (2015).[68]
[o] Assumed equal to 4-vinylguaicol and O_3 determined by EPI Suite (see footnote c).
[p] Assumed equal to eugenol and O_3 determined by Sun et al., (2021).[72]
[q] Assumed equal to syringol and O_3 reported by Liu et al. (2022).[73]
[r] Assumed equal to sinapylaldehyde and O_3 determined by EPI suite (See footnote c).
[s] Assumed equal to average of NO_3 and m-cresol and p-cresol reported by Atkinson et al., (1991).[65]
[t] Assumed equal to average of NO_3 and m-cresol, o-creso, and p-cresol reported by Atkinson et al., (1991).[65]
[u] Assumed equal to average guiacol and NO_3 reported by Lauraguais et al. (2012) at 294 K.[69]
[v] Assumed equal to NO3 + 4-ethylguaiacol reported by Wei et al. (2018) at 294 K.
[w] Assumed equal to vanillic acid and NO_3 reported by Sun et al. (2022).[74]
[x] Assumed equal to average syringol and NO_3 reported by Lauraguis et al. (2012) at 294 K.[69]
[y] Assumed equal to vanillin and NO_3 reported by Sun et al. (2022).[74]
[z] All direct photodegradation rate constants were assumed to be 7 times larger than the corresponding aqueous-phase *j*-value, based on the estimated $\Phi_{ArOH,gas}/\Phi_{ArOH,aqeous}$ ratio for phenolic carbonyl photodegradation estimated by Smith et al. (2016).[36] See equations S20 and S21.
[α] All values are for the neutral form of the compound, unless otherwise noted.

Table S8. Particle-phase rate constants I

Compound [γ]	Rate Constants (room temperature)		
	$k_{\cdot OH+ArOH}$ (L-aq mol^{-1} s^{-1})	$k_{3C*+ArOH}$ (L-aq mol^{-1} s^{-1})	$k_{1O2*+arOH}$ (L-aq mol^{-1} s^{-1})
levoglucosan	2.4×10^{9} [76]	0 [a]	0 [a]
Phenols			
phenol	1.8×10^{9} [b,c,77]	2.0×10^{9} [b,c,77]	2.6×10^{6} [v,78]
o-cresol	1.1×10^{10} [79]	2.0×10^{9} [b,c,n]	9.6×10^{6} [v,w]
m- and p-cresol	1.2×10^{10} [79]	2.0×10^{9} [b,c,n]	9.6×10^{6} [v,78]
dimethylphenol	1.15×10^{10} [d]	2.0×10^{9} [b,c,n]	9.6×10^{6} [v,w]
Diols			
catechol	2.5×10^{9} [b,c,77]	2.5×10^{9} [b,c,77]	2.9×10^{7} [x]
resorcinol	1.6×10^{9} [b,c,77]	2.9×10^{9} [b,c,77]	2×10^{7} [33]
hydroquinone	1.4×10^{9} [b,c,77]	2.6×10^{9} [b,c,77]	3.8×10^{7} [v,78]
tyrosol	1.9×10^{9} [b,c,77]	2.6×10^{9} [b,c,77]	2.9×10^{7} [x]
methylcatechols	1.4×10^{10} [80]	2.6×10^{9} [b,c,o]	2.9×10^{7} [x]
hydroxybenzaldehydes	1.4×10^{10} [e,80]	2.6×10^{9} [b,c,o]	2.9×10^{7} [x]
Guaiacols			
guaicol	6.8×10^{9} [b,c,77]	3.2×10^{9} [b,c,77]	6×10^{6} [v,78]
4-vinylguaicol	6.8×10^{9} [f]	3.2×10^{9} [b,c,p]	6×10^{6} [y]
4-methylguaicol	6.2×10^{9} [81]	3.2×10^{9} [b,c,p]	6×10^{6} [y]
4-ethylguaicol	6.2×10^{9} [g]	3.2×10^{9} [b,c,p]	6×10^{6} [y]
4-propylguaicol	6.2×10^{9} [g]	3.2×10^{9} [b,c,p]	6×10^{6} [y]
eugenol	6.2×10^{9} [g]	3.2×10^{9} [b,c,p]	6×10^{6} [y]
cis- & trans-isoeugenol	6.2×10^{9} [g]	3.2×10^{9} [b,c,p]	6×10^{6} [y]
homovanillic acid	1×10^{10} [h,b,c]	3.3×10^{9} [b,c,q]	6×10^{6} [y]
guaicyl acetone	6.8×10^{9} [c,82]	3.3×10^{9} [b,c,77]	6×10^{6} [y]

Syringols			
syringol	1.5×10^{10} b,c,77	6.7×10^{9} b,c,77	3.6×10^{7} v,78
4-methylsyringol	1.5×10^{10} i,b,c	6.7×10^{9} b,c,r	3.6×10^{7} z
4-ethylsyringol	1.5×10^{10} i,b,c	6.7×10^{9} b,c,r	3.6×10^{7} z
4-propylsyringol	1.5×10^{10} i,b,c	6.7×10^{9} b,c,r	3.6×10^{7} z
4-allylsyringol	1.5×10^{10} i,b,c	6.7×10^{9} b,c,r	3.6×10^{7} z
4-propenylsyringol	1.5×10^{10} i,b,c	6.7×10^{9} b,c,r	3.6×10^{7} z
propionyl syringol	1.4×10^{10} j,c	4.5×10^{9} b,c,s	3.6×10^{7} z
syringyl acetone	1.4×10^{10} c,82	4.5×10^{9} b,c,83	3.6×10^{7} z
butyrylsyringol	1.4×10^{10} j,c	4.5×10^{9} b,c,s	3.6×10^{7} z
Carbonyls			
vanillin	4×10^{8} 84	3.0×10^{9} b,c,t	4.6×10^{6} 85
acetovanillone	4×10^{8} k	3.0×10^{9} b,c,t	4.6×10^{6} α
coniferylaldehyde	1.3×10^{10} l,c	3.4×10^{9} b,c,u	1.6×10^{7} 85
syringaldehyde	3.7×10^{10} m,85,86	4.5×10^{9} b,c,s	1.84×10^{7} 85
acetosyringone	1.4×10^{10} j,c	4.5×10^{9} b,c,s	4.6×10^{6} α
sinapylaldehyde	1.4×10^{10} j,c	4.5×10^{9} b,c,s	1.84×10^{7} β

[a] No data available so we assume zero based on the molecular structure.
[b] Measured at 293 K.
[c] Measured at pH 2.
[d] Average of o-, m-, and p-cresol with ˙OH.
[e] Assumed equal to methylcatechols and ˙OH reported by Kroflič et al. (2020).[80]
[f] Assumed equal to guaiacol with ˙OH at pH 2 measured at 293 K measured by Smith et al. (2015).[77]
[g] Assumed equal to 4-methylguaiacol and ˙OH reported by He et al. (2019).[81]
[h] Assumed equal to vanillic acid and ˙OH reported by Tang et al. (2020)[87] at pH 2 and 293 K.
[i] Assumed equal to syringol and ˙OH reported by Smith et al. (2015) at pH 2 and 293 K.[77]
[j] Assumed equal to syringyl acetone and ˙OH reported by Arciva et al. (2022) at pH 2.[82,84]
[k] Assumed equal to vanillin and ˙OH estimated by Li et al. (2014).[84]
[l] Assumed equal to ˙OH and trans-ferulic acid determined by Arciva et al. (2022).[82]

[m] Rate constant reported for the neutral form. pK_a is reported by An et al. (2020) as 7.165.[86]
[n] Assumed equal to phenol and $^3C^*$ reported by Smith et al. (2015) at pH 2 at 293 K.[77]
[o] Assumed equal to tyrosol and $^3C^*$ reported by Smith et al. (2015) at pH 2 at 293 K.[77]
[p] Assumed equal to guaicol+ 3C* reported by Smith et al. (2015) at pH 2 at 293 K.[77]
[q] Assumed equal to guaicyl acetone and $^3C^*$ reported by Smith et al. (2015) at pH 2 at 293 K.[77]
[s] Assumed equal to syringyl acetone and $^{\cdot}OH$ reported by Ma et al. (2021) at pH 2 and 293 K.[83]
[t] Assumed equal to vanillyl alcohol and $^{\cdot}OH$ reported by Ma et al. (2021) at pH 2 and 293 K.[83]
[u] Assumed equal to trans-ferulic acid and $^{\cdot}OH$ reported by Ma et al. (2021) at pH 2 and 293 K.[83]
[v] Reported at 290 K for the neutral form of phenol.
[w] Assumed equal to m- and p-cresol and $^1O_2^*$ reported by Tratnyek et al. (1991).[78]
[x] Average of resorcinol and hydroquinone.
[y] Assumed equal to guaicol and $^1O_2^*$ reported by Tratnyek & Holgne (1991).[78]
[z] Assumed equal to syingol and $^1O_2^*$ reported by Tratnyek & Holgne (1991).[78]
[α] Assumed equal to vanillin and $^1O_2^*$ reported by Zhou et al. (2023).[85]
[β] Assumed equal to syringaldehyde and $^1O_2^*$ reported by Zhou et al. (2023).[85]
[γ] All values are for the neutral form of the compound, unless otherwise noted.

Table S9. Particle-phase rate constants II

Compound [u]	Rate Constants (room temperature)		
	$k_{NO3+ArOH}$ (L-aq mol^{-1} s^{-1})	$k_{O3+ArOH}$ (L-aq mol^{-1} s^{-1})	j_{ArOH} (s^{-1})
levoglucosan	1.6×10^{7} [76]	0 [a]	0 [a]
Phenols			
phenol	1.8×10^{9} [88]	1.3×10^{3} [h,89]	0
o-cresol	1.7×10^{9} [c]	5.7×10^{3} [h,90]	0
m- and p-cresol	1.7×10^{9} [b,88]	1.0×10^{4} [h,i,90]	0
dimethoxyphenol	1.7×10^{9} [c]	8.6×10^{3} [h,j]	0
Diols			
catechol	8.8×10^{8} [d]	2.9×10^{5} [h,90]	0
resorcinol	8.8×10^{8} [d]	9.1×10^{4} [h,90]	0
hydroquinone	8.8×10^{8} [88]	1.4×10^{6} [h,90]	0
tyrosol	8.8×10^{8} [d]	6.0×10^{5} [h,k]	0
methylcatechols	8.8×10^{8} [d]	6.0×10^{5} [h,k]	0
hydroxybenzaldehydes	8.8×10^{8} [d]	6.0×10^{5} [h,k]	0
Guaiacols			
guaicol	2.5×10^{9} [88]	5×10^{5} [l,91]	0
4-vinylguaicol	1.0×10^{9} [e]	5×10^{5} [m]	0
4-methylguaicol	1.0×10^{9} [e]	5×10^{5} [m]	0
4-ethylguaicol	1.0×10^{9} [e]	5×10^{5} [m]	0
4-propylguaicol	1.0×10^{9} [e]	5×10^{5} [m]	0
eugenol	1.0×10^{9} [e]	5×10^{5} [m]	0
cis- & trans-isoeugenol	1.0×10^{9} [e]	5×10^{5} [m]	0
homovanillic acid	1.0×10^{9} [e]	0 [n]	0
guaicyl acetone	1.0×10^{9} [e]	0 [n]	1.65×10^{-7} [r]
Syringols			

syringol	1.4×10^{9} [f]	5×10^{5} [m]	0
4-methylsyringol	1.4×10^{9} [f]	5×10^{5} [m]	0
4-ethylsyringol	1.4×10^{9} [f]	5×10^{5} [m]	0
4-propylsyringol	1.4×10^{9} [f]	5×10^{5} [m]	0
4-allylsyringol	1.4×10^{9} [f]	5×10^{5} [m]	0
4-propenylsyringol	1.4×10^{9} [f]	5×10^{5} [m]	0
propionyl syringol	1.4×10^{9} [f]	5×10^{5} [m]	6.27×10^{-5} [s]
syringyl acetone	1.4×10^{9} [f]	5×10^{5} [m]	6.27×10^{-5} [s]
butyrylsyringol	1.4×10^{9} [f]	5×10^{5} [m]	6.27×10^{-5} [s]
Carbonyls			
vanillin	1.7×10^{9} [g]	5.4×10^{5} [o,92]	1.68×10^{-5} [r]
acetovanillone	1.7×10^{9} [g]	4.1×10^{3} [93]	1.23×10^{-5} [r]
coniferylaldehyde	1.7×10^{9} [g]	5.4×10^{5} [o,p]	1.11×10^{-4} [r]
syringaldehyde	1.7×10^{9} [88]	2.9×10^{5} [93]	6.27×10^{-5} [r]
acetosyringone	1.7×10^{9} [g]	3.6×10^{5} [93]	6.90×10^{-5} [r]
sinapylaldehyde	1.7×10^{9} [g]	2.9×10^{5} [q]	1.11×10^{-4} [t]

[a] No data available so we assume this is zero based on the molecular structure.
[b] Weller et al. (2010) report the rate constant for p-methyl phenol.
[c] Assumed equal to the rate constant of NO_3 with p-methyl phenol reported by Weller et al. (2010).[88]
[d] Assumed equal to the rate constant of NO_3 with p-hydroxy phenol (hydroquinone) reported by Weller et al. (2010).[88]
[e] Assumed equal to the rate constant of NO_3 with vanillic acid reported by Weller et al. (2010).[88]
[f] Assumed equal to the rate constant of NO_3 with syringic acid reported by Weller et al. (2010).[88]
[g] Assumed equal to the rate constant of NO_3 with syringaldehyde reported by Weller et al. (2010).[88]
[h] Measured at 293 K.
[i] Average of m- and p-cresol reported by Gurol et al. (1984).[90]
[j] Average of o-, m-, and p-cresol reported by Gurol et al. (1984).[90]
[k] Average of catechol, resorcinol, and hydroquinone reported by Gurol et al. (1984).[90]
[l] Khudoshin et al. (2008) reports a lower bound for the rate constant of O_3 with guaiacol, which is used here.
[m] Assumed equal to the rate constant of O_3 with guaiacol reported by Khudoshin et al. (2008).[91]

[n] Assumed equal to the rate constant of O_3 with veratric acid reported by Ragnar et al. (1999).[93]
[o] Reported at 296 K.
[p] Assumed equal to the rate constant of vanillin and with O_3 reported by Wang et al. (2021).[92]
[q] Assumed equal to the rate constant of syringaldehyde and ozone reported by Ragnar et al. (1999).[93]
[r] Molar absorptivity and photolysis quantum yield reported by Smith et al. (2016) and calculated here for the actinic flux at solar noon in Fairbanks, Alaska on 1/30/2022.[36] This calculation includes optical confinement in the condensed phase (equation S20).
[s] Assumed equal to syringaldedehyde.
[t] Assumed equal to coniferylaldehyde.
[u] All values are for the neutral form of the compound, unless otherwise noted.

Table S10. Gas-phase SOA yields

Compound [o]	SOA Mass Yield			
	$Y_{SOA,\cdot OH+ArOH}$	$Y_{SOA,O3+ArOH}$	$Y_{SOA,NO3+ArOH}$	$Y_{SOA,h\nu}$ [n]
Phenols				
phenol	0.33 [a,94]	0.52 [g]	0.21 [k]	0
o-cresol	0.33 [b]	0.52 [g]	0.21 [k]	0
m- and p-cresol	0.33 [b]	0.52 [g]	0.21 [k]	0
dimethylphenol	0.33 [b]	0.52 [g]	0.21 [k]	0
Diols				
catechol	0.33 [b]	0.52 [h,95]	0.21 [k]	0
resorcinol	0.33 [b]	0.52 [g]	0.21 [k]	0
hydroquinone	0.33 [b]	0.52 [g]	0.21 [k]	0
tyrosol	0.33 [b]	0.52 [g]	0.21 [k]	0
methylcatechols	0.33 [b]	0.50 [I,95]	0.21 [k]	0
hydroxybenzaldehydes	0.33 [b]	0.50 [j]	0.21 [k]	0
Guaiacols				
guaicol	0.47 [a,94]	0.50 [j]	0.21 [l,96]	0
4-vinylguaicol	0.47 [c]	0.50 [j]	0.21 [k]	0
4-methylguaicol	0.47 [c]	0.50 [j]	0.21 [k]	0
4-ethylguaicol	0.47 [c]	0.50 [j]	0.21 [k]	0
4-propylguaicol	0.47 [c]	0.50 [j]	0.21 [k]	0
eugenol	0.31 [d,73]	0.50 [j]	0.21 [k]	0
cis- & trans-isoeugenol	0.31 [e]	0.50 [j]	0.21 [k]	0
homovanillic acid	0.31 [e]	0.50 [j]	0.21 [k]	0
guaicyl acetone	0.31 [e]	0.50 [j]	0.21 [k]	0.31 [m]
Syringols				
syringol	0.32 [a,94]	0.50 [j]	0.21 [k]	0

4-methylsyringol	0.32 [f]	0.50 [j]	0.21 [k]	0
4-ethylsyringol	0.32 [f]	0.50 [j]	0.21 [k]	0
4-propylsyringol	0.32 [f]	0.50 [j]	0.21 [k]	0
4-allylsyringol	0.32 [f]	0.50 [j]	0.21 [k]	0
4-propenylsyringol	0.32 [f]	0.50 [j]	0.21 [k]	0
propionyl syringol	0.32 [f]	0.50 [j]	0.21 [k]	0.32 [m]
syringyl acetone	0.32 [f]	0.50 [j]	0.21 [k]	0.32 [m]
butyrylsyringol	0.32 [f]	0.50 [j]	0.21 [k]	0.32 [m]
Carbonyls				
vanillin	0.47 [c]	0.50 [j]	0.21 [k]	0.47 [m]
acetovanillone	0.47 [c]	0.50 [j]	0.21 [k]	0.47 [m]
coniferylaldehyde	0.47 [c]	0.50 [j]	0.21 [k]	0.47 [m]
syringaldehyde	0.47 [c]	0.50 [j]	0.21 [k]	0.47 [m]
acetosyringone	0.47 [c]	0.50 [j]	0.21 [k]	0.47 [m]
sinapylaldehyde	0.47 [c]	0.50 [j]	0.21 [k]	0.47 [m]

[a] The average of four yields reported from four separate experiments by Yee et al. (2013).[94]
[b] Assumed equal to the phenol and ·OH yield used in this work.
[c] Assumed equal to the guaiacol and ·OH yield used in this work.
[d] Upper bound of SOA yield range reported by Liu et al. (2022).[73]
[e] Assumed equal to the eugenol and ·OH value used in this work.
[f] Assumed equal to the syringol and ·OH yield used in this work.
[g] Assumed equal to the catechol yield used in this work.
[h] Midpoint value of range of values reported for SOA yield of catechol + ozone reported by Coeur-Tournoeur et al. (2008).[95]
[i] Midpoint value of all eighteen yields reported for ozone with 3-methylcatechol and 4-methylcatechol reported by Coeur-Tournoeur et al. (2009).[95]
[j] Assumed equal to methylcatechol and ozone yield used here.
[k] Assumed equal to yield of NO_3 and guaiacol used in this work.
[l] Equal to upper bound of yields for NO_3 and guaiacol reported by Meng et al. (2020).[96]
[m] Assumed equal to the SOA yield for ·OH with each individual phenol.

[n] $Y_{SOA,hv}$ is the SOA yield for direct photodegradation.
[o] All values are for the neutral form of the compound, unless otherwise noted.

Table S11. Particle-phase SOA yields

Compound [r]	SOA Mass Yield					
	$Y_{SOA,\cdot OH+ArOH}$	$Y_{SOA,3C*+ArOH}$	$Y_{SOA,1O2*+ArOH}$	$Y_{SOA,NO3+ArOH}$	$Y_{SOA,O3+ArOH}$	$Y_{SOA,h\nu}$ [q]
Phenols						
phenol	1.07 [97]	1.13 [97]	1 [n]	1 [n]	1 [n]	0
o-cresol	1.07 [a]	1.13 [f]	1 [n]	1 [n]	1 [n]	0
m- and p-cresol	1.07 [a]	1.13 [f]	1 [n]	1 [n]	1 [n]	0
dimethylphenol	1.07 [a]	1.13 [f]	1 [n]	1 [n]	1 [n]	0
Diols						
catechol	0.80 [77]	0.72 [77]	1 [n]	1 [n]	1 [n]	0
resorcinol	0.59 [77]	1.12 [77]	1 [n]	1 [n]	1 [n]	0
hydroquinone	0.82 [77]	1.13 [77]	1 [n]	1 [n]	1 [n]	0
tyrosol	0.74 [b]	0.99 [g]	1 [n]	1 [n]	1 [n]	0
methylcatechols	0.74 [b]	0.99 [g]	1 [n]	1 [n]	1 [n]	0
hydroxybenzaldehydes	0.74 [b]	0.99 [g]	1 [n]	1 [n]	1 [n]	0
Guaiacols						
guaicol	1.09 [97]	0.94 [97]	1 [n]	1 [n]	1 [n]	0
4-vinylguaicol	1.09 [c]	0.94 [h]	1 [n]	1 [n]	1 [n]	0
4-methylguaicol	1.09 [c]	0.94 [h]	1 [n]	1 [n]	1 [n]	0
4-ethylguaicol	1.09 [c]	0.585 [98]	1 [n]	1 [n]	1 [n]	0
4-propylguaicol	1.09 [c]	0.585 [i]	1 [n]	1 [n]	1 [n]	0
eugenol	1.09 [c]	0.585 [i]	1 [n]	1 [n]	1 [n]	0
cis- & trans-isoeugenol	1.09 [c]	0.585 [i]	1 [n]	1 [n]	1 [n]	0
homovanillic acid	1.09 [c]	0.85 [j]	1 [n]	1 [n]	1 [n]	0
guaicyl acetone	1.09 [c]	0.85 [83]	1 [n]	1 [n]	1 [n]	0.87 [o]
Syringols						
syringol	1.14 [77]	0.83 [97]	1 [n]	1 [n]	1 [n]	0

4-methylsyringol	1.14 [d]	0.83 [k]	1 [n]	1 [n]	1 [n]	0
4-ethylsyringol	1.14 [d]	0.83 [k]	1 [n]	1 [n]	1 [n]	0
4-propylsyringol	1.14 [d]	0.83 [k]	1 [n]	1 [n]	1 [n]	0
4-allylsyringol	1.14 [d]	0.83 [k]	1 [n]	1 [n]	1 [n]	0
4-propenylsyringol	1.14 [d]	0.83 [k]	1 [n]	1 [n]	1 [n]	0
propionyl syringol	1.14 [d]	0.99 [l]	1 [n]	1 [n]	1 [n]	0.87 [o]
syringyl acetone	1.14 [d]	0.99 [l]	1 [n]	1 [n]	1 [n]	0.87 [o]
butyrylsyringol	1.14 [d]	0.99 [l]	1 [n]	1 [n]	1 [n]	0.87 [o]
Carbonyls						
vanillin	0.87 [e]	0.59 [m]	1 [n]	1 [n]	1 [n]	0.81 [99]
acetovanillone	0.87 [e]	0.59 [m]	1 [n]	1 [n]	1 [n]	0.82 [99]
coniferylaldehyde	0.87 [e]	0.99 [l]	1 [n]	1 [n]	1 [n]	1.20 [99]
syringaldehyde	0.87 [e]	0.99 [l]	1 [n]	1 [n]	1 [n]	1.20 [p]
acetosyringone	0.87 [e]	0.99 [l]	1 [n]	1 [n]	1 [n]	1.20 [p]
sinapylaldehyde	0.87 [e]	0.99 [l]	1 [n]	1 [n]	1 [n]	1.20 [p]

[a] Assumed equal to the yield of ·OH and phenol reported by Smith et al. (2014).[100]
[b] Average of o-, m-, and p-cresol reported by Smith et al. (2015).[77]
[c] Assumed equal to yield of ·OH and guaiacol reported by Smith et al. (2015).[77]
[d] Assumed equal to yield of ·OH and syringol reported by Smith et al. (2015).[77]
[e] Average of yield of ·OH with 12 substituted phenols reported by Arciva et al. (2022).[82]
[f] Assumed to be equal to yield of ^{3}C* with phenol reported by Smith et al. (2014).[97]
[g] Assumed to be equal to average yield of ^{3}C* with o-, m-, and p-cresol reported by Smith et al. (2015).[77]
[h] Assumed equal to the yield of ^{3}C* and guaiacol reported by Smith et al. (2014).[97]
[i] Assumed equal to yield of ^{3}C* and ethylguaiacol reported by Chen et al. (2020).[98]
[j] Assumed equal to yield of ^{3}C* and guaiacyl acetone reported by Ma et al. (2021).[83]
[k] Assumed equal to yield of ^{3}C* with syringol reported by Smith et al. (2014).[97]
[l] Assumed equal to yield of ^{3}C* with syringylacetone reported by Ma et al. (2021).[83]
[m] Assumed equal to yield of ^{3}C* with vanillyl alcohol reported by Ma et al. (2021).[83]
[n] No data on yield; we assume a value of 1.
[o] Assumed equal to the average yield from direct photodegradation of all substituted phenols reported by Smith et al. (2016).[36]

[p] Assumed equal to the yield from direct photodegradation of coniferylaldehyde reported by Smith et al. (2016).[36]
[q] $Y_{SOA,hv}$ is the SOA yield for direct photodegradation.
[r] All values are for the neutral form of the compound, unless otherwise noted.

Table S12. Gas-phase activation energies

Compound [i]	Activation Energy (kJ mol^{-1})		
	$E_{a,\cdot OH+ArOH}$	$E_{a,O3+ArOH}$	$E_{a,NO3+ArOH}$
Phenols			
phenol	10.96 [a]	39.7 [101]	4.9 [102]
o-cresol	10.96 [b]	39.7 [e]	4.9 [f]
m- and p-cresol	10.96 [b]	39.7 [e]	4.9 [f]
dimethylphenol	10.96 [b]	39.7 [e]	4.9 [f]
Diols			
catechol	8.95 [a]	39.7 [e]	4.9 [f]
resorcinol	6.40 [a]	39.7 [e]	4.9 [f]
hydroquinone	10.40 [a]	39.7 [e]	4.9 [f]
tyrosol	8.58 [c]	39.7 [e]	4.9 [f]
methylcatechols	8.58 [c]	39.7 [e]	4.9 [f]
hydroxybenzaldehydes	8.58 [c]	39.7 [e]	4.9 [f]
Guaiacols			
guaicol	8.95 [d]	39.7 [e]	7.9 [g]
4-vinylguaicol	8.95 [d]	39.7 [e]	7.9 [g]
4-methylguaicol	8.95 [d]	39.7 [e]	7.9 [g]
4-ethylguaicol	8.95 [d]	39.7 [e]	7.9 [70]
4-propylguaicol	8.95 [d]	39.7 [e]	7.9 [g]
eugenol	8.95 [d]	39.7 [e]	12.8 [70]
cis- & trans-isoeugenol	8.95 [d]	39.7 [e]	12.8 [h]
homovanillic acid	8.95 [d]	39.7 [e]	12.8 [h]
guaicyl acetone	8.95 [d]	39.7 [e]	12.8 [h]
Syringols			
syringol	8.95 [d]	39.7 [e]	12.8 [h]

4-methylsyringol	8.95 [d]	39.7 [e]	12.8 [h]
4-ethylsyringol	8.95 [d]	39.7 [e]	12.8 [h]
4-propylsyringol	8.95 [d]	39.7 [e]	12.8 [h]
4-allylsyringol	8.95 [d]	39.7 [e]	12.8 [h]
4-propenylsyringol	8.95 [d]	39.7 [e]	12.8 [h]
propionyl syringol	8.95 [d]	39.7 [e]	12.8 [h]
syringyl acetone	8.95 [d]	39.7 [e]	12.8 [h]
butyrylsyringol	8.95 [d]	39.7 [e]	12.8 [h]
Carbonyls			
vanillin	8.95 [d]	39.7 [e]	12.8 [h]
acetovanillone	8.95 [d]	39.7 [e]	12.8 [h]
coniferylaldehyde	8.95 [d]	39.7 [e]	12.8 [h]
syringaldehyde	8.95 [d]	39.7 [e]	12.8 [h]
acetosyringone	8.95 [d]	39.7 [e]	12.8 [h]
sinapylaldehyde	8.95 [d]	39.7 [e]	12.8 [h]

[a] Lowest activation energy reported by Kiliç et al. (2007) based on computational modeling of several reaction pathways.[64]
[b] Assumed equal to phenol and ·OH.
[c] Average of catechol, resorcinol, and hydroquinone reported here.
[d] Assumed equal to catechol.
[e] Assumed equal to phenol and ozone reported by Hendrickx et al. (2003).[101]
[f] Assumed equal to phenol and NO_3 reported by Wei et al. (2021).[70,103]
[g] Assumed equal to 4-ethylguaicol and NO_3 reported by Zhang et al. (2016).[70]
[h] Assumed equal to eugenol and NO_3 reported by Zhang et al. (2016).[70]
[i] All values are for the neutral form of the compound, unless otherwise noted.

Table S13. Particle-phase activation energies

Compound [u]	Activation Energy (kJ mol^{-1})				
	$E_{a,\cdot OH+ArOH}$	$E_{a,3C*+ArOH}$	$E_{a,1O2*+ArOH}$	$E_{a,NO3+ArOH}$	$E_{a,O3+ArOH}$
Phenols					
phenol	18 [80]	0 [i]	40.2 [j,104]	17 [k]	51.9 [q]
o-cresol	18 [a]	0 [i]	40.2 [j,104]	22 [88]	51.9 [q]
m- and p-cresol	18 [a]	0 [i]	40.2 [j,104]	6.0 [l,88]	51.9 [q]
dimethylphenol	18 [a]	0 [i]	40.2 [j,104]	17 [k]	51.9 [q]
Diols					
catechol	17 [80]	0 [i]	40.2 [j,104]	39 [88]	51.9 [q]
resorcinol	17 [b]	0 [i]	40.2 [j,104]	16 [m]	51.9 [q]
hydroquinone	17 [b]	0 [i]	40.2 [j,104]	16 [m]	51.9 [q]
tyrosol	20 [c]	0 [i]	40.2 [j,104]	16 [m]	51.9 [q]
methylcatechols	20 [80]	0 [i]	40.2 [j,104]	16 [m]	51.9 [r,105]
hydroxybenzaldehydes	20 [c]	0 [i]	40.2 [j,104]	16 [m]	51.9 [q]
Guaiacols					
guaicol	17.3 [81]	0 [i]	40.2 [j,104]	25 [88]	51.9 [q]
4-vinylguaicol	17.3 [d]	0 [i]	40.2 [j,104]	26 [n]	51.9 [q]
4-methylguaicol	15.5 [81]	0 [i]	40.2 [j,104]	26 [n]	51.9 [q]
4-ethylguaicol	15.5 [e]	0 [i]	40.2 [j,104]	26 [n]	51.9 [q]
4-propylguaicol	15.5 [e]	0 [i]	40.2 [j,104]	26 [n]	51.9 [q]
eugenol	15.5 [e]	0 [i]	40.2 [j,104]	26 [n]	51.9 [q]
cis- & trans-isoeugenol	15.5 [e]	0 [i]	40.2 [j,104]	26 [n]	51.9 [q]
homovanillic acid	9.73 [f]	0 [i]	40.2 [j,104]	15 [p]	0 [s]
guaicyl acetone	9.73 [f]	0 [i]	40.2 [j,104]	15 [p]	0 [s]
Syringols					
syringol	9.73 [f]	0 [i]	40.2 [j,104]	16 [88]	51.9 [q]

4-methylsyringol	9.73 [f]	0 [i]	40.2 [j,104]	15 [o]	51.9 [q]
4-ethylsyringol	9.73 [f]	0 [i]	40.2 [j,104]	15 [o]	51.9 [q]
4-propylsyringol	9.73 [f]	0 [i]	40.2 [j,104]	15 [o]	51.9 [q]
4-allylsyringol	9.73 [f]	0 [i]	40.2 [j,104]	15 [o]	51.9 [q]
4-propenylsyringol	9.73 [f]	0 [i]	40.2 [j,104]	16 [m]	51.9 [q]
propionyl syringol	9.73 [f]	0 [i]	40.2 [j,104]	16 [m]	51.9 [q]
syringyl acetone	9.73 [f]	0 [i]	40.2 [j,104]	16 [m]	51.9 [q]
butyrylsyringol	9.73 [f]	0 [i]	40.2 [j,104]	16 [m]	51.9 [q]
Carbonyls					
vanillin	9.73 [f]	0 [i]	40.2 [j,104]	16 [88]	34.09 [t]
acetovanillone	12.61 [g]	0 [i]	40.2 [j,104]	16 [m]	34.09 [t]
coniferylaldehyde	12.61 [75]	0 [i]	40.2 [j,104]	16 [m]	34.09 [t]
syringaldehyde	10.90 [75]	0 [i]	40.2 [j,104]	18 [88]	34.09 [106]
acetosyringone	10.9 [h]	0 [i]	40.2 [j,104]	16 [m]	34.09 [t]
sinapylaldehyde	10.9 [h]	0 [i]	40.2 [j,104]	16 [m]	34.09 [t]

[a] Assumed equal to activation energy for ·OH and phenol reported by Kroflič et al. (2020).[80]
[b] Assumed equal to activation energy for ·OH and catechol reported by Kroflič et al. (2020).[80]
[c] Assumed equal to activation energy for ·OH and 3-methylcatechol reported by Kroflic et al. (2020).[80]
[d] Assumed equal to the activation energy of guaiacol and ·OH reported by He at al. (2019).[81]
[e] Assumed equal to activation energy of creosol and ·OH reported by He et al. (2019).[81]
[f] Assumed equal to the activation energy of vanillic acid and ·OH reported by Liu et al. (2018).[75]
[g] Assumed equal to the activation energy of coniferylaldehyde and ·OH reported by Liu et al. (2018).[75]
[h] Assumed equal to the activation energy of syringaldehyde and ·OH reported by Liu et al. (2018).[75]
[i] Smith et al., 2014 found no temperature dependence of $^3C^*$ reactions with phenol, guaiacol, and syringol between 25 and 5 °C. Based on this, we assume the activation energy for reactions of triplet excited states is zero.
[j] Assumed equal to activation energy of $^1O_2^*$ and tyrosine reported by Richards-Henderson et al. (2015).[104]
[k] Average of activation energies for NO_3 with o-cresol and p-cresol reported by Weller et al. (2010).[88]
[l] Weller et al. (2010) reports a value for p-cresol.[88]
[m] Average of activation energy for NO_3 and polysubstituted phenols measured by Weller et al. (2010).[88]
[n] Average activation energy for NO_3 with two substituted phenols reported by Weller et al. (2010).[88]

[o] Average activation energy for NO_3 with 2,6-substituted phenols reported by Weller et al. (2010).[88]
[p] Assumed equal to activation energy for NO_3 with vanillic acid reported by Weller et al. (2010).[88]
[q] Assumed equal to the activation energy of O_3 with methylcatechol used here.
[r] Sun et al. (2019) reports a gas phase activation energy of 74.1 kJ mol^{-1} as well as a difference in the gas- and aqueous-phase activation energy, with the aqueous-phase value being 22.2 kJ mol^{-1} less than the gas-phase value due to the solvation effect.[105] Here, we use the difference to calculate the aqueous-phase activation energy of 51.9 kJ mol^{-1}.
[s] No reaction.
[t] Assumed equal to activation energy of O_3 with syringaldehyde reported by Benitez et al. (1998).[106]
[u] All values are for the neutral form of the compound, unless otherwise noted.

Table S14. List of phenols on the x-axis of Figure 4, organized by modeled saturation concentration (C_i*) at 1:00 PM on 1/31/2022. C_i* and K_H values are for the ambient temperature (-30 °C).

Compound Name	C_i* (μg m^{-3})	K_H (M atm^{-1})
hydroquinone	0.088	1.2×10^{9}
homovanillic acid	0.16	1.5×10^{8}
butyrylsyringol	0.17	5.5×10^{8}
propionyl syringol	0.17	5.5×10^{8}
syringyl acetone	0.17	1.7×10^{9}
sinapyladehyde	0.37	1.7×10^{9}
resorcinol	0.59	1.2×10^{5}
tyrosol	0.65	1.2×10^{9}
syringaldehyde	2.0	2.0×10^{8}
acetosyringone	2.0	2.8×10^{8}
acetovanillone	3.0	3.5×10^{6}
coniferylaldehyde	3.2	2.5×10^{7}
methylcatechols	5.2	1.2×10^{9}
propylsyringol	6.4	3.2×10^{4}
methoxyeugenol	7.1	9.2×10^{5}
cis-syringylprop-1-ene	7.1	9.2×10^{5}
vanillin	7.6	9.4×10^{5}
guaiacyl acetone	8.4	7.1×10^{7}
ethylsyringol	19	4.3×10^{4}
cerulignol	23	9.0×10^{3}
methylsyringol	61	5.6×10^{4}
syringol	93	7.2×10^{4}
catechol	181	2.6×10^{4}
vinylguaiacol	283	1.1×10^{4}
ethylguaiacol	283	1.1×10^{4}
isoeugenol	937	2.1×10^{5}
eugenol	945	1.2×10^{5}
hydroxybenzaldehydes	1.0×10^{3}	2.1×10^{7}
creosol	1.2×10^{3}	2.1×10^{3}
o-cresol	3.0×10^{3}	6.1×10^{3}
dimethylphenol	3.8×10^{3}	7.0×10^{3}
m- & p-cresol	5.6×10^{3}	2.2×10^{4}
guaiacol	9.2×10^{3}	3.5×10^{4}
phenol	5.8×10^{4}	6.3×10^{3}

Figure S1. Composition of organic aerosol during ALPACA. Organic aerosol (OA) was measured with a HR-ToF-MS during ALPACA. Biomass burning organic aerosol (BBOA) and oxidized organic aerosol (OOA) were determined with positive matrix factorization of CHARON data, as reported by Ijaz et al. (2025).[21] Other factors not included here were cooking organic aerosol, hydrocarbon-like organic aerosol, a sulfur-containing organic aerosol, and an organic-nitrate-containing organic aerosol.

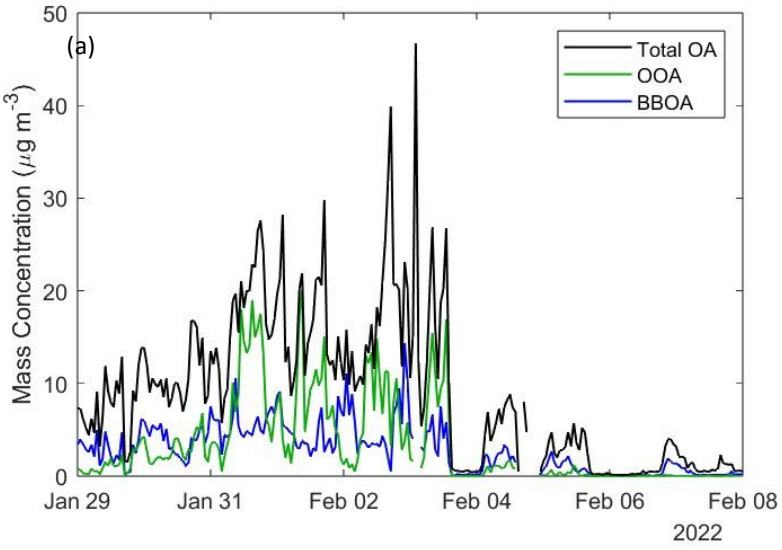

Figure S2. Particle composition: comparison of PACT-1D modeling with measurements of a) aerosol liquid water[16] and b) organic aerosol.[21]

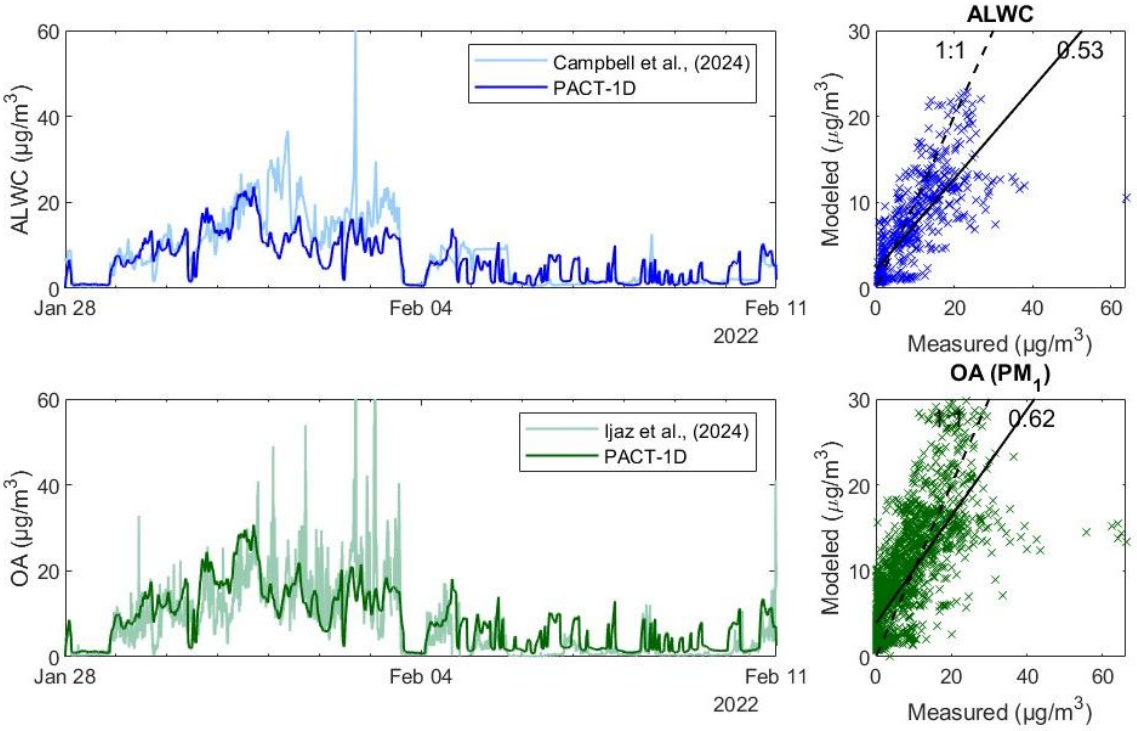

Figure S3. (a) Simulated and measured levoglucosan concentrations in the polluted surface layer. (b) Hardwood and softwood fractions of BBOA determined with positive matrix factorization.[21] Note the different date ranges on the *x* axes.

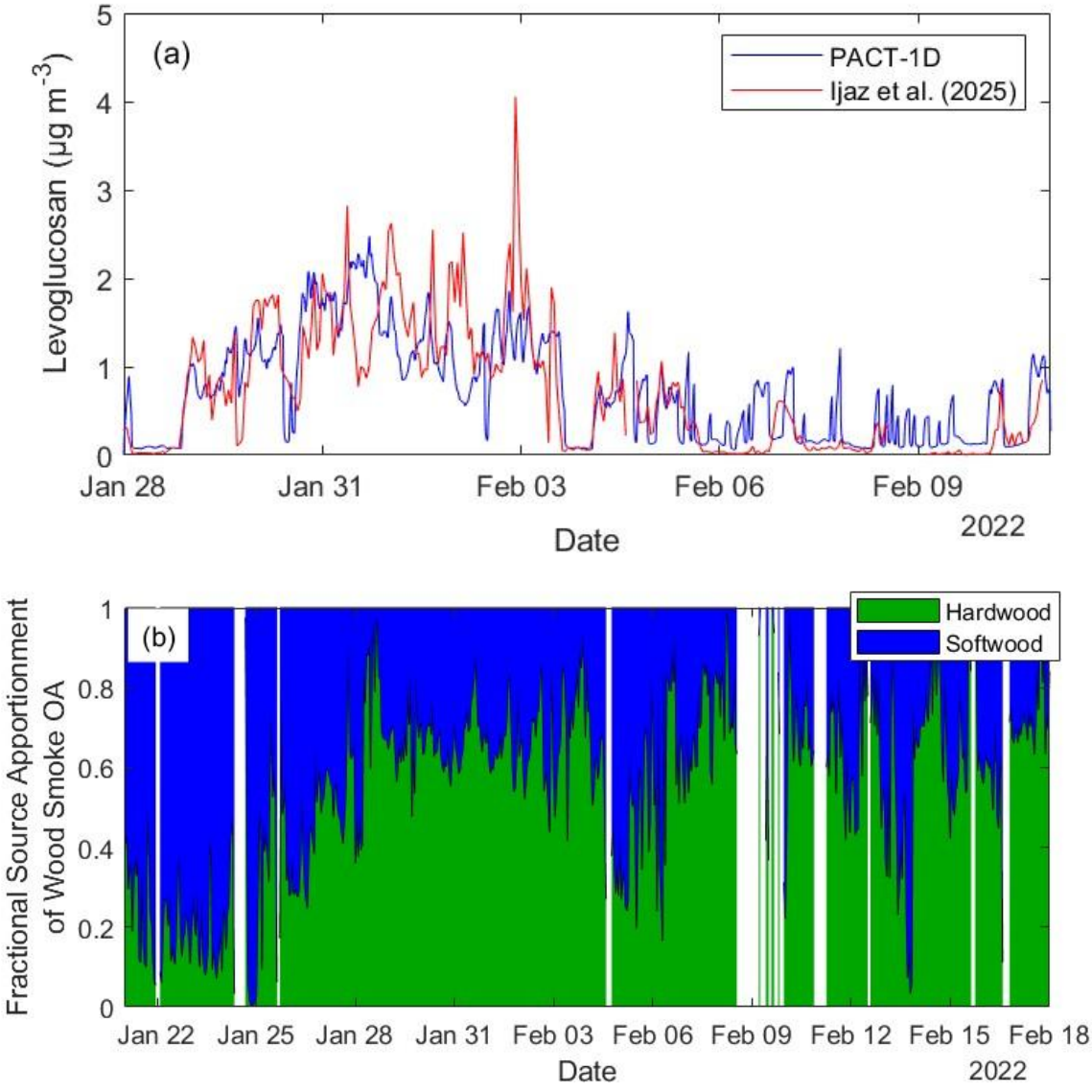

Figure S4. Atmospheric data for Fairbanks, Alaska during ALPACA: a) $PM_{2.5}$,[107] b) temperature,[107] and c) relative humidity. Relative humidity data was retrieved from NOAA's Environmental Research Division Data Access Program (ERDDAP) website for relative humidity data (https://erddap.sensors.ioos.us/erddap/tabledap/alaska-dot-rwis-255.html, last access: 18 October 2023, Airport Way @ Eielson Street).

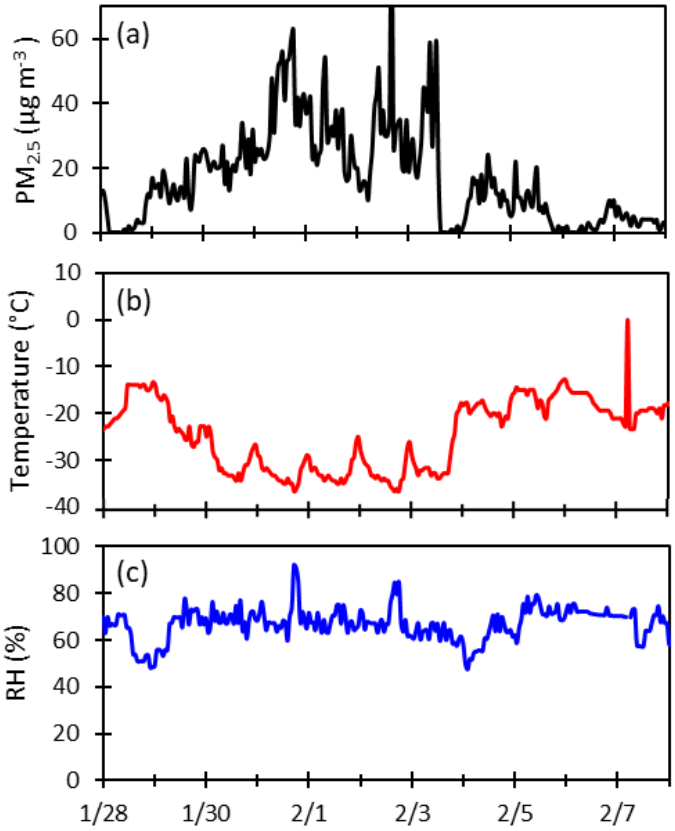

Figure S5. Modeled production rates of a) $^3C^*$, b) $^1O_2^*$, and c) $^{\bullet}OH$ in aqueous (solid blue lines) and organic (dashed green lines) particles. Rates are expressed relative to the air volume.

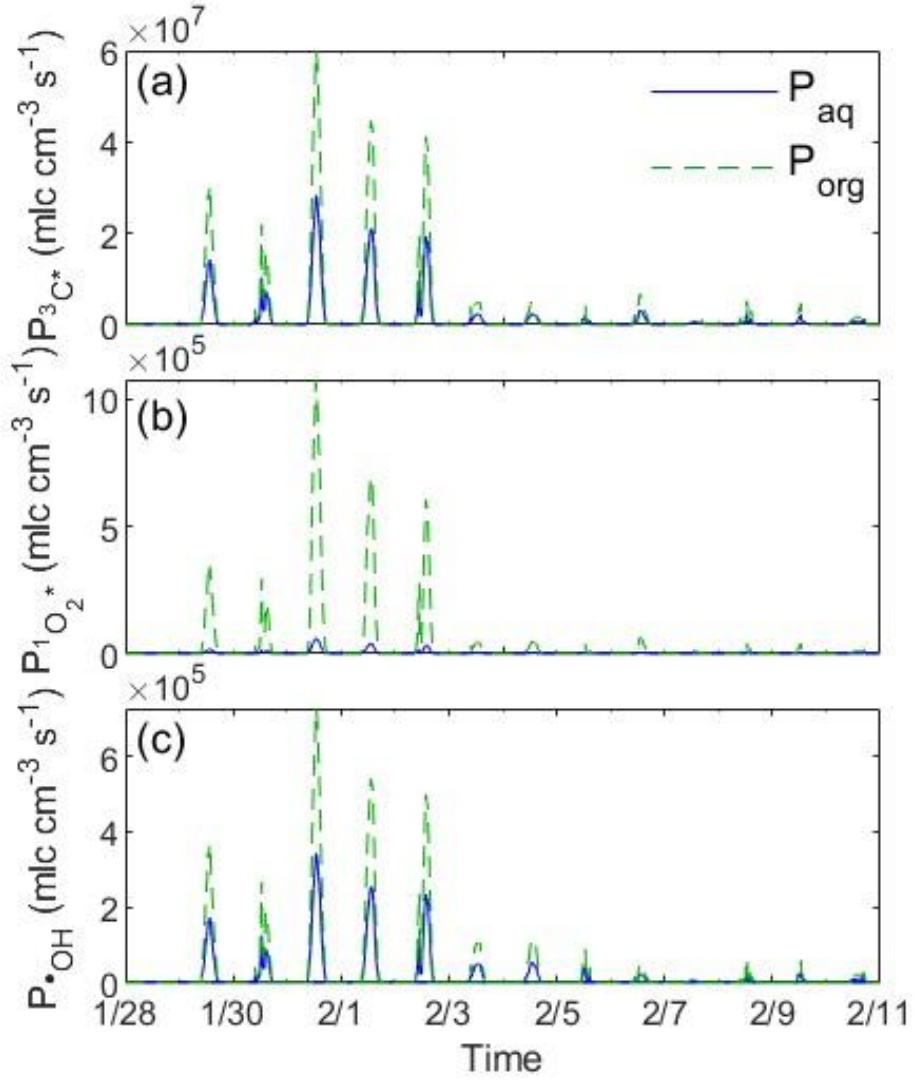

Figure S6. Comparison of singlet oxygen quantum yields. The continuous lines represent quantum yields determined from PACT-1D for aqueous (blue) and organic (red) particles, while the discontinuous lines represent measurements in dilute aqueous extracts of particle composites during ALPACA.[35]

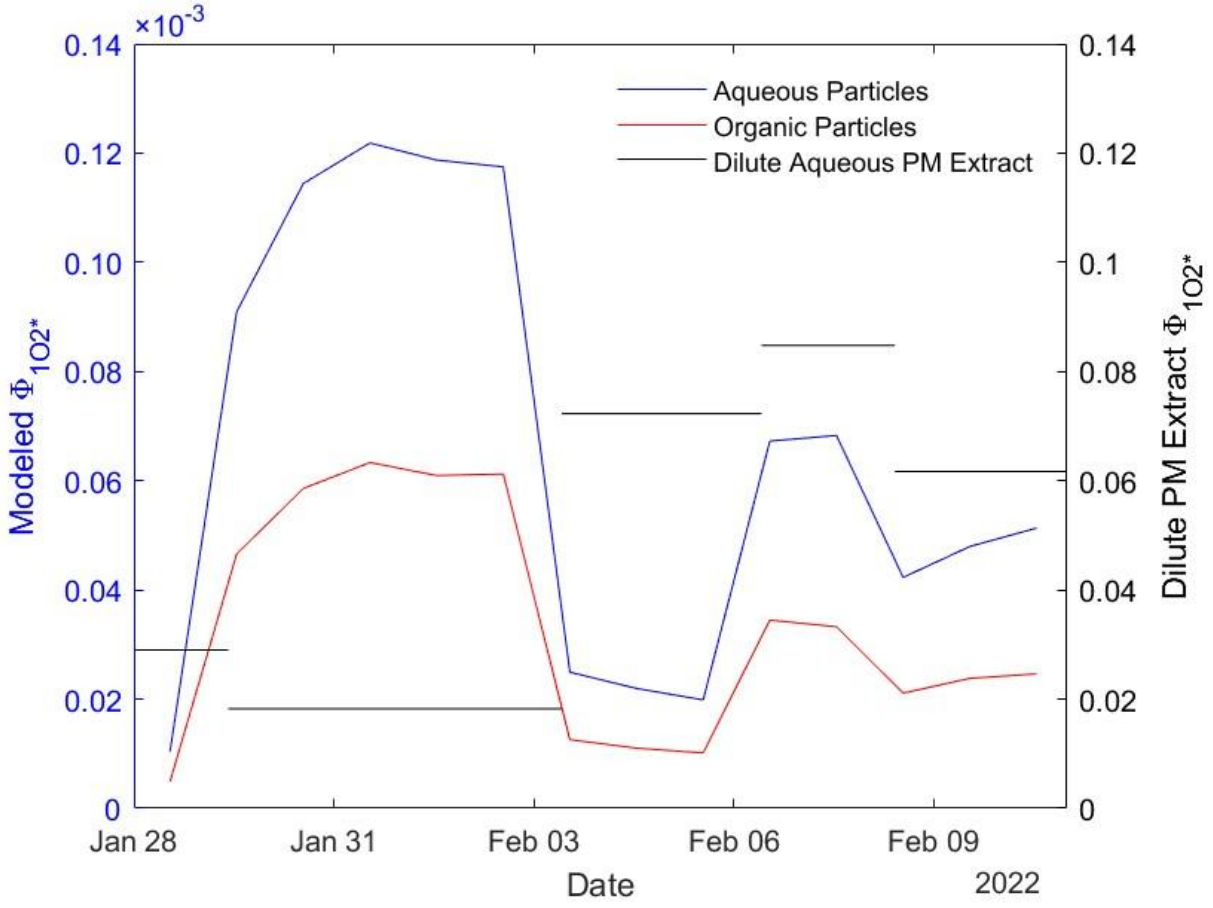

Figure S7. Concentrations of particle-phase a) $^{3}C^{*}$, b) $^{1}O_{2}^{*}$, and c) $^{\bullet}OH$ normalized to the air volume. Solid blue lines are results for aqueous particles and dashed green lines are concentrations in organic particles.

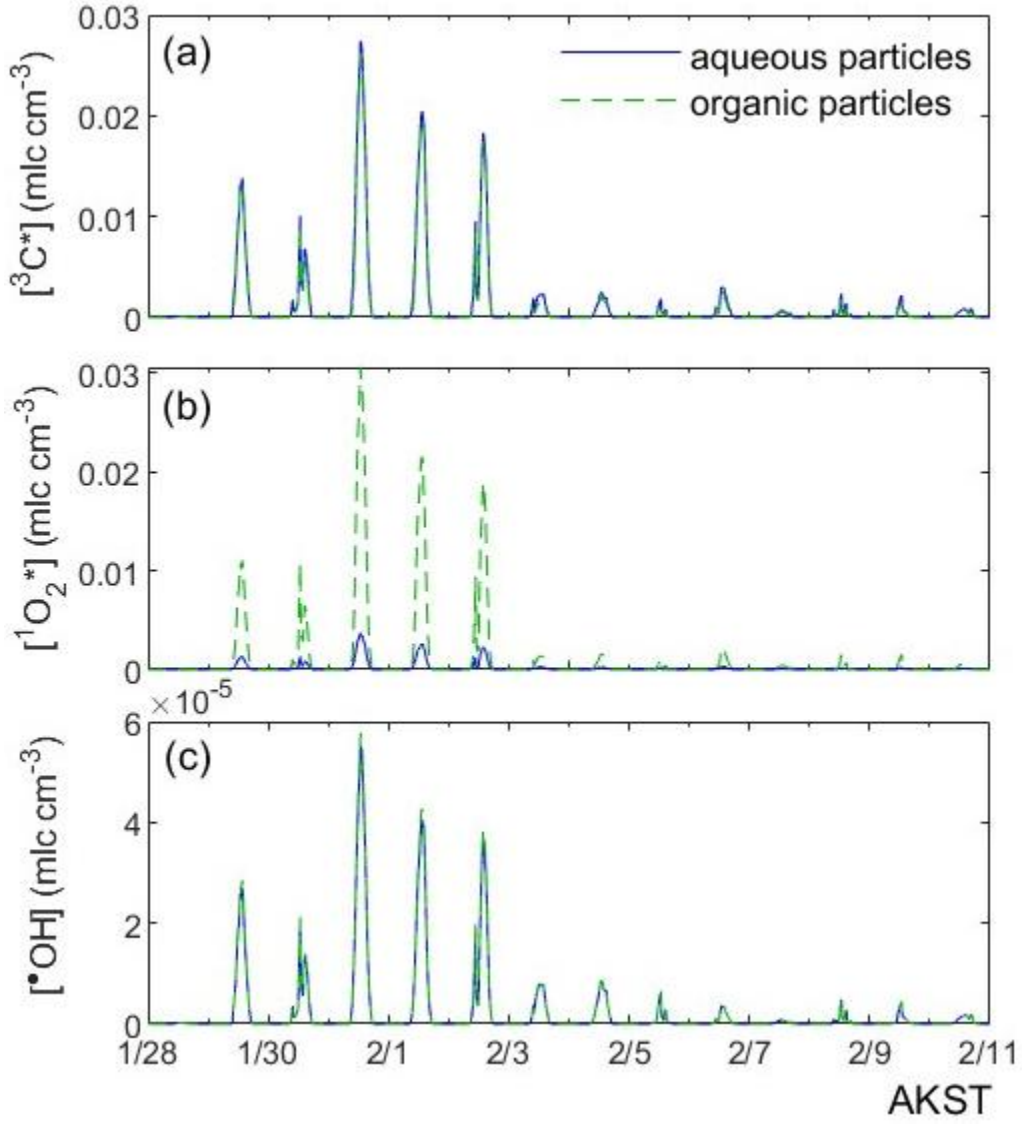

Figure S8. A comparison of the fraction of each modeled phenol in the particle phase (X_{PM}) on 1/31/2022 at 8:00 AM (Panel a) and 1:00 PM (Panel b). The pink 'x' marks represent the theoretical equilibrium X_{PM} (aqueous and organic) values at the given temperature and ALW and OA concentrations. The temperatures for the two times are -34 and -29 °C, respectively, while the OA concentrations are 18.7 and 22.6 μg m^{-3}, respectively. Panel (a) is the same plot as Figure 4b in the main text. Phenol names organized by C_i* are listed in Table S14.

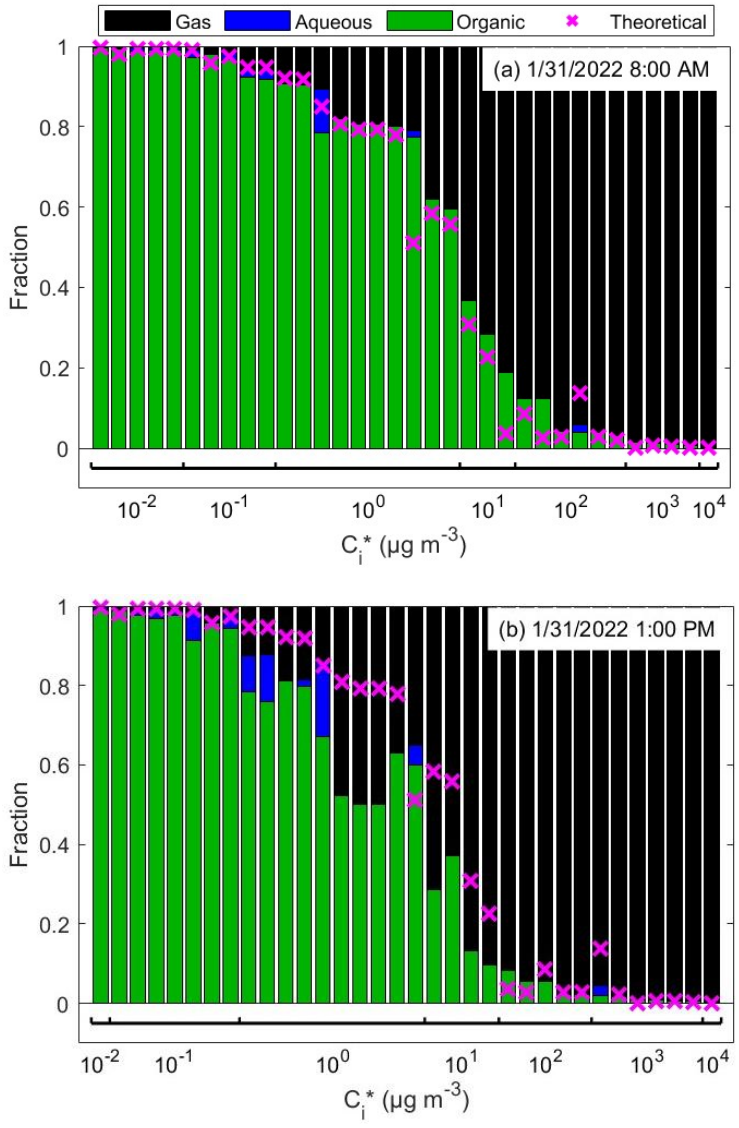

Figure S9. Model results for sensitivity test in which all phenols were emitted in the gas phase. Panels (a)-(c) show sensitivity test results that are parallel to the bas-case results in Figure 5 (where phenols were emitted in organic particles,) while panels (d)-(e) show equivalent information to the base case in Figure S8. (a) Stacked plot of the simulated organic aerosol (OA) concentrations formed in the gas phase (orgSOA, black – too small to be visible), aqueous particles (aqSOA, blue), and organic particles (orgSOA, green), in addition to simulated hydroxymethanesulfonate (HMS) reported by Kuhn et al. (yellow).[108] The right *y*-axis shows the total measured oxidized organic aerosol (OOA, magenta).[21] (b) Line plot of the ratio of simulated phenolic SOA to simulated levoglucosan (LG) concentrations (left *y*-axis, green) and the ratio of the measured OOA to measured LG (right *y*-axis, black).[21] (c) A stacked plot of the simulated fractional phenolic SOA formation rate from $^3C^*$ in organic particles (green), $^3C^*$ in aqueous particles (blue), and all other oxidants (white). (d-e) Fraction of each modeled phenol in the gas phase (black), aqueous particles (blue) and organic particles (green) on 1/31/2022 at 8:00 AM (panel d) and 1:00 PM (panel e). (f) Regression of total ArOH SOA formed in all phases in the sensitivity test, in which all ArOH are emitted in the gas phases, compared to the base case, in which all ArOH are emitted in organic particles.

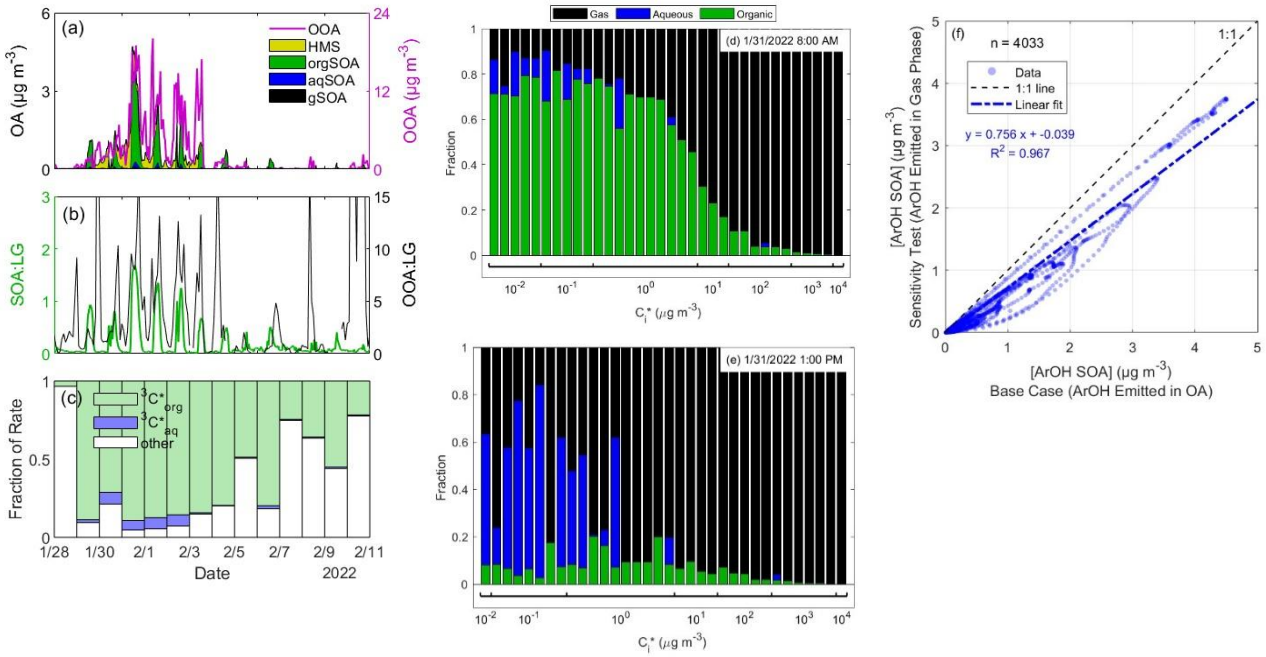

Figure S10. Total atmospheric chemical lifetimes of individual phenols from 1:00 AM to 1:00 PM on 1/31/2022. The lifetime for a given phenol was calculated as the total (gaseous + particulate) amount of phenol divided by the sum of the rates of loss in each phase. Each entry on the plot represents the statistical distribution of the lifetimes for the 34 modeled phenols: the top and bottom of each box are the first and third quartiles of the distribution, the midpoint line in the box is the median lifetime, the whiskers represent the entire range of points not considered outliers (quartile value ± 1.5 of the interquartile range), and individual points are outliers. In general, the total lifetime of a phenol increases as its fraction in the particle phase decreases. The magenta 'x' marks are the air-mass residence time at a given time of day.

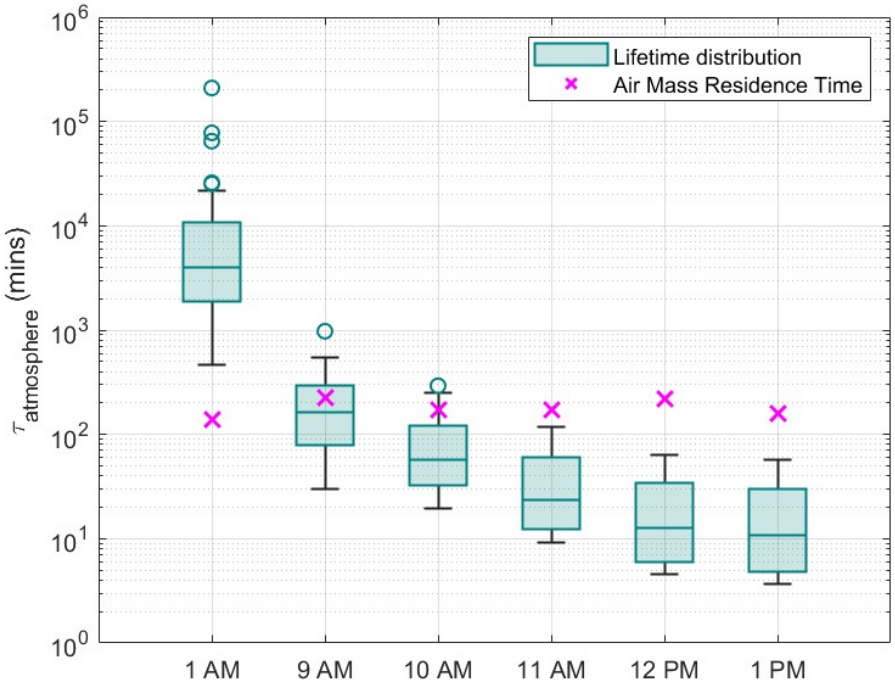

Figure S11. Lifetimes of individual phenols (calculated based on the total (gas + particulate) concentration of each phenol) due to chemical loss in (a) the gas phase (black), (b) aqueous particles (blue), or (c) organic particles (green) at 1:00 PM on 1/31/2022. The phenols are arranged by saturation concentration, C_i*. The magenta line depicts the PACT-1D predicted air mass residence time (2.7 hr) for this day and time. Figure S12 depicts the phenol lifetimes in each phase based on the concentration and rate of chemical loss in that phase. The phenol names organized by C_i* are listed in Table S14.

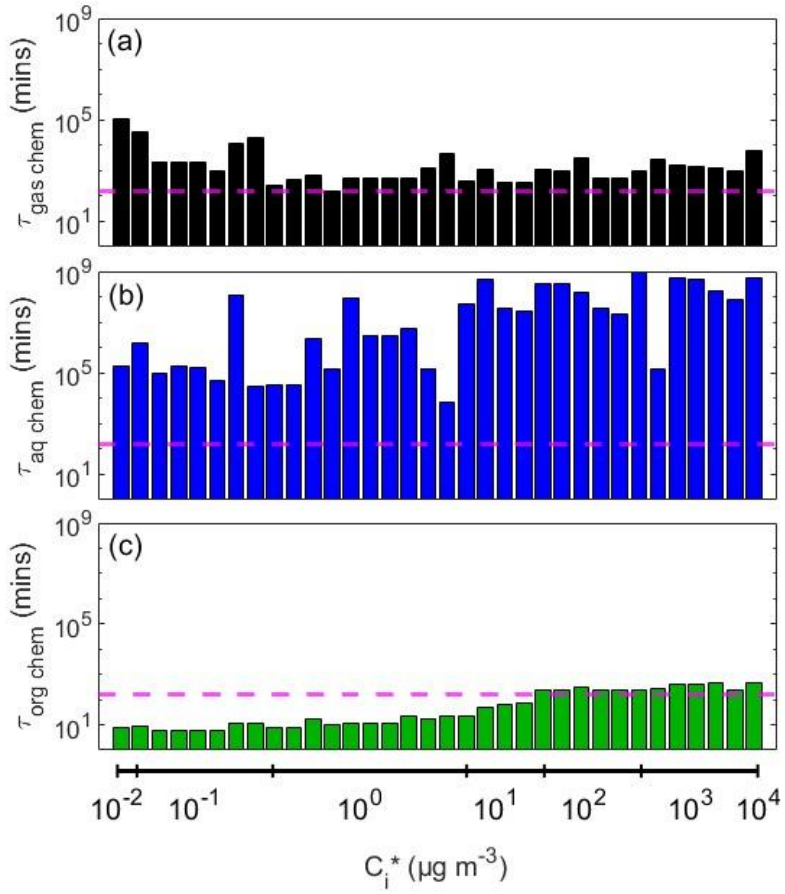

Figure S12. Lifetimes of individual phenols in a given phase, calculated as the concentration of ArOH in that phase divided by the rate of chemical loss in that phase, for the gas phase (black), aqueous particles (blue), and organic particles (green) at 1:00 PM on 1/31/2022. The lifetimes are grouped by C_i* at 1:00 PM on 1/31/2022. The magenta line depicts the PACT-1D predicted air mass residence time (2.7 hr) of the polluted layer at 1:00 PM on 1/31/2022. Figure S11 is a companion plot of ArOH lifetimes determined based on the total (gas + particulate) concentration of each phenol and rate of chemical loss in each phase. The phenol names organized by C_i* are listed in Table S14.

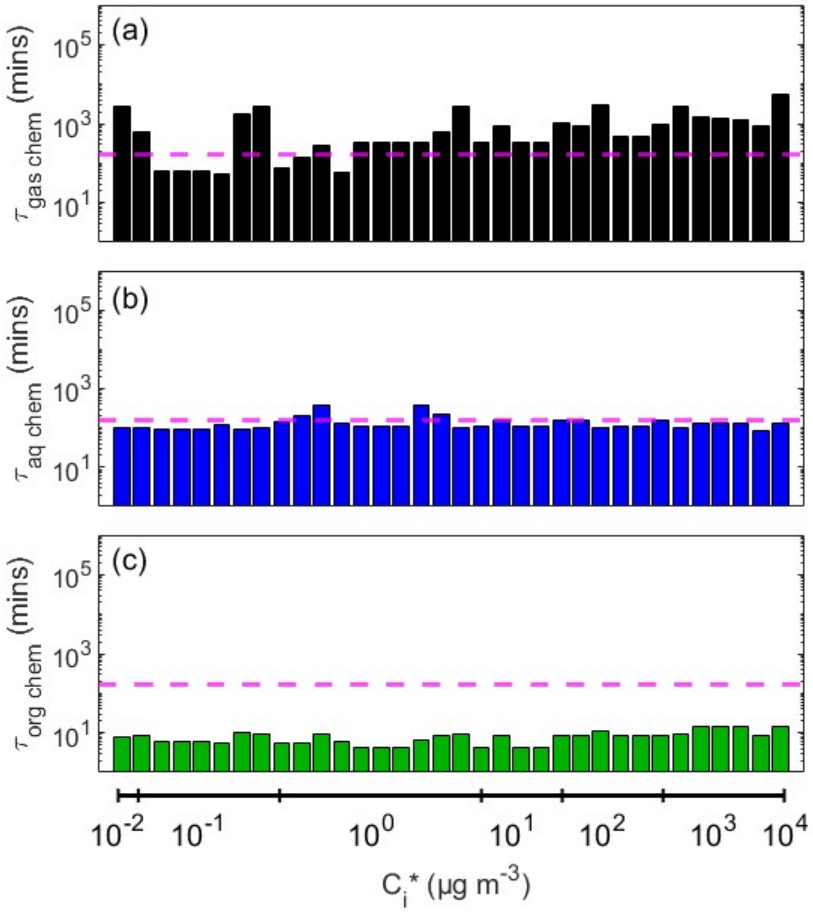

Figure S13. Distribution of ArOH lifetimes due to chemical loss in each phase between 1:00 AM and 1:00 PM on 1/31/2022. Panels (a)-(c) represent the lifetimes of phenols in a given phase (i.e., amount of phenol in a given phase divided by the chemical rate of loss in that phase), while (d)-(e) represent the total lifetime of phenol calculated as the total (gas + particulate) ArOH concentration divided by the rate of chemical loss in a given phase. The magenta 'x' marks the air mass residence time of the polluted surface later predicted by PACT-1D at each time point.

(a-c) Lifetimes with respect to phenol concentration in each phase.

(d-f) Lifetimes with respect to the total phenol concentration.

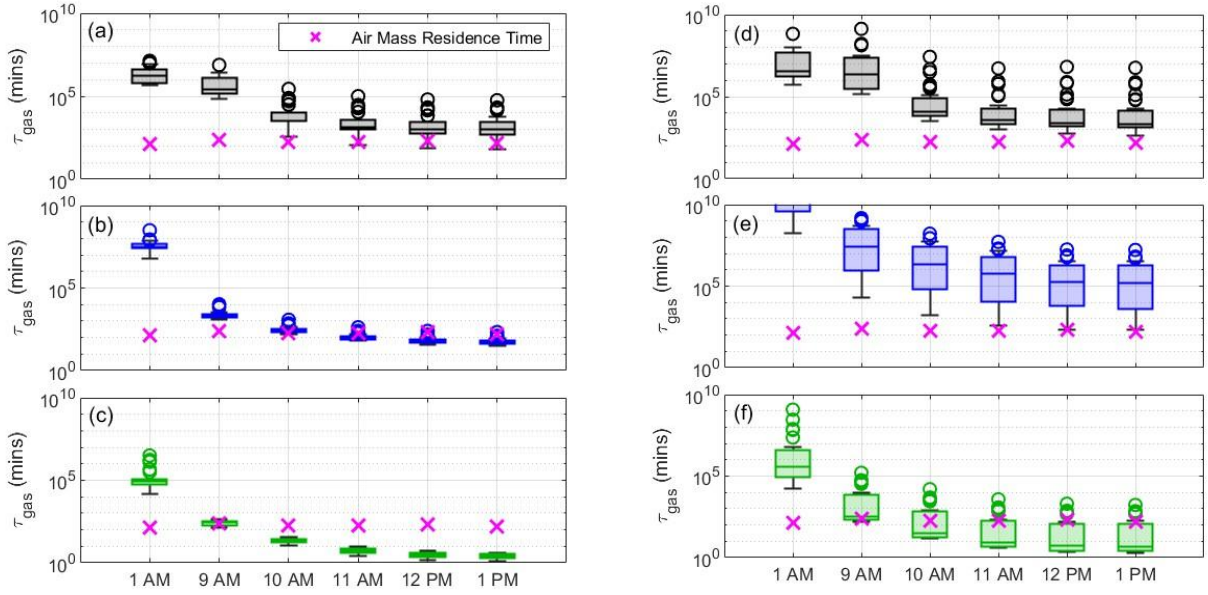

Figure S14. Correlogram of factors of each phenol showing their influence on phenol-specific rates of ArOH SOA formation at 1:00 PM on 1/31/2022. For example, the rate of phenolic SOA formation has a correlation coefficient (R^2) of 0.9 with respect to the emissions rate across the 34 modeled phenols. Key to factors: SOA_{tot} = total phenolic SOA concentration (μg m^{-3}); $ArOH_{org}$ = concentration of each phenol in organic particles (μg m^{-3}); X_{org} = fraction of each ArOH in organic particles; C_i* = the saturation concentration of each ArOH species at 1:00 PM on 1/31/2022 (-29 °C, μg m^{-3}); $ArOH_{tot}$ = total ArOH concentration (μg m^{-3}); and Emissions = the emissions rate of each ArOH (mlc cm^{-3} s^{-1}).

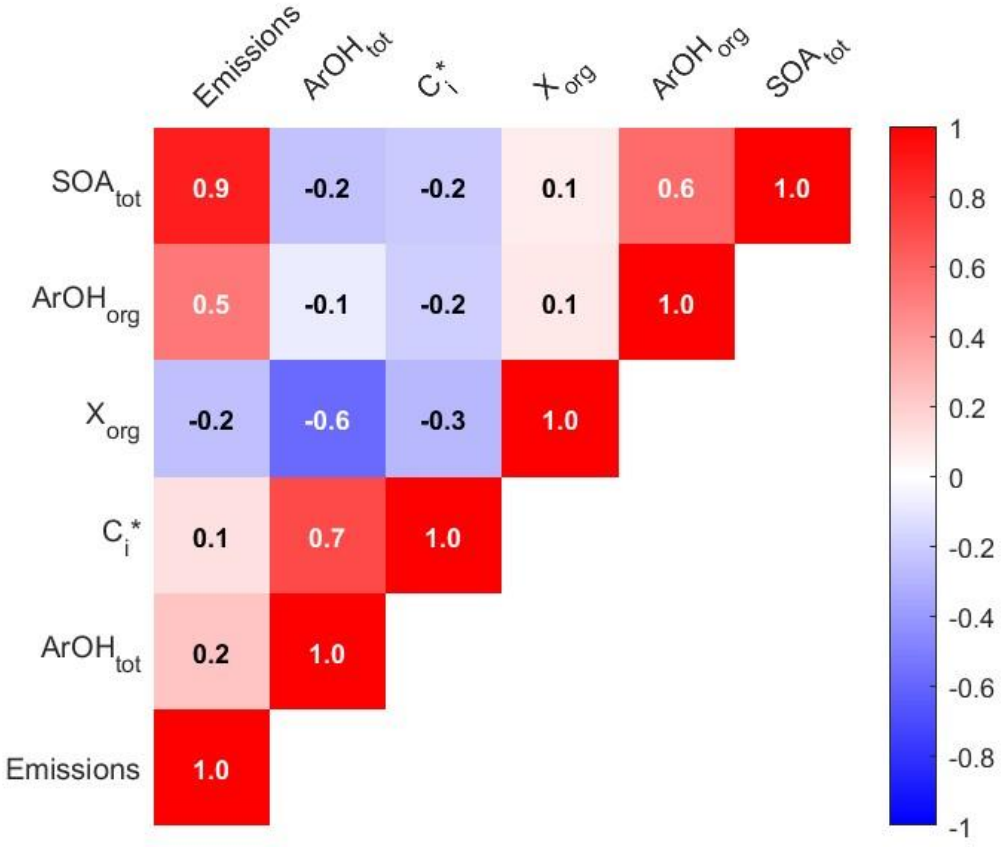

Figure S15. (a) $^1O_2$* phosphorescence kinetic traces produced from Rose Bengal in D_2O with increasing concentrations of woodsmoke extract. Concentrations are mM-organic C. (b) Calculated $^1O_2$* pseudo-first-order decay rate constants (*k'*) for solutions with increasing woodsmoke extract concentrations. The line represents a linear fit (R^2 = 0.98) with the slope representing the quenching rate constant between $^1O_2$* and woodsmoke extract, yielding $k_{1O2*+DOC}$ = 1.6(±0.1)×10^6 L mol-C^{-1} s^{-1} with associated standard deviation of the slope.

(a)

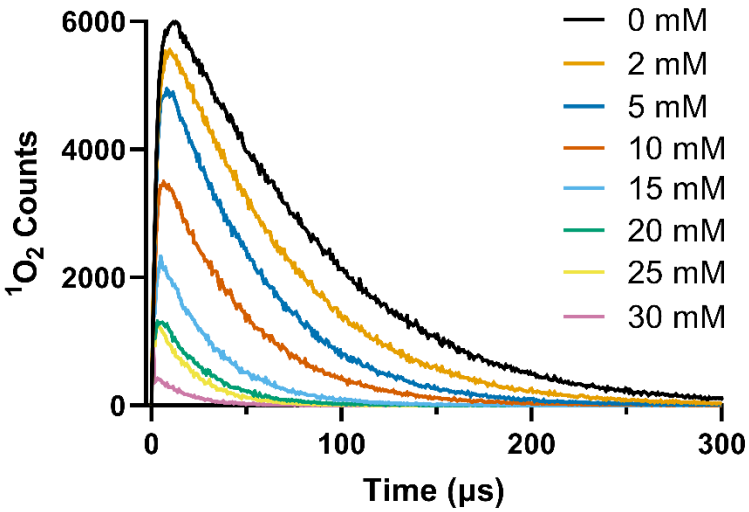

(b)

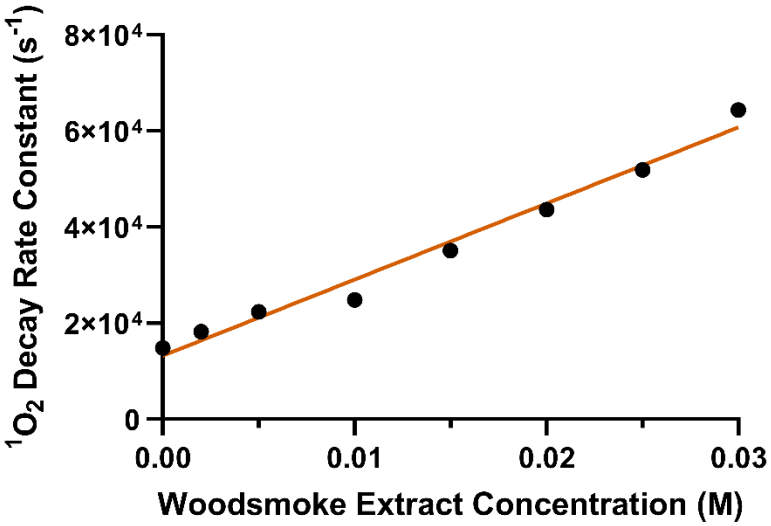

Figure S16. Regressions of modeled versus measured (a) total phenol concentrations and (b) particle-phase phenol concentrations for 16 phenols measured with an SV-TAG during ALPACA.[24] The measurements were collected at random intervals throughout the day. Only model results with corresponding timestamps are included in these regressions. The points are color coded to reflect the time of day (i.e., yellow corresponds to noon and dark purple corresponds to midnight).

(a) Total phenol concentrations

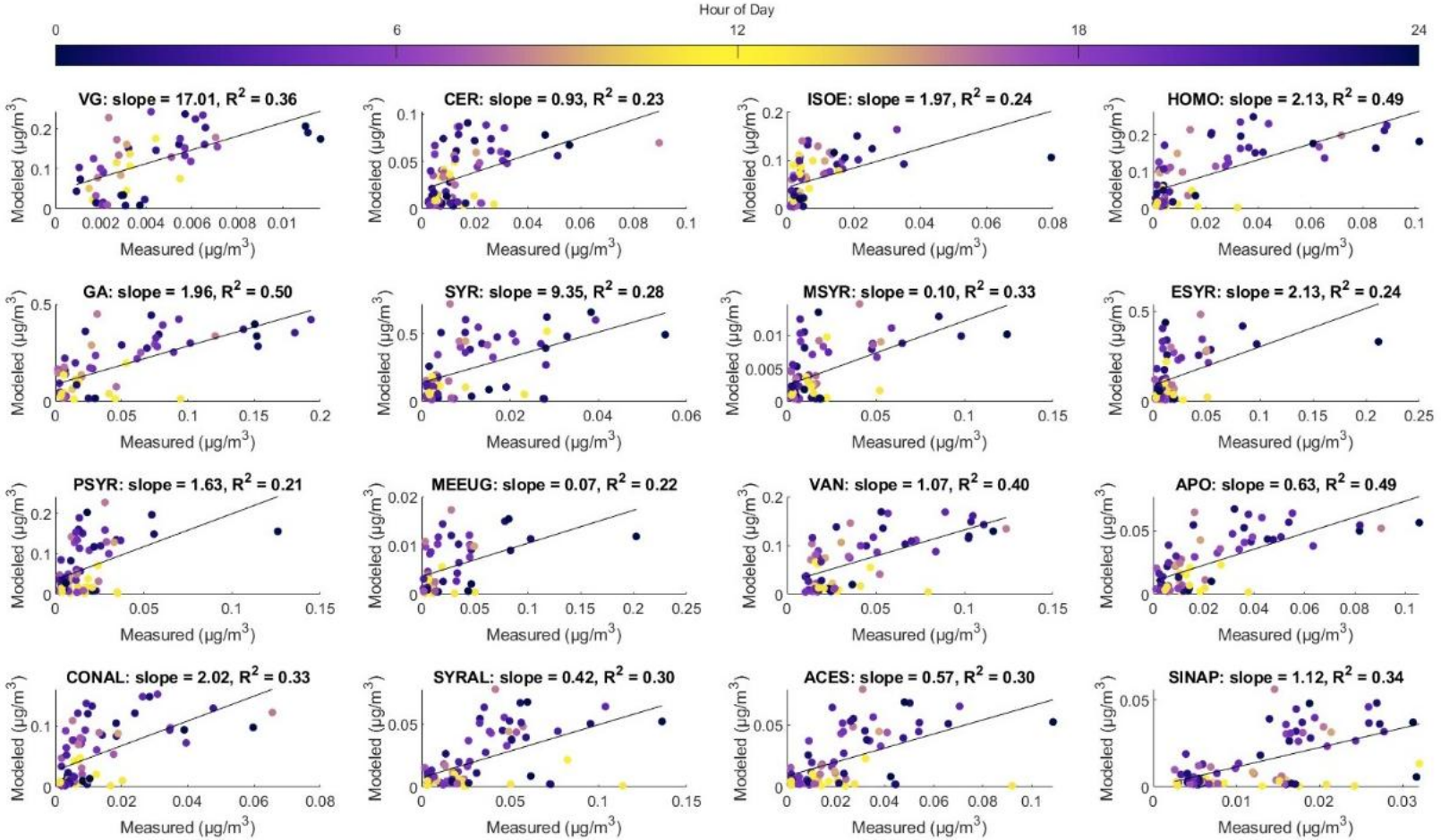

(b) Particle-phase phenol concentrations

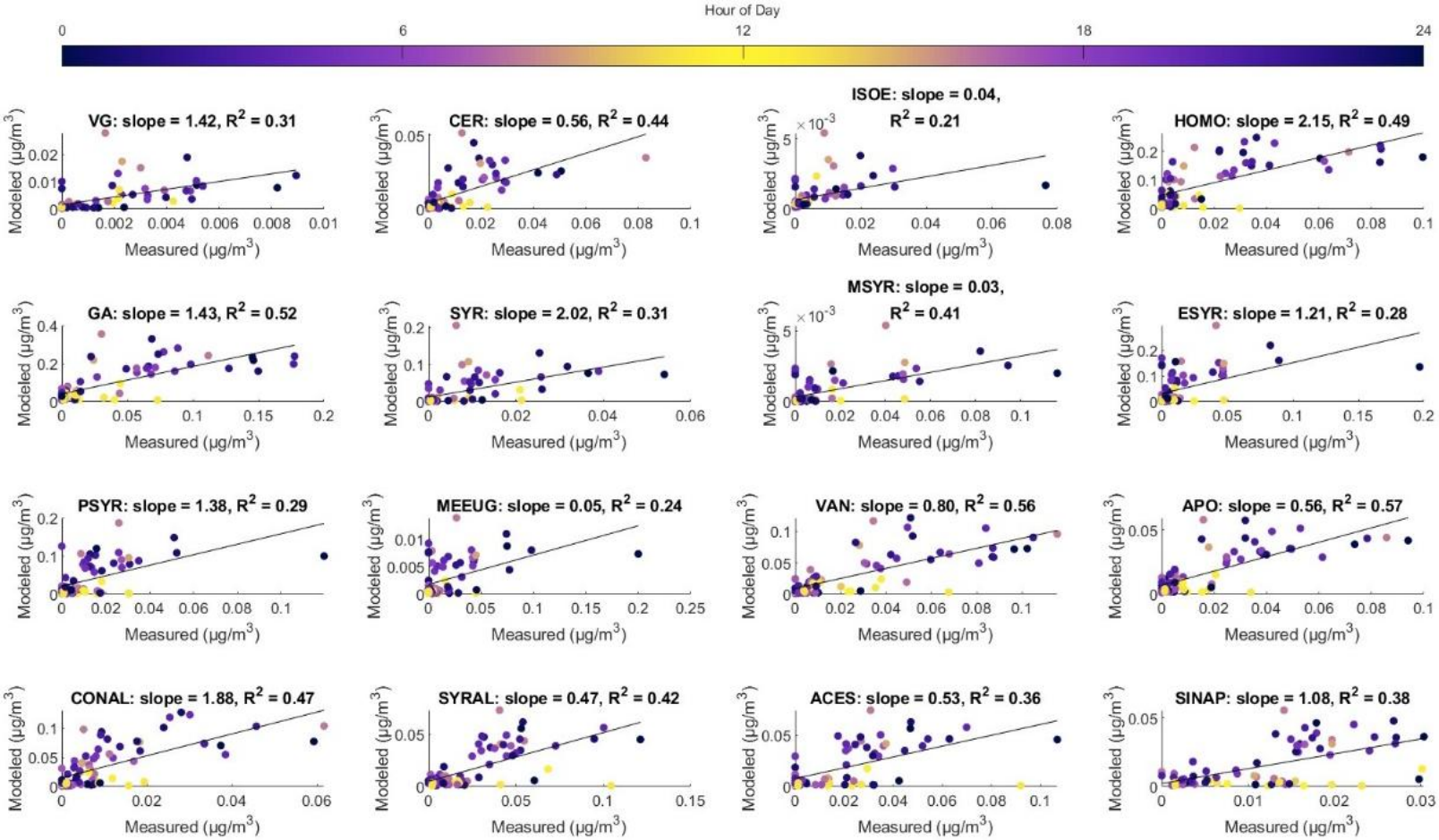

REFERENCES

(1) Schauer, J. J.; Kleeman, M. J.; Cass, G. R.; Simoneit, B. R. T. Measurement of Emissions from Air Pollution Sources. 3. C1-C29 Organic Compounds from Fireplace Combustion of Wood. *Environ. Sci. Technol.* **2001**, *35* (9), 1716–1728. https://doi.org/10.1021/es001331e.

(2) Ijaz, A.; Temime-Roussel, B.; Kammer, J.; Mao, J.; Simpson, W.; Law, K. S.; D'Anna, B. In Situ Measurements of Gas-Particle Partitioning of Organic Compounds in Fairbanks. *Faraday Discuss.* **2024**. https://doi.org/10.1039/d4fd00175c.

(3) Seinfeld, J. H.; Pandis, S. N. *Atmospheric Chemistry and Physics: From Air Pollution to Climate Change*, 3rd ed.; Wiley, **2016**.

(4) Fuchs, N. A.; Sutugin, A. G. High-Dispersed Aerosols. *Topics in Current Aerosol Research* **1971**, 1. https://doi.org/10.1016/B978-0-08-016674-2.50006-6.

(5) Tuite, K.; Thomas, J. L.; Veres, P. R.; Roberts, J. M.; Stevens, P. S.; Griffith, S. M.; Dusanter, S.; Flynn, J. H.; Ahmed, S.; Emmons, L.; Kim, S. W.; Washenfelder, R.; Young, C.; Tsai, C.; Pikelnaya, O.; Stutz, J. Quantifying Nitrous Acid Formation Mechanisms Using Measured Vertical Profiles During the CalNex 2010 Campaign and 1D Column Modeling. *Journal of Geophysical Research: Atmospheres* **2021**, *126* (13). https://doi.org/10.1029/2021JD034689.

(6) Ahmed, S.; Thomas, J. L.; Tuite, K.; Stutz, J.; Flocke, F.; Orlando, J. J.; Hornbrook, R. S.; Apel, E. C.; Emmons, L. K.; Helmig, D.; Boylan, P.; Huey, L. G.; Hall, S. R.; Ullmann, K.; Cantrell, C. A.; Fried, A. The Role of Snow in Controlling Halogen Chemistry and Boundary Layer Oxidation During Arctic Spring: A 1D Modeling Case Study. *Journal of Geophysical Research: Atmospheres* **2022**, *127* (5). https://doi.org/10.1029/2021JD036140.

(7) Cesler-Maloney, M.; Simpson, W.; Kuhn, J.; Stutz, J.; Thomas, J.; Roberts, T.; Huff, D.; Cooperdock, S. Shallow Boundary Layer Heights Controlled by the Surface-Based Temperature Inversion Strength Are Responsible for Trapping Home Heating Emissions near the Ground Level in Fairbanks, Alaska. **2024**. https://doi.org/10.5194/egusphere-2023-3082.

(8) Kuhn, J.; Stutz, J.; Bartels-Rausch, T.; Thomas, J. L.; Cesler-Maloney, M.; Simpson, W.; Dibb, J. E.; Heinlein, L. M. D.; Anastasio, C. The Interplay between Snow and Polluted Air Masses in Cold Urban Environments. *Faraday Discuss.* **2024**. https://doi.org/10.1039/D4FD00176A.

(9) Sander, R. Compilation of Henry's Law Constants (Version 5.0.0) for Water as Solvent. *Atmos. Chem. Phys.* **2023**, *23* (19), 10901–12440. https://doi.org/10.5194/acp-23-10901-2023.

(10) Muller, B.; Heal, M. R. Mass Accommodation Coefficients of Phenol, 2-Nitrophenol, and 3-Methylphenol over the Temperature Range 278-298 K. *J. Phys. Chem. A* **2002**, *106*, 5120–5127. https://doi.org/10.1021/jp013559.

(11) Diévart, P.; Allou, L.; Louis, F.; Le Calvé, S. Tropospheric Multiphase Chemistry of 2,5- and 2,6-Dimethylphenols: Determination of the Mass Accommodation Coefficients and the Henry's Law Constants. *Physical Chemistry Chemical Physics* **2006**, *8* (14), 1714–1723. https://doi.org/10.1039/b516193b.

(12) Krechmer, J. E.; Day, D. A.; Ziemann, P. J.; Jimenez, J. L. Direct Measurements of Gas/Particle Partitioning and Mass Accommodation Coefficients in Environmental Chambers. *Environ. Sci. Technol.* **2017**, *51* (20), 11867–11875. https://doi.org/10.1021/acs.est.7b02144.

(13) Julin, J.; Winkler, P. M.; Donahue, N. M.; Wagner, P. E.; Riipinen, I. Near-Unity Mass Accommodation Coefficient of Organic Molecules of Varying Structure. *Environ. Sci. Technol.* **2014**, *48* (20), 12083–12089. https://doi.org/10.1021/es501816h.

(14) Sinha, A.; Saleh, R.; Robinson, E. S.; Ahern, A. T.; Tkacik, D. S.; Presto, A. A.; Sullivan, R. C.; Robinson, A. L.; Donahue, N. M. Mass Accommodation Coefficients of Fresh and Aged Biomass-Burning Emissions. *Aerosol Science and Technology* **2018**, *52* (3), 300–309. https://doi.org/10.1080/02786826.2017.1413488.

(15) McFall, A. S.; Johnson, A. W.; Anastasio, C. Air-Water Partitioning of Biomass-Burning Phenols and the Effects of Temperature and Salinity. *Environ. Sci. Technol.* **2020**, *54* (7), 3823–3830. https://doi.org/10.1021/acs.est.9b06443.

(16) Campbell, J.; Battaglia Jr, M.; Dingilian, K.; Cesler-Maloney, M.; Simpson, W.; Robinson, E.; DeCarlo, P.; Temime-Roussel, B.; D'Anna, B.; Holen, A.; Wu, J.; Pratt, K.; Dibb, J.; Nenes, A.; Weber, R.; Mao, J. Enhanced Aqueous Formation and Neutralization of Fine Atmospheric Particles Driven by Extreme Cold. *Arctic Data Center [data set]* **2024**. https://doi.org/10.18739/A2G73757K.

(17) Campbell, J. R.; Battaglia Jr, M.; Dingilian, K. K.; Cesler-Maloney, M.; Simpson, W. R.; Robinson, E. S.; DeCarlo, P. F.; Temime-Roussel, B.; Holen, A. L.; Wu, J.; Pratt, K. A.; Dibb, J. E.; Nenes, A.; Weber, R. J.; Mao, J. Enhanced Aqueous Formation and Neutralization of Fine Atmospheric Particles Driven by Extreme Cold. *Sci. Adv* **2024**, *10*, 4373. https://doi.org/10.1126/sciadv.ado4373.

(18) Robinson, E. S.; Battaglia, M.; Campbell, J. R.; Cesler-Maloney, M.; Simpson, W.; Mao, J.; Weber, R. J.; DeCarlo, P. F. Multi-Year, High-Time Resolution Aerosol Chemical Composition and Mass Measurements from Fairbanks, Alaska. *Environmental Science: Atmospheres* **2024**, *4* (6), 685–698. https://doi.org/10.1039/d4ea00008k.

(19) Holen, A. L.; Wu, J.; Forshee, L.; Dingilian, K. K.; Selimovic, V.; Battaglia, M. A.; Robinson, E. S.; Cysneiros de Carvalho, K.; Ketcherside, D. T.; Campbell, J. R.; Moon, A.; Alexander, B.; Simpson, W. R.; Mao, J.; Hu, L.; Williams, B. J.; DeCarlo, P. F.; Weber, R. J.; Pratt, K. A. Quantifying Contributions of Sulfate, Hydroxymethanesulfonate, and Additional S(IV) Compounds to Wintertime Aerosol Particles. *ACS ES&T Air* **2025**, *2* (11), 2588–2602. https://doi.org/10.1021/acsestair.5c00232.

(20) Moon, A.; Jongebloed, U.; Dingilian, K. K.; Schauer, A. J.; Chan, Y.-C.; Cesler-Maloney, M.; Simpson, W. R.; Weber, R. J.; Tsiang, L.; Yazbeck, F.; Zhai, S.; Wedum, A.; Turner, A. J.; Albertin, S.; Bekki, S.; Savarino, J.; Gribanov, K.; Pratt, K. A.; Costa, E. J.; Anastasio, C.; Sunday, M. O.; Heinlein, L. M. D.; Mao, J.; Alexander, B. Primary Sulfate Is the Dominant Source of Particulate Sulfate during Winter in Fairbanks, Alaska. *ES&T Air* **2024**, *1*, 139–149. https://doi.org/10.1021/acsestair.3c00023.

(21) Ijaz, A.; Temime-Roussel, B.; Chazeau, B.; Albertin, S.; Arnold, S. R.; Barrett, B.; Bekki, S.; Brett, N.; Cesler-Maloney, M.; Dieudonne, E.; Dingilian, K. K.; Fochesatto, J. G.; Mao, J.; Moon, A.; Savarino, J.; Simpson, W.; Weber, R. J.; Law, K. S.; D'Anna, B. Complementary Aerosol Mass Spectrometry Elucidates Sources of Wintertime Sub-Micron Particle Pollution in Fairbanks, Alaska, during ALPACA 2022 . *Atmos. Chem. Phys.* **2025**, *25*, 11789–11811. https://doi.org/10.5194/acp-25-11789-2025.

(22) Pankow, J. F. An Absorption Model of Gas/Particle Partitioning of Organic Compounds in the Atmosphere. *Atmos. Environ.* **1994**, *28* (2), 185–188.https://doi.org/10.1016/1352-2310(94)90093-0.

(23) Pankow, J. F. An Absorption Model of Gas/Particle Partitioning Involved in the Formation of Secondary Organic Aerosol. *Atmos. Environ.* **1994**, *28* (2), 189–193. https://doi.org/10.1016/1352-2310(94)90094-9.

(24) Cysneiros De Carvalho, K. Investigation of Volatility, Composition, and Gas-Particle Phase Investigation of Volatility, Composition, and Gas-Particle Phase Partitioning of Atmospheric Organic Compounds through Novel Partitioning of Atmospheric Organic Compounds through Novel Instrumentation and Techniques Instrumentation and Techniques, Washington University in St. Louis, **2024**. https://openscholarship.wustl.edu/eng_etds/1057.

(25) Donahue, N. M.; Robinson, A. L.; Stanier, C. O.; Pandis, S. N. Coupled Partitioning, Dilution, and Chemical Aging of Semivolatile Organics. *Environ. Sci. Technol.* **2006**, *40* (8), 2635–2643. https://doi.org/10.1021/es052297c.

(26) Pankow, J. F.; Seinfeld, J. H.; Asher, W. E.; Erdakos, G. B. Modeling the Formation of Secondary Organic Aerosol. 1. Application of Theoretical Principles to Measurements Obtained in the α-Pinene/, β-Pinene/, Sabinene/, Δ3-Carene/, and Cyclohexene/Ozone Systems. *Environ. Sci. Technol.* **2001**, *35* (6), 1164–1172. https://doi.org/10.1021/es001321d.

(27) Kuwata, M.; Zorn, S. R.; Martin, S. T. Using Elemental Ratios to Predict the Density of Organic Material Composed of Carbon, Hydrogen, and Oxygen. *Environ. Sci. Technol.* **2012**, *46* (2), 787–794. https://doi.org/10.1021/es202525q.

(28) Atwi, K.; Cheng, Z.; El Hajj, O.; Perrie, C.; Saleh, R. A Dominant Contribution to Light Absorption by Methanol-Insoluble Brown Carbon Produced in the Combustion of Biomass Fuels Typically Consumed in Wildland Fires in the United States. *Environmental Science: Atmospheres* **2022**, *2* (2), 182–191. https://doi.org/10.1039/d1ea00065a.

(29) Ma, L.; Worland, R.; Jiang, W.; Niedek, C.; Guzman, C.; Bein, K. J.; Zhang, Q.; Anastasio, C. Predicting Photooxidant Concentrations in Aerosol Liquid Water Based on Laboratory Extracts of Ambient Particles. *Atmos. Chem. Phys.* **2023**, *23*, 8805–8821. https://doi.org/10.5194/acp-23-8805-2023.

(30) Ma, L.; Worland, R.; Heinlein, L.; Guzman, C.; Jiang, W.; Niedek, C.; Bein, K. J.; Zhang, Q.; Anastasio, C. Seasonal Variations in Photooxidant Formation and Light Absorption in Aqueous Extracts of Ambient Particles. *Atmos. Chem. Phys.* **2024**, *24*, 1–21. https://doi.org/10.5194/acp-24-1-2024.

(31) Kaur, R.; Labins, J. R.; Helbock, S. S.; Jiang, W.; Bein, K. J.; Zhang, Q.; Anastasio, C. Photooxidants from Brown Carbon and Other Chromophores in Illuminated Particle Extracts. *Atmos. Chem. Phys.* **2019**, *19* (9), 6579–6594. https://doi.org/10.5194/acp-19-6579-2019.

(32) Gorman, A. A.; Hamblett, I.; Lambert, C.; Spencer, B.; Standen, M. C. Identification of Both Preequilibrium and Diffusion Limits for Reaction of Singlet Oxygen, O2(1Ag), with Both Physical and Chemical Quenchers: Variable-Temperature, Time-Resolved Infrared Luminescence Studies. *J. Am. Chem. Soc.* **1988**, *110*, 8053–8059. https://doi.org/0002-7863/88/1510-8053S01.50/0.

(33) Wilkinson, F.; Helman, W. P.; Ross, A. B. Rate Constants for the Decay and Reactions of the Lowest Electronically Excited Singlet State of Molecular Oxygen in Solution. An Expanded and Revised Compilation. *J. Phys. Chem. Ref. Data* **1995**, *24* (2), 663–677. https://doi.org/10.1063/1.555965.

(34) Cory, R. M.; Cotner, J. B.; Mcneill, K. Quantifying Interactions between Singlet Oxygen and Aquatic Fulvic Acids. *Environ. Sci. Technol.* **2009**, *43* (3), 718–723. https://doi.org/10.1021/es801847g.

(35) Heinlein, L. M. D.; He, J.; Sunday, M. O.; Guo, F.; Campbell, J.; Moon, A.; Kapur, S.; Fang, T.; Edwards, K.; Cesler-Maloney, M.; Burns, A. J.; Dibb, J.; Simpson, W.; Shiraiwa, M.; Alexander, B.; Mao, J.; Flynn III, J. H.; Stutz, J.; Anastasio, C. Surprisingly Robust Photochemistry in Subarctic Particles During Winter: Evidence from Photooxidants. *Atmos. Chem. Phys.* **2025**, *25*, 9561–9581. https://doi.org/10.5194/acp-25-9561-2025.

(36) Smith, J. D.; Kinney, H.; Anastasio, C. Phenolic Carbonyls Undergo Rapid Aqueous Photodegradation to Form Low-Volatility, Light-Absorbing Products. *Atmos. Environ.* **2016**, *126*, 36–44. https://doi.org/10.1016/j.atmosenv.2015.11.035.

(37) Corral Arroyo, P.; David, G.; Alpert, P. A.; Parmentier, E. A.; Ammann, M.; Signorell, R. Amplification of Light within Aerosol Particles Accelerates In-Particle Photochemistry. *Science (1979).* **2022**, *376* (6590), 293–296. https://doi.org/10.1126/science.abm7915.

(38) Li, J.; Chen, Q.; Guan, D. Insights into the Triplet Photochemistry of Atmospheric Aerosol and Subfractions Isolated with Different Polarity. *Atmos. Environ.* **2022**, *290*. https://doi.org/10.1016/j.atmosenv.2022.119375.

(39) Sardena, C.; Gemmell, K. J.; Zhang, J.; Jiang, F.; Saathoff, H.; Bell, D. M.; Borduas-Dedekind, N. Singlet Oxygen and Triplet Excited State Organics Produced by Primary Biomass Burning Organic Aerosol from Wood, Dung, Straw, and Plastic Fuels: Role of Solvent-Dependent Photochemistry. *ACS ES&T Air* **2026**. https://doi.org/10.1021/acsestair.5c00462.

(40) McNeill, K.; Canonica, S. Triplet State Dissolved Organic Matter in Aquatic Photochemistry: Reaction Mechanisms, Substrate Scope, and Photophysical Properties. *Environ. Sci. Process. Impacts* **2016**, *18* (11), 1381–1399. https://doi.org/10.1039/c6em00408c.

(41) Miyamoto, H.; Yampolski, Y.; Young, C. L. IUPAC-NIST Solubility Data Series. 103. Oxygen and Ozone in Water, Aqueous Solutions, and Organic Liquids (Supplement to Solubility Data Series Volume 7). *J. Phys. Chem. Ref. Data* **2014**, *43* (3). https://doi.org/10.1063/1.4883876.

(42) Kiland, K. J.; Mahrt, F.; Peng, L.; Nikkho, S.; Zaks, J.; Crescenzo, G. V.; Bertram, A. K. Viscosity, Glass Formation, and Mixing Times within Secondary Organic Aerosol from Biomass Burning Phenolics. *ACS Earth Space Chem.* **2023**, *7*, 1388–1400. https://doi.org/10.1021/acsearthspacechem.3c00039.

(43) Reid, J. P.; Bertram, A. K.; Topping, D. O.; Laskin, A.; Martin, S. T.; Petters, M. D.; Pope, F. D.; Rovelli, G. The Viscosity of Atmospherically Relevant Organic Particles. *Nat. Commun.* **2018**, *9* (1). https://doi.org/10.1038/s41467-018-03027-z.

(44) DeRieux, W. S. W.; Li, Y.; Lin, P.; Laskin, J.; Laskin, A.; Bertram, A. K.; Nizkorodov, S. A.; Shiraiwa, M. Predicting the Glass Transition Temperature and Viscosity of Secondary Organic Material Using Molecular Composition. *Atmos. Chem. Phys.* **2018**, *18* (9), 6331–6351. https://doi.org/10.5194/acp-18-6331-2018.

(45) Sheldon, C. S.; Salazar, J.; Palacios Diaz, T.; Morton, K.; Davis, R. D.; Davies, J. F. Correlating the Viscosity and Rate of Water Diffusion in Semisolid Gel-Forming Aerosol Particles. *ACS Earth Space Chem.* **2023**, *7* (11), 2311–2320. https://doi.org/10.1021/acsearthspacechem.3c00241.

(46) Campbell, J. R.; Battaglia, M.; Dingilian, K.; Cesler-Maloney, M.; St Clair, J. M.; Hanisco, T. F.; Robinson, E.; Decarlo, P.; Simpson, W.; Nenes, A.; Weber, R. J.; Mao, J. Source and Chemistry of Hydroxymethanesulfonate (HMS) in Fairbanks, Alaska. *Environ. Sci. Technol.* **2022**. https://doi.org/10.1021/acs.est.2c00410.

(47) Dingilian, K.; Hebert, E.; Battaglia, M.; Campbell, J. R.; Cesler-Maloney, M.; Simpson, W.; St. Clair, J. M.; Dibb, J.; Temime-Roussel, B.; D'Anna, B.; Moon, A.; Alexander, B.; Yang, Y.; Nenes, A.; Mao, J.; Weber, R. J. Hydroxymethanesulfonate and Sulfur(IV) in Fairbanks Winter During the ALPACA Study. *ACS ES&T Air* **2024**, *1* (7), 646–659. https://doi.org/10.1021/acsestair.4c00012.

(48) Kotchenruther, R. A. Source Apportionment of PM2.5 at Multiple Northwest U.S. Sites: Assessing Regional Winter Wood Smoke Impacts from Residential Wood Combustion. *Atmos. Environ.* **2016**, *142*, 210–219. https://doi.org/10.1016/j.atmosenv.2016.07.048.

(49) Feigenbrugel, V.; Le Calvé, S.; Mirabel, P.; Louis, F. Henry's Law Constant Measurements for Phenol, o-, m-, and p-Cresol as a Function of Temperature. *Atmos. Environ.* **2004**, *38* (33), 5577–5588. https://doi.org/10.1016/j.atmosenv.2004.06.025.

(50) Carl L Yaws. *The Yaws Handbook of Vapor Pressure*, Second Edition.; Gulf Professional Publishing, **2015**.

(51) Chyliński, K.; Fraś, Z.; Malanowski, S. K. Vapor-Liquid Equilibrium in Phenol + 2-Ethoxyethanol at 363.15 to 383.15 K. *J. Chem. Eng. Data* **2001**, *46* (1), 29–33. https://doi.org/10.1021/je0001072.

(52) Richard, L. S.; Bernardes, C. E. S.; Diogo, H. P.; Leal, J. P.; Da Piedade, M. E. M. Energetics of Cresols and of Methylphenoxyl Radicals. *Journal of Physical Chemistry A* **2007**, *111* (35), 8741–8748. https://doi.org/10.1021/jp073515m.

(53) Mackay, D.; Shiu, W. Y.; Ma, K.-C.; Lee, S. C. *Handbook of Physical-Chemical Properties and Environmental Fate for Organic Chemicals Volume I Introduction and Hydrocarbons*, Second Edition.; Taylor & Francis Group, **2006**; Vol. I.

(54) Verevkin, S. P.; Schick, C. Substituent Effects on the Benzene Ring. Determination of the Intramolecular Interactions of Substituents in Tert-Alkyl-Substituted Catechols from Thermochemical Measurements. *J. Chem. Eng. Data* **2000**, *45* (5), 946–952. https://doi.org/10.1021/je0001126.

(55) Stephenson, R. M.; Malanowski, S. *Handbook of the Thermodynamics of Organic Compounds*, 1st ed.; Elsevier, **1987**.

(56) Sagabiel, J. C.; Seiber, J. N.; Woodrow, J. E. Comparison of Headspace and Gas-Stripping Methods for Determining the Henry's Law Constants (H) for Organic Compounds of Low to Intermediate H. *Chemosphere* **1992**, *25* (12), 1763–1768. https://doi.org/10.1016/0045-6535(92)90017-L.

(57) Ponomarev, D. A.; Oleinikova, T. P.; Masalitinova, T. N. Enthalpy of Creosol Formation. *Khim. Khim. Tekhnol.* **1987**, *30*, 115–116.

(58) Sander, R. Compilation of Henry's Law Constants (Version 4.0) for Water as Solvent. *Atmos. Chem. Phys.* **2015**, *15* (8), 4399–4981. https://doi.org/10.5194/acp-15-4399-2015.

(59) Van Roon, A.; Parsons, J. R.; Govers, H. A. J. Gas Chromatographic Determination of Vapour Pressure and Related Thermodynamic Properties of Monoterpenes and Biogenically Related Compounds. *J. Chromatogr. A* **2002**, *955*, 105–115. https://doi.org/https://doi.org/10.1016/S0021-9673(02)00200-5.

(60) US EPA. Estimation Programs Interface Suite™ for Microsoft® Windows. United States Environmental Protection Agency: Washington, DC, USA **2012**.

(61) Battino, R.; Rettich, T. R.; Tominaga, T. The Solubility of Oxygen and Ozone in Liquids. *J. Phys. Chem. Ref. Data* **1983**, *12* (2), 163–178. https://doi.org/10.1063/1.555680.

(62) Arakaki, T.; Anastasio, C.; Kuroki, Y.; Nakajima, H.; Okada, K.; Kotani, Y.; Handa, D.; Azechi, S.; Kimura, T.; Tsuhako, A.; Miyagi, Y. A General Scavenging Rate Constant for Reaction of Hydroxyl Radical with Organic Carbon in Atmospheric Waters. *Environ. Sci. Technol.* **2013**, *47* (15), 8196–8203. https://doi.org/10.1021/es401927b.

(63) Appiani, E.; Ossola, R.; Latch, D. E.; Erickson, P. R.; McNeill, K. Aqueous Singlet Oxygen Reaction Kinetics of Furfuryl Alcohol: Effect of Temperature, PH, and Salt Content. *Environ. Sci. Process. Impacts* **2017**, *19* (4), 507–516. https://doi.org/10.1039/c6em00646a.

(64) Kiliç, M.; Koçtürk, G.; San, N.; Çinar, Z. A Model for Prediction of Product Distributions for the Reactions of Phenol Derivatives with Hydroxyl Radicals. *Chemosphere* **2007**, *69* (9), 1396–1408. https://doi.org/10.1016/j.chemosphere.2007.05.002.

(65) Atkinson, R. Kinetics and Mechanisms of the Gas-Phase Reactions of the NO3 Radical with Organic Compounds. *J. Phys. Chem. Ref. Data* **1991**, *20* (3), 459–507. https://doi.org/10.1063/1.555887.

(66) Coeur-Tourneur, C.; Foulon, V.; Laréal, M. Determination of Aerosol Yields from 3-Methylcatechol and 4-Methylcatechol Ozonolysis in a Simulation Chamber. *Atmos. Environ.* **2010**, *44* (6), 852–857. https://doi.org/10.1016/j.atmosenv.2009.11.027.

(67) Tomas, A.; Olariu, R. I.; Barnes, I.; Becker, K. H. Kinetics of the Reaction of O3 with Selected Benzenediols. *Int. J. Chem. Kinet.* **2003**, *35* (6), 223–230. https://doi.org/10.1002/kin.10121.

(68) El Zein, A.; Coeur, C.; Obeid, E.; Lauraguais, A.; Fagniez, T. Reaction Kinetics of Catechol (1,2-Benzenediol) and Guaiacol (2-Methoxyphenol) with Ozone. *Journal of Physical Chemistry A* **2015**, *119* (26), 6759–6765. https://doi.org/10.1021/acs.jpca.5b00174.

(69) Lauraguais, A.; Coeur-Tourneur, C.; Cassez, A.; Seydi, A. Rate Constant and Secondary Organic Aerosol Yields for the Gas-Phase Reaction of Hydroxyl Radicals with Syringol (2,6-Dimethoxyphenol). *Atmos. Environ.* **2012**, *55*, 43–48. https://doi.org/10.1016/j.atmosenv.2012.02.027.

(70) Zhang, H.; Yang, B.; Wang, Y.; Shu, J.; Zhang, P.; Ma, P.; Li, Z. Gas-Phase Reactions of Methoxyphenols with NO3 Radicals: Kinetics, Products, and Mechanisms. *Journal of Physical Chemistry A* **2016**, *120* (8), 1213–1221. https://doi.org/10.1021/acs.jpca.5b10406.

(71) Wei, B.; Sun, J.; Mei, Q.; He, M. Mechanism and Kinetic of Nitrate Radical-Initiated Atmospheric Reactions of Guaiacol (2-Methoxyphenol). *Comput. Theor. Chem.* **2018**, *1129*, 1–8. https://doi.org/10.1016/j.comptc.2018.02.014.

(72) Sun, Y.; Chen, X.; Liu, L.; Xu, F.; Zhang, X. Mechanisms and Kinetics Studies of the Atmospheric Oxidation of Eugenol by Hydroxyl Radicals and Ozone Molecules. *Science of the Total Environment* **2021**, *770*. https://doi.org/10.1016/j.scitotenv.2021.145203.

(73) Liu, C.; Chen, D.; Chen, X. Atmospheric Reactivity of Methoxyphenols: A Review. *Environ. Sci. Technol.* **2022**, *56* (5), 2897–2916. https://doi.org/10.1021/acs.est.1c06535.

(74) Sun, Y.; Liu, L.; Li, M.; Chen, X.; Xu, F. Theoretical Investigation on the Mechanisms and Kinetics of OH/NO3-Initiated Atmospheric Oxidation of Vanillin and Vanillic Acid. *Chemosphere* **2022**, *288*. https://doi.org/10.1016/j.chemosphere.2021.132544.

(75) Liu, C.; Zeng, C. Heterogeneous Kinetics of Methoxyphenols in the OH-Initiated Reactions under Different Experimental Conditions. *Chemosphere* **2018**, *209*, 560–567. https://doi.org/10.1016/j.chemosphere.2018.06.131.

(76) Hoffmann, D.; Tilgner, A.; Iinuma, Y.; Herrmann, H. Atmospheric Stability of Levoglucosan: A Detailed Laboratory and Modeling Study. *Environ. Sci. Technol.* **2010**, *44* (2), 694–699. https://doi.org/10.1021/es902476f.

(77) Smith, J. D.; Kinney, H.; Anastasio, C. Aqueous Benzene-Diols React with an Organic Triplet Excited State and Hydroxyl Radical to Form Secondary Organic Aerosol. *Physical Chemistry Chemical Physics* **2015**, *17* (15), 10227–10237. https://doi.org/10.1039/c4cp06095d.

(78) Tratnyek, P. G.; Hoigné, J. Oxidation of Substituted Phenols in the Environment: A QSAR Analysis of Rate Constants for Reaction with Singlet Oxygen. *Environ. Sci. Technol* **1991**, *25*, 1596–1604. https://doi.org/10.1021/es00021a011.

(79) Buxton, G. V.; Greenstock, C. L.; Helman, W. P.; Ross, A. B. Critical Review of Rate Constants for Reactions of Hydrated Electrons, Hydrogen Atoms and Hydroxyl Radicals (·OH/·O−) in Aqueous Solution. *J. Phys. Chem. Ref. Data* **1988**, *17* (2), 513–886. https://doi.org/10.1063/1.555805.

(80) Kroflič, A.; Schaefer, T.; Huš, M.; Phuoc Le, H.; Otto, T.; Herrmann, H. OH Radicals Reactivity towards Phenol-Related Pollutants in Water: Temperature Dependence of the Rate Constants and Novel Insights into the [OH-Phenol] Adduct Formation. *Physical Chemistry Chemical Physics* **2020**, *22* (3), 1324–1332. https://doi.org/10.1039/c9cp05533a.

(81) He, L.; Schaefer, T.; Otto, T.; Kroflič, A.; Herrmann, H. Kinetic and Theoretical Study of the Atmospheric Aqueous-Phase Reactions of OH Radicals with Methoxyphenolic Compounds. *Journal of Physical Chemistry A* **2019**, *123* (36), 7828–7838. https://doi.org/10.1021/acs.jpca.9b05696.

(82) Arciva, S.; Niedek, C.; Mavis, C.; Yoon, M.; Sanchez, M. E.; Zhang, Q.; Anastasio, C. Aqueous ·OH Oxidation of Highly Substituted Phenols as a Source of Secondary Organic Aerosol. *Environ. Sci. Technol.* **2022**, *56* (14), 9959–9967. https://doi.org/10.1021/acs.est.2c02225.

(83) Ma, L.; Guzman, C.; Niedek, C.; Tran, T.; Zhang, Q.; Anastasio, C. Kinetics and Mass Yields of Aqueous Secondary Organic Aerosol from Highly Substituted Phenols Reacting with a Triplet Excited State. *Environ. Sci. Technol.* **2021**, *55* (9), 5772–5781. https://doi.org/10.1021/acs.est.1c00575.

(84) Li, Y. J.; Huang, D. D.; Cheung, H. Y.; Lee, A. K. Y.; Chan, C. K. Aqueous-Phase Photochemical Oxidation and Direct Photolysis of Vanillin - A Model Compound of Methoxy Phenols from Biomass Burning. *Atmos. Chem. Phys.* **2014**, *14* (6), 2871–2885. https://doi.org/10.5194/acp-14-2871-2014.

(85) Zhou, R.; Liu, J.; Zhou, C.; Zhang, X. Phototransformation of Lignin-Related Compounds in Chromophoric Dissolved Organic Matter Solutions. *Water Res.* **2023**, *245*. https://doi.org/10.1016/j.watres.2023.120586.

(86) An, Z.; Sun, J.; Han, D.; Mei, Q.; Wei, B.; Wang, X.; Xie, J.; Zhan, J.; He, M. Effect of PH on ·OH-Induced Degradation Progress of Syringol/Syringaldehyde and Health Effect. *Chemosphere* **2020**, *255*. https://doi.org/10.1016/j.chemosphere.2020.126893.

(87) Tang, S.; Li, F.; Tsona, N. T.; Lu, C.; Wang, X.; Du, L. Aqueous-Phase Photooxidation of Vanillic Acid: A Potential Source of Humic-Like Substances (HULIS). *ACS Earth Space Chem.* **2020**, *4* (6), 862–872. https://doi.org/10.1021/acsearthspacechem.0c00070.

(88) Weller, C.; Hoffmann, D.; Schaefer, T.; Herrmann, H. Temperature and Ionic Strength Dependence of NO 3-Radical Reactions with Substituted Phenols in Aqueous Solution. *Z. Phys. Chem* **2010**, *224*, 4. https://doi.org/10.1524.zpch.2010.6151.

(89) Hoigne, J.; Bader, H. Rate Constants of Reactions of Ozone with Organic and Inorganic Compounds in Water-II. *Water Res.* **1983**, *17*, 185–194. https://doi.org/10.1016/0043-1354(83)90098-2.

(90) Gurol, M. D.; Nekoulnalnl, S. Kinetic Behavior of Ozone in Aqueous Solutions of Substituted Phenols. *Ind. Eng. Chem. Fundam.* **1984**, *6* (23), 54–60. https://doi.org/10.1021/i100013a011.

(91) Khudoshin, A. G.; Mitrofanova, A. N.; Lunin, V. V. Kinetics and Mechanism of the Reactions of Ozone with Guaiacol, Veratrol, and Veratrol Derivatives. *Russian Chemical Bulletin, International Edition* **2008**, *57* (2), 283–288. https://doi.org/10.1007/s11172-008-0043-6.

(92) Wang, Y.; Mekic, M.; Li, P.; Deng, H.; Liu, S.; Jiang, B.; Jin, B.; Vione, D.; Gligorovski, S. Ionic Strength Effect Triggers Brown Carbon Formation through Heterogeneous Ozone Processing of Ortho-Vanillin. *Environ. Sci. Technol.* **2021**, *55* (8), 4553–4564. https://doi.org/10.1021/acs.est.1c00874.

(93) Ragnar, M.; Eriksson, T.; Reitberger, T. Radical Formation in Ozone Reactions with Lignin and Carbohydrate Model Compounds. *Holzforschung* **1999**, *53* (3), 292–298. https://doi.org/10.1515/HF.1999.049.

(94) Yee, L. D.; Kautzman, K. E.; Loza, C. L.; Schilling, K. A.; Coggon, M. M.; Chhabra, P. S.; Chan, M. N.; Chan, A. W. H.; Hersey, S. P.; Crounse, J. D.; Wennberg, P. O.; Flagan, R. C.; Seinfeld, J. H. Secondary Organic Aerosol Formation from Biomass Burning Intermediates: Phenol and Methoxyphenols. *Atmos. Chem. Phys.* **2013**, *13* (16), 8019–8043. https://doi.org/10.5194/acp-13-8019-2013.

(95) Coeur-Tourneur, C.; Tomas, A.; Guilloteau, A.; Henry, F.; Ledoux, F.; Visez, N.; Riffault, V.; Wenger, J. C.; Bedjanian, Y. Aerosol Formation Yields from the Reaction of Catechol with Ozone. *Atmos. Environ.* **2009**, *43* (14), 2360–2365. https://doi.org/10.1016/j.atmosenv.2008.12.054.

(96) Meng, L.; Coeur, C.; Fayad, L.; Houzel, N.; Genevray, P.; Bouzidi, H.; Tomas, A.; Chen, W. Secondary Organic Aerosol Formation from the Gas-Phase Reaction of Guaiacol (2-Methoxyphenol) with NO3 Radicals. *Atmos. Environ.* **2020**, *240*. https://doi.org/10.1016/j.atmosenv.2020.117740.

(97) Smith, J. D.; Sio, V.; Yu, L.; Zhang, Q.; Anastasio, C. Secondary Organic Aerosol Production from Aqueous Reactions of Atmospheric Phenols with an Organic Triplet Excited State. *Environ. Sci. Technol.* **2014**, *48* (2), 1049–1057. https://doi.org/10.1021/es4045715.

(98) Chen, Y.; Li, N.; Li, X.; Tao, Y.; Luo, S.; Zhao, Z.; Ma, S.; Huang, H.; Chen, Y.; Ye, Z.; Ge, X. Secondary Organic Aerosol Formation from ^{3}C*-Initiated Oxidation of 4-Ethylguaiacol in Atmospheric Aqueous-Phase. *Science of the Total Environment* **2020**, *723*. https://doi.org/10.1016/j.scitotenv.2020.137953.

(99) Yu, L.; Smith, J.; Laskin, A.; M George, K.; Anastasio, C.; Laskin, J.; M Dillner, A.; Zhang, Q. Molecular Transformations of Phenolic SOA during Photochemical Aging in the Aqueous Phase: Competition among Oligomerization, Functionalization, and Fragmentation. *Atmos. Chem. Phys.* **2016**, *16* (7), 4511–4527. https://doi.org/10.5194/acp-16-4511-2016.

(100) Yu, L.; Smith, J.; Laskin, A.; Anastasio, C.; Laskin, J.; Zhang, Q. Chemical Characterization of SOA Formed from Aqueous-Phase Reactions of Phenols with the Triplet Excited State of Carbonyl and Hydroxyl Radical. *Atmos. Chem. Phys.* **2014**, *14* (24), 13801–13816. https://doi.org/10.5194/acp-14-13801-2014.

(101) Hendrickx, M. F. A.; Vinckier, C. 1,3-Cycloaddition of Ozone to Ethylene, Benzene, and Phenol: A Comparative Ab Initio Study. *Journal of Physical Chemistry A* **2003**, *107* (38), 7574–7580. https://doi.org/10.1021/jp034541x.

(102) Wang, W.; Liu, M.; Wang, T.; Song, Y.; Zhou, L.; Cao, J.; Hu, J.; Tang, G.; Chen, Z.; Li, Z.; Xu, Z.; Peng, C.; Lian, C.; Chen, Y.; Pan, Y.; Zhang, Y.; Sun, Y.; Li, W.; Zhu, T.; Tian, H.; Ge, M. Sulfate Formation Is Dominated by Manganese-Catalyzed Oxidation of SO2 on Aerosol Surfaces during Haze Events. *Nat. Commun.* **2021**, *12* (1). https://doi.org/10.1038/s41467-021-22091-6.

(103) Wei, B.; Sun, J.; Mei, Q.; An, Z.; Cao, H.; Han, D.; Xie, J.; Zhan, J.; Zhang, Q.; Wang, W.; He, M. Reactivity of Aromatic Contaminants towards Nitrate Radical in Tropospheric Gas and Aqueous Phase. *J. Hazard. Mater.* **2021**, *401*. https://doi.org/10.1016/j.jhazmat.2020.123396.

(104) Richards-Henderson, N. K.; Pham, A. T.; Kirk, B. B.; Anastasio, C. Secondary Organic Aerosol from Aqueous Reactions of Green Leaf Volatiles with Organic Triplet Excited

States and Singlet Molecular Oxygen. *Environ. Sci. Technol.* **2015**, *49* (1), 268–276. https://doi.org/10.1021/es503656m.

(105) Sun, Y.; Xu, F.; Li, X.; Zhang, Q.; Gu, Y. Mechanisms and Kinetic Studies of OH-Initiated Atmospheric Oxidation of Methoxyphenols in the Presence of O2 and NOx. *Physical Chemistry Chemical Physics* **2019**, *21* (39), 21856–21866. https://doi.org/10.1039/c9cp03246k.

(106) Benitez, F. J.; Beltran-Heredia, J.; Gonzalez, T.; Real, F. Kinetics of the Direct Reaction between Ozone and Phenolic Aldehydes. *Journal of Chemical Technology and Biotechnology* **1998**, *72* (3), 235–244. https://doi.org/10.1002/(SICI)1097-4660(199807)72:3<235::AID-JCTB907>3.0.CO;2-G.

(107) Simpson, W.; Cesler-Maloney, M.; Hoskins-Chaddon, R. Gas and Meteorological Measurements at the CTC Site and Birch Hill in Fairbanks, Alaska, during the ALPACA-2022 Field Study. *Arctic Data Center [data set]* **2023**.

(108) Kuhn, J.; Heinlein, L. M. D.; Cesler-Maloney, M.; Dibb, J. E.; Thomas, J.; Bartels-Rausch, T.; Sunday, M. O.; R Simpson, W.; Anastasio, C.; Stutz, J. Secondary Aerosol Production in Heavily Polluted Cold-Climate Urban Environmental Can Be Enhanced by Precursor Reduction. https://doi.org/10.26434/chemrxiv.10001971/v1. *In Review*.